UNIVERSITÄT PADERBORN
Die Universität der Informationsgesellschaft

Faculty of Natural Sciences
Department of Physics

Structure Sensitive Investigations on Mn-activated Perovskites and Rare-Earth-doped Aluminates

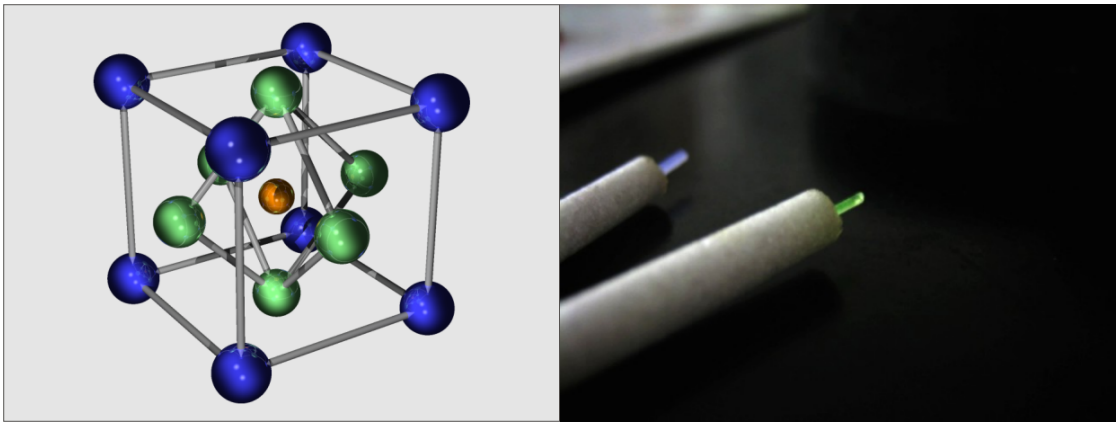

Dissertation

von Dipl. Phys.
Bastian Henke

Gutachter: PD Dr. Stefan Schweizer
Zweitgutachter: Prof. Dr. Gerhard Wortmann

Abgabe der Dissertation: 19. Oktober 2007
Datum der mündlichen Prüfung: 11. Dezember 2007

Abstract

In this work optical, magnetic resonance, and optically-detected magnetic resonance measurement techniques were used to investigate the Mn-activated fluoroperovskites $RbCdF_3$ and $LiBaF_3$ as well as the rare-earth (RE) doped persistent phosphors $SrAl_2O_4$ and $CaAl_2O_4$.

The photoluminescence (PL) of Mn-activated $RbCdF_3$ shows an emission band at 560 nm, which can be attributed to the Mn^{2+} dopant; the corresponding excitation bands are between 240 and 520 nm. After x-irradiation an increased Mn^{2+} emission can be observed and the excitation spectrum shows an additional intense broad band at 300 nm. Excitation at 300 nm leads to a decreasing intensity of the Mn^{2+} emission, whereas excitation at 240 nm leads to an increase in the PL intensity. Electron paramagnetic resonance (EPR) shows that the number of Mn^{2+} ions is reduced upon x-irradiation; the original Mn^{2+} level can be restored by optical bleaching.

In $LiBaF_3$ it was possible to identify a luminescent oxygen vacancy complex emitting in the blue spectral region. The structure of that complex was investigated by PL and PL-detected electron paramagnetic resonance (PL-EPR). At 20 K the oxygen-related complex shows two luminescence bands peaking at about 430 and 475 nm, when excited at 220 nm. These bands can be attributed to an excited triplet state ($S = 1$) with the z-axis of the fine structure tensor parallel to the <110> direction. This complex is believed to be next to a Mn^{2+} impurity on a Ba^{2+} site and can be described by an oxygen on a fluorine lattice site with a nearest fluorine vacancy along the <110> direction.

Prior to x-irradiation the PL of Mn-activated $LiBaF_3$ shows a Mn^{2+} emission band at 710 nm; the corresponding excitation bands are between 210 and 620 nm. After x-irradiation the PL spectrum shows a new emission peaking at about 610 nm which is tentatively assigned to a perturbed Mn^{2+} emission; the intensity of all PL bands is increased. Structure sensitive investigations on the radiation-induced emission band

were done by PL-EPR at a temperature of 1.5 K. The analysis of the angular dependent PL-EPR spectra, recorded for different orientations of the magnetic field, yielded that the 610 nm luminescence band is due to an excited triplet state ($S = 1$) of a Mn-related center with the z-axis of the fine structure tensor close to a <110> direction.

Single-crystals of MAl_2O_4 (M=Ca and Sr) persistent phosphors that are nominally pure or doped with Eu and Nd or Dy, respectively, were investigated. Their recombination luminescence (RL) and microwave-induced changes in the RL in a high magnetic field (RL-EPR) were investigated after ultraviolet excitation at low temperatures. Wavelength dependent RL-EPR measurements indicate that only one intrinsic donor but at least two different intrinsic acceptors are involved in the recombination process. The donor-acceptor recombination energy is either emitted directly (undoped samples) or almost completely transferred to the RE activators (doped samples).

Contents

1 Introduction

In recent years there has been interest in dosimetric materials where the dose can be read out via optically stimulated luminescence (OSL) and not as usually via thermally stimulated luminescence. The most important advantage of OSL active materials is the possibility to be bleached optically and to be reused.

The use of OSL for personnel dosimetry, is not widely spread and in radiation dosimetry it has not been extensively reported, mainly because of the lack of a good luminescent material.

MgS, CaS, SrS, and SrSe doped with different rare-earth (RE) elements such as Ce, Sm, and Eu were among the first phosphors suggested for OSL dosimetry applications. They possess a high sensitivity to radiation and a high efficiency under infrared stimulation at a wavelength around 1 μm, but they show a significant fading of the luminescence at room temperature (RT). These phosphors also have a very high effective atomic number and, as a result, they exhibit strong photon energy dependence, which is unacceptable for use in personnel dosimetry.

Alternative materials can be found in $AMeF_3$ perovskites, where A is an alkali metal, Me is a transition metal, and F is a fluorine ion. These compounds doped with an activator ion, e.g. Mn^{2+}, are known to emit an enhanced luminescence after irradiation. This was first observed by Sibley and Koumvakalis in $RbMgF_3$:Mn^{2+} [1]. It was supposed that an F-centre (electron trapped at an anion vacancy), in the vicinity of the Mn dopant, enhances the oscillator strength leading to increased emission intensity. A similar effect was observed in $RbCdF_3$:Mn^{2+}, where after x-irradiation an increased luminescence and an additional absorption band around 310 nm occurs; this band can also be observed in nominally pure $RbCdF_3$ [2]. The 310 nm band was tentatively assigned to intrinsic defects being created upon x-irradiation. The radiation-induced luminescence intensity is correlated with the x-ray dose; Mn-doped $RbCdF_3$ has potential as a radiation dosimeter material.

Persistent phosphors are compounds which emit a very long lasting afterglow after excitation mainly in the UV spectral range. Long persistent phosphors have a great potential in applications such as emergency illumination in planes and trains or as luminous dials. The first materials were ZnS:Cu and alkali sulfides like CaS and SrS. In 1996 rare-earth doped aluminates MAl_2O_4 (M = Ca, Sr) have been found as a new type of persistent phosphor [3]. Their emission can be attributed to the RE activator Eu^{2+} and is due to a $5f - 4d$ transition. Although the single doped systems show already a phosphorescent behavior, the addition of Dy in the case of $SrAl_2O_4$ (SAO) and of Nd in the case of $CaAl_2O_4$ (CAO) leads to a significant increase in the phosphorescent lifetime. Upon this additional codoping the phosphorescent lifetime is extended to about 16 hours. These two phosphors drew considerable attentions from many scientists because a 16 hours persistent time could bring the phosphorescence over a whole night.

The complete mechanism of this phosphorescent luminescence is still unknown although several models have been proposed [4, 5]. On the one hand it has been assumed that only RE traps are involved in the recombination process. On the other hand it was supposed that intrinsic traps are the source of the traps.

Theoretical and experimental fundamentals of the main experimental methods used in this work are described in chapter two.

Chapter three deals in the first part with Mn-activated $RbCdF_3$, especially with the investigation of x-irradiation induced effects. The second part is about two different luminescent centers in the Mn-activated inverse fluoroperovskite $LiBaF_3$ investigated by photoluminescence detected electron paramagnetic resonance.

The fourth chapter is about the persistent phosphors CAO and SAO. Low temperature recombination processes leading to phosphorescence in RE doped CAO and SAO single crystals is studied by detecting the microwave-induced changes in the recombination luminescence.

Parts of the present work have already been published, a publication list is added at the end of this thesis.

2 Physical Background

2.1 Perovskites

2.1.1 Crystal Structure

The name perovskite represents a group of crystals having the same structure. The perovskites presented in this work have an $AMeF_3$ structure, where A stands for a cation, Me for a metal and F for fluorine. The crystal structure of $AMeF_3$ perovskites depends on the tolerance factor t, which gives a relation between the radii of the cation, the metal, and the fluorine. The tolerance factor is defined by

$$t = \frac{r_A + r_F}{\sqrt{2} \cdot (r_{Me} + r_F)}. \tag{2.1}$$

A perovskite structure is expected if t has a value within the range $0.76 \leq t \leq 1.13$. For a tolerance factor of $0.76 \leq t \leq 0.88$ the orthorhombically distorted $GdFeO_3$-type structure is found, which corresponds to the space group $Pbnm$.

The ideal cubic structure of $AMeF_3$ belongs to a tolerance factor range of $0.88 \leq t \leq 1.00$, space group $Pm3m$ (see Figure 2.1). The A-ions have 12 fluorine neighbors while the metal ions have six. Thus, the metal ions with six neighbors form a MeF_6 octahedron, which is linked to a neighboring MeF_6 octahedron by sharing the corners throughout the structure.

In orthorhombic perovskites the Me-F-Me bridge angles (Figure 2.1 left side, horizontal solid line) deviate significantly from linearity which is the main difference between cubic and orthorhombic perovskites. This means a rotation of the MeF_6 octahedron about one of its fourfold axes. As the tolerance factor is a measure of the misfit between the size of the MeF_6 octahedra and that of the A cations, the Me-F-Me bridge angles depend on t. A smaller tolerance factor means a smaller bridge angle.

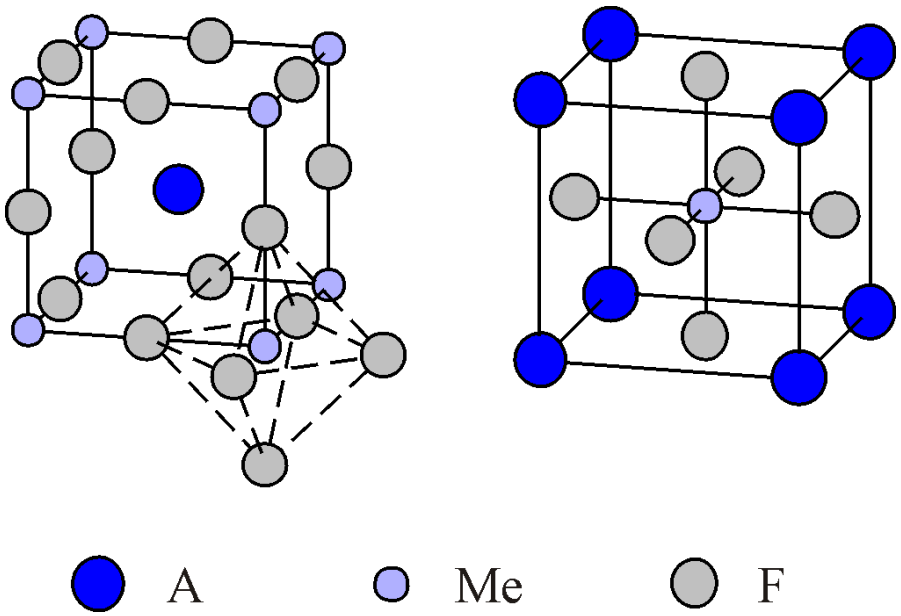

Figure 2.1: Cubic perovskite. The left picture shows how the six fluorine neighbors of the Me ion form an octahedron.

$AMeF_3$ fluorides with a tolerance factor $t > 1$ adopt a variety of hexagonal structures. In all these hexagonal structures a face-sharing of the octahedra occurs, which is a kind of linking.

2.1.2 Photoluminescence of Mn^{2+}

In the following section the electronic structure of Mn^{2+} will be explained for a better understanding of its optical properties. Mn^{2+} has an incompletely filled d shell and its electron configuration is d^5. The energy levels originating from this configuration have been calculated by Tanabe and Sugano considering the interaction between the d electrons and the crystal field [6].

The energy levels of a free ion can be found on the left hand side of these Tanabe-Sugano diagrams, see Figure 2.2. Many of these levels split into two or more levels for a crystal field $10Dq \neq 0$. The ground state is represented by the x axis. The free ion levels are marked ^{2S+1}L, where S presents the total spin quantum number, and L the total orbital angular momentum. The degeneracy of these levels is $2L + 1$ and can be lifted by the crystal field. Crystal field energy levels are marked ^{2S+1}X, where X may be A for no degeneracy, B for a twofold degeneracy and T for a threefold degeneracy.

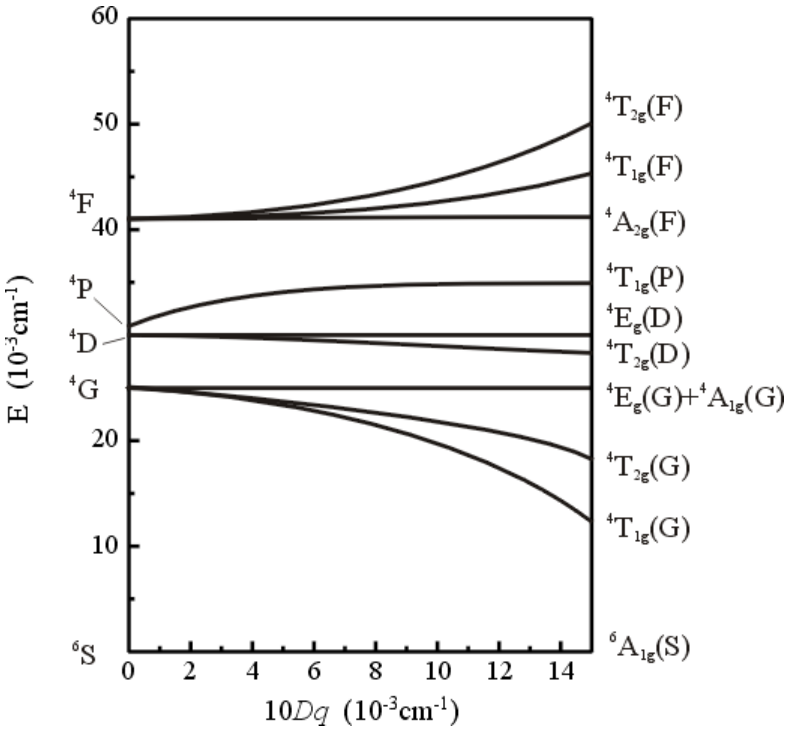

Figure 2.2: The energy levels of Mn^{2+} as a function of the octahedral crystal field $10Dq$. The x axis represents the ground state.

Subscripts indicate certain symmetry properties and the letter in brackets represents the energy level of the free ion. For further information the reader is referred to [6, 7].

The Tanabe-Sugano diagram for Mn^{2+} in an octahedral O_h surrounding is shown in Figure 2.2. The ground state is ${}^6A_{1g}(S)$. Since these energy levels are all within the d shell, all transitions from the ground state to excited levels are spin and parity forbidden. However, the Mn^{2+} transitions can still be observed. It was suggested that the selection rule is relaxed through a spin-spin interaction and a vibronic mechanism, where the electronic transitions are coupled with vibrations of suitable symmetry [7].

Exciting a system with UV light brings an electron of Mn^{2+} in a high vibrational level of the excited state, as shown in Figure 2.3. The electron falls to the lowest vibrational level of the excited state giving up the excess energy to the surrounding. Another way to describe this process is to say that the nucleus adjusts its position to the excited state, so the interatomic distance varies from the distance it has in equilibrium. The configurational coordinate changes by ΔR. This process is called relaxation. From the lowest vibrational level the electron can return to the ground state spontaneously under

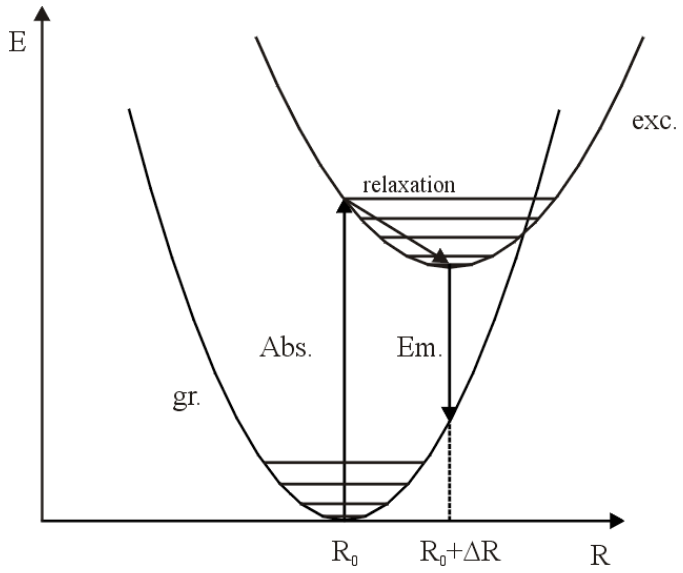

Figure 2.3: Configurational coordinate diagram. After absorption the system reaches a high vibrational level of the excited state. Subsequently it relaxes to the lowest vibrational level from where the emission occurs.

emission of radiation. From this it can be seen, that the emission has a lower energy than the excitation of the same excited level. This effect is called Stokes Shift.

Typical photostimulated spectrum and excitation bands from Mn^{2+} are given in Figure 2.4. The PL arises from the radiative return to the ground state via the ${}^4T_{1g}(G) \rightarrow {}^6A_{1g}(S)$ transition. The excitation bands are marked with their corresponding energy level. An interesting feature in this excitation spectrum is the different width of the excitation maxima. In particular the degenerate states ${}^4A_{1g}(G)$ and ${}^4E_g(G)$ have a narrow band and the ${}^4T_{2g}(G)$ and ${}^4T_{1g}(G)$ states are rather broad. The band-width is due to coupling with vibrations. Since the crystal field strength varies during the vibration the Tanabe-Sugano diagrams predict the width of the band. If the level runs parallel to the ground level a variation of Δ will not influence the transition energy and a narrow band can be expected like the ones observed for ${}^4A_{1g}(G)$ and ${}^4E_g(G)$. From this reason these energy levels show for most systems their excitation band at about 400 nm. If the excited levels has a slope relative to the ground state a variation of Δ will influence the transition energy, and a broad transition band can be expected. Because of this, the ${}^4T_{1g}(G)$ is most sensitive to changes in Δ and has significant different values for all systems.

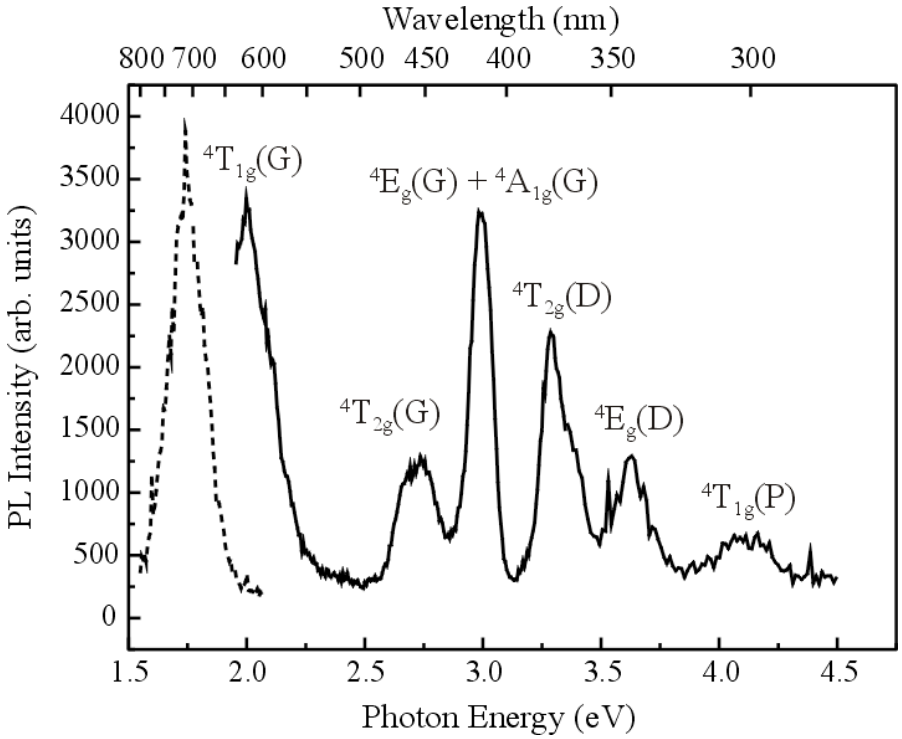

Figure 2.4: The dashed curve shows the PL spectrum of Mn^{2+} in $LiBaF_3$, excited at 255 nm. The solid curve presents the excitation bands for this transition and the PL was detected at 712 nm.

Another property in these systems is the distance between the Me and the F ions R_{MF}. The $10Dq$ parameter strongly depends on R_{MF} by the inverse power law found by Rodriguez [8]. They showed that the dependence of $10Dq$ with R_{MF} can be described in the form

$$10Dq = K \cdot R_{\mathrm{MF}}^{-n} \tag{2.2}$$

where K and n are constants. However, this law is only valid in a small range of R_{MF} (2.0-2.2 Å).

2.2 Experimental

The luminescence spectrometer is shown in Figure 2.5. Photoluminescence (PL) and x-ray excited luminescence (XL) spectra were recorded with a single beam spectrometer in which two 0.22 m double monochromators were available for excitation and luminescence.

Figure 2.5: Photograph of the luminescence spectrometer: a) Xenon lamp, b) excitation monochromator, c) cryostat, d) emission monochromator, e) Photomultiplier.

The PL excitation was carried out with a xenon lamp, the x-ray excitation with a tungsten tube (50-60 kV, 15-30 mA). The luminescence was detected using single photon counting with a cooled photomultiplier. For the lifetime measurements a nitrogen flash lamp or an iris in combination with a computer-controlled transient recording board were used. For low temperature measurements a continuous flow cryostat was used. The spectra were not corrected for spectral sensitivity of the experimental setup.

2.3 Magneto-Optical Measurement Techniques

2.3.1 Photoluminescence detected Electron Paramagnetic Resonance

With the PL-EPR technique it is possible to detect triplet spin systems. Triplet states are often found as strongly coupled electrons and holes after band to band excitation, which may be excitons bound to an impurity. Each of these two particles have a spin of $S = 1/2$, are strongly coupled and form a triplet spin $S = 1$. Figure 2.6 shows the energy levels of a triplet with fine structure interaction for an external magnetic field $\vec{B}$

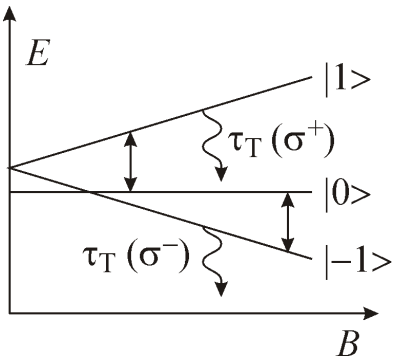

Figure 2.6: Level scheme of a triplet spin state system in an external magnetic field. The rippled arrows indicate allowed transitions to the ground state.

parallel to the fine-structure axes.

With no applied magnetic field the $m_S = \pm 1$ and $m_S = 0$ levels are split by the fine-structure constant D. Applying a higher magnetic field leads to a further splitting of the $m_S = \pm 1$ levels. There are allowed transitions to the singlet ground state for the $|+1>$ and $|-1>$ levels (indicated by waved arrows) but not for the $|\,0>$ level. Thus the $|\,0>$ level will have a higher population than the $|+1>$ and $|-1>$ energy states. By applying microwaves it is possible to induce fine-structure EPR transition from $|\,0>$ to $|+1>$ and $|-1>$, indicated by arrows in Figure 2.6. Both transitions lead to an enhanced PL intensity which can be detected.

2.3.2 Recombination Luminesence detected Electron Paramagnetic Resonance of Weakly Coupled Donor Acceptor Recombination

Another technique of ODMR is the detection of the recombination luminescence of weakly coupled donor acceptor pairs. Donors D^0 can be described by $S = 1/2$. For a recombination luminescence donors and acceptors must be at least coupled weakly. In this case the energy level scheme of Figure 2.7 applies; the spins of the donor and acceptor can be parallel or antiparallel, which lead to four energy levels. The transition probabilities for the two triplet spin states into the singlet ground state is rather small compared to the two singlet-singlet transitions. Thus, there will be more electrons in the two triplet states. By inducing EPR transitions electrons can be shifted from these levels into the singlet states and thus the radiative transitions out of these levels are enhanced.

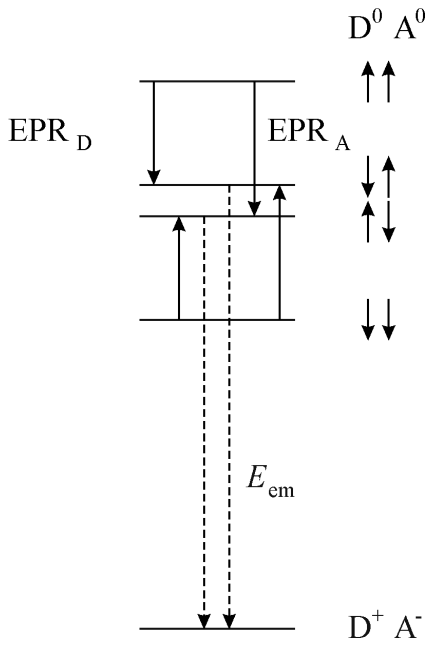

Figure 2.7: Level scheme for a weakly coupled donor acceptor pair.

The RL resulting from donor acceptor recombination created by UV light quenches in high magnetic fields what is due to polarization of the magnetic moments of the recombination centers. The probability W for a radiative recombination is given by

$$W = W_0(1 - P_1 P_2) \tag{2.3}$$

where W_0 is the probability of radiative recombination without external magnetic field; P_1 and P_2 are the polarizations of the spins of the donors and acceptors dependent on the magnetic field given by

$$P_i = \frac{1}{S_i} \frac{\sum_{n=0}^{2S_i} n e^{-gn\mu_B B/kT} - S_i \sum_{n=0}^{2S_i} e^{-gn\mu_B B/kT}}{\sum_{n=0}^{2S_i} e^{-gn\mu_B B/kT}} \tag{2.4}$$

where S_i is the spin of the corresponding recombination center; μ_B is the Bohr magneton; B is the external magnetic field. The recombination probability calculated for a $S_1 = S_2 = 1/2$ system is shown in Figure 2.8. It can be seen that the probability decreases significantly upon decreasing temperature and an increasing magnetic field.

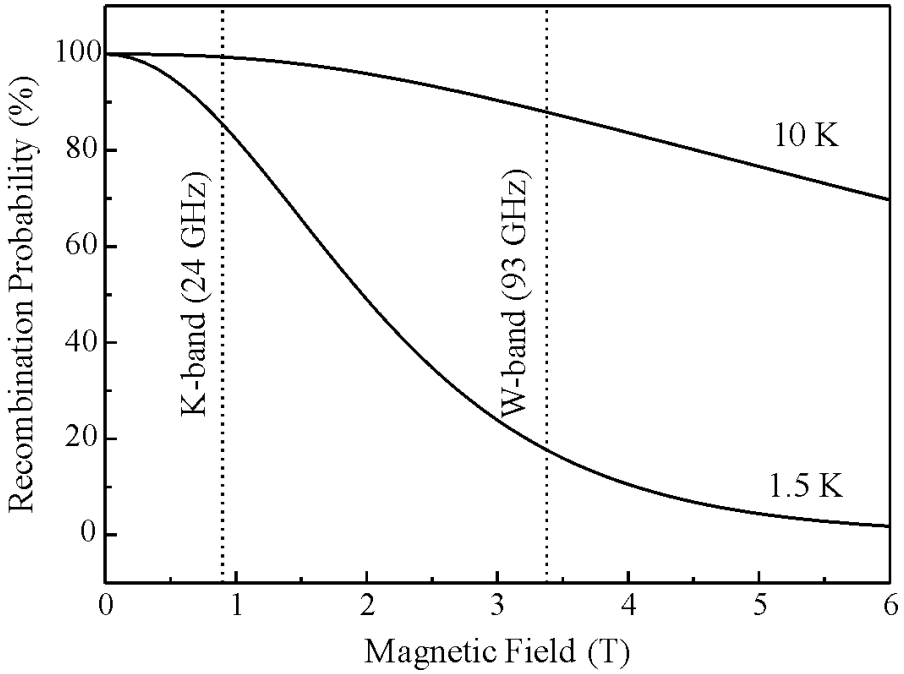

Figure 2.8: Theoretical dependence for the recombination at two centers with the g factors $g_1 = g_2 = 2$ and with the spins $S_1 = S_2 = 1/2$, T=1.5 K [9].

Thus it is essential to record the RL-EPR at low temperatures. Going to higher magnetic fields and thus to higher microwave frequencies leads to a higher enhancement of the RL due to the lower RL seen in higher magnetic fields.

2.3.3 Experimental Setup

A schematic diagram of a magneto-optical spectrometer for PL/RL-EPR measurements is shown in Figure 2.9. The main part of the spectrometer is an Oxford Instruments bath cryostat. The sample is placed in the middle of a superconducting magnet, which can provide magnetic fields up to 4 T. Excitation is carried out with a deuterium lamp and subsequent band pass or interference filters. The light emitted by the sample is detected in the integral luminescence with different available edge filters. The microwave field is coupled into the cavity via a coaxial conductor. The resonator can be varied by adjusting the bottom of the cavity.

Helium supply in the sample cavity is provided by a needle valve. In case of a helium filled sample cavity and a closed needle valve temperatures between 4.2 and 1.5 K can be achieved by vapor pressure reduction of the helium in the sample cavity.

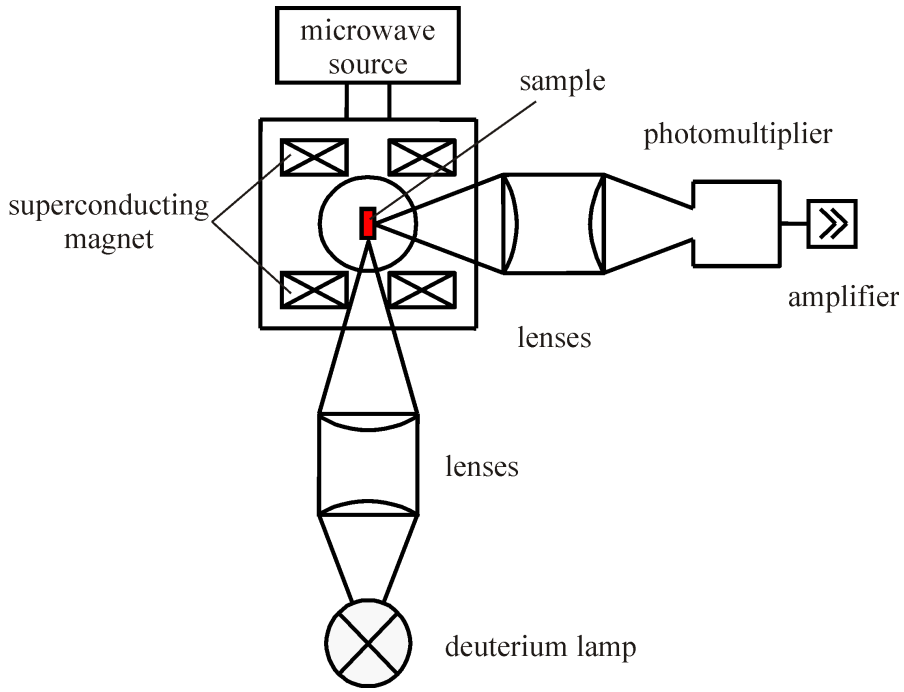

Figure 2.9: Schematic diagram of a magneto-optical spectrometer.

2.4 X-ray Absorption Spectroscopy

2.4.1 Extended X-ray Absorption Fine Structure Oscillations

In the following section a brief introduction into the spectroscopic use of x-ray absorption will be given. For further information the reader is referred to [10, 11]. Spectroscopic methods dealing with x-ray absorption are usually called EXAFS (Extended X-ray Absorption Fine Structure) or XANES (X-ray Absorption Near Edge Structure). These investigation origin from the fact, that the absorption edge of elements in a solid shows a significant fine structure. This fine structure gives information about the vicinity of the investigated atoms.

An incident x-ray beam can eject an electron from an atom. When this electron has an energy of more than 40 eV above the edge energy, the electron can be described as spherical wave. The wavelength $\lambda = 2\pi/k$ is described by

$$k = \sqrt{\frac{2m_e}{\hbar^2}(h\nu - E_0)} \tag{2.5}$$

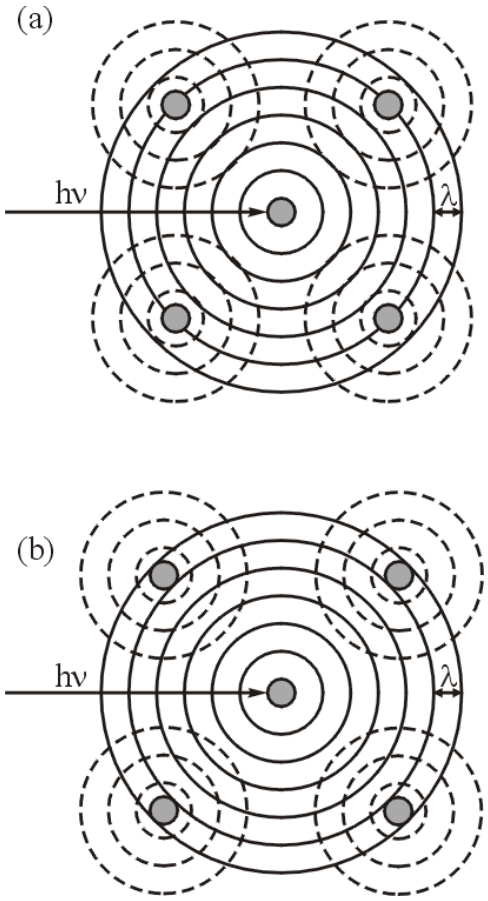

Figure 2.10: Scheme of the origin of the EXAFS oscillations (a) for a constructive interference of the incident and backscattered waves and (b) for a destructive one. Note, the distance between the absorbing and the scattering atoms is (a) $n\lambda$ and (b) $(2n+1)\lambda/2$.

where m_e is the electron mass, $\hbar$ Planck's constant, and E_0 the binding energy of the electron. This wave scatters at the surrounding atoms and these backscattered waves can interfere constructively or destructively with the original wave which influences the probability for the absorption of an incident x-ray beam. These effects are depicted schematically in Figure 2.10 for four neighboring atoms.

A typical x-ray absorption spectrum is shown in Figure 2.11 (a). For the analysis from the raw data a background function has to be subtracted. In addition this new function has to be normalized that most of the EXAFS part is close to a value of 1, see Figure 2.11 (b). By subtracting a value E_0 from the energy scale a pre-stage of the EXAFS-analysis is achieved. E_0 is the energy value where the normalized x-ray

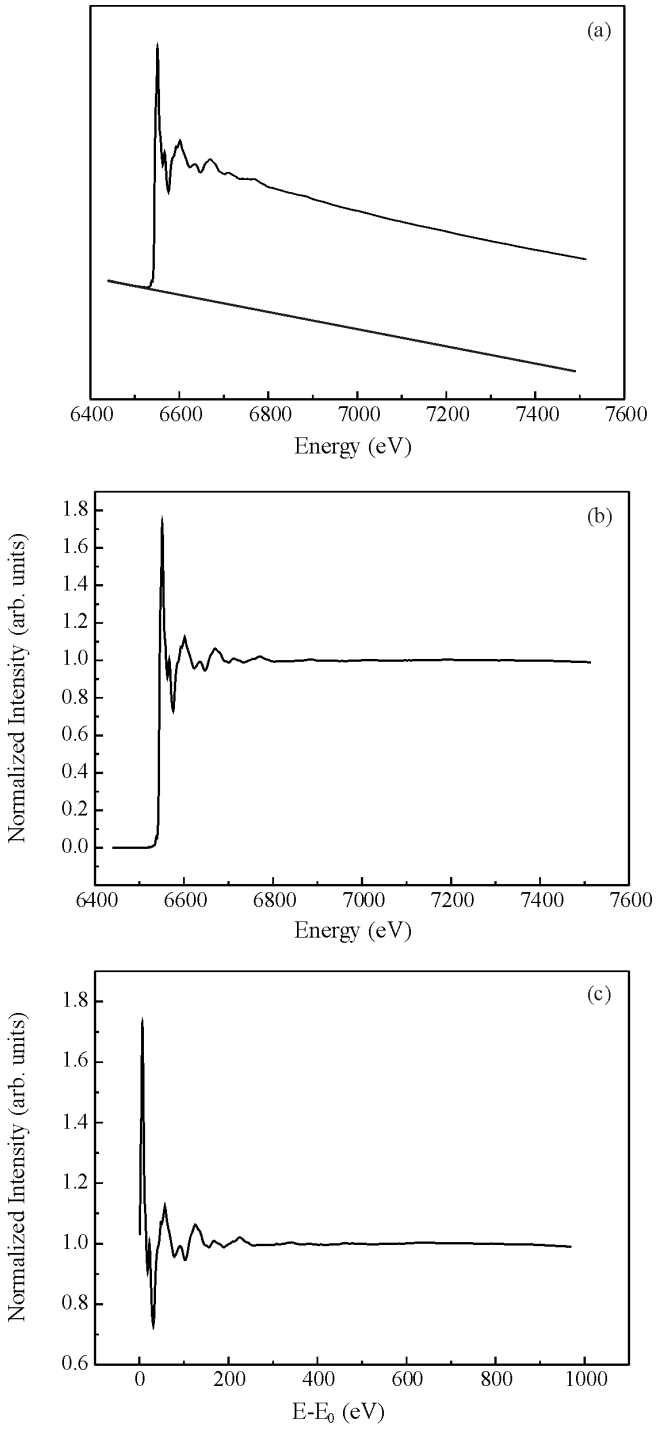

Figure 2.11: (a) X-ray absorption spectrum of MnF_2 and the corresponding background function. (b) Normalized x-ray absorption spectrum of MnF_2. (c) Pre-stage of the EXAFS analysis. E_0 is the energy value where the normalized x-ray absorption reaches a value of 1.

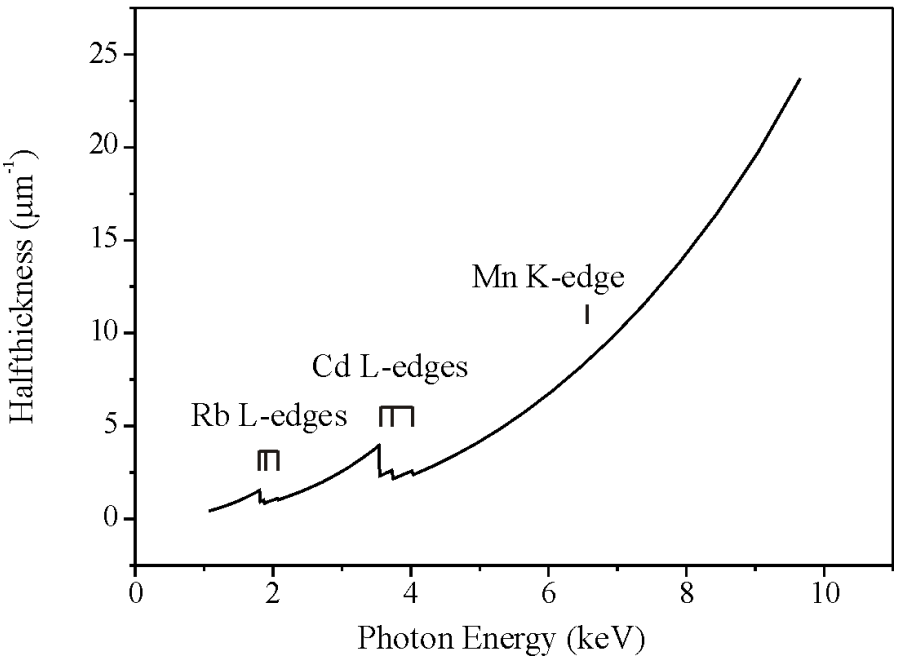

Figure 2.12: Half thickness of $RbCdF_3$.

absorption has a value of 1. These data can be transferred from energy into k-space by using Equation 2.5. To enhance these data for higher values of k it is possible to weight these data with $k^n (1 \leq n \leq 3)$. A Fourier transformation leads to a transformation from k-space into R-space. The spectra in R-space provide information about the type and number of atoms in the neighbor shells.

2.4.2 Experimental Details

The linear attenuation coefficient μ was estimated by using the data given by the National Institute of Standards and Technology [12]. The half thickness is given by $d_{1/2} = \ln 2/\mu$ and is shown for $RbCdF_3$ in Figure 2.12 for a density of 3.586 g/cm^3 [13]. The absorbance is given by

$$A = 1 - e^{-\mu d}. \tag{2.6}$$

Due to the high absorbance of $RbCdF_3$ at the Mn K-edge it is hardly possible to record EXAFS spectra of single crystalline $RbCdF_3$ with absorption technique. In this case a thin sample (≈ 50 μm) would be necessary. A different approach would be to crush a

small amount of the single crystals and press them in cellulose based pellets. But in order to keep the samples most of the measurements presented in this work were recorded in fluorescence mode. The experiments were carried out at the 5BM-D beamline of the Advanced Photon Source (Argonne National Laboratory). For detection a 12 channel Ge-detector was available.

3 The Perovskite $RbCdF_3$:Mn^{2+}

3.1 Crystal Structure

At RT $RbCdF_3$ has a perfect cubic structure (Figure 3.1, left side) with a tolerance factor of $t = 0.86$; the lattice parameter is $a = 4.399$ Å [14]. It shows a structural phase transition from [15] cubic (O_h^1) to tetragonal (D_{18}^{4h}) symmetry at $T = 124$ K (Figure 3.1, right side).

Rubidium has an oxidation state of +1 ($r = 1.47$ Å), cadmium +2 (0.97 Å) and fluorine −1 (1.33 Å) [16]. Since Mn is a divalent ion it substitutes for a Cd-ion [15] and is thus surrounded by a fluorine octahedron.

Single crystals of Mn-doped $RbCdF_3$ were grown in the Paderborn crystal growth laboratory using the Bridgman method with a vitreous carbon crucible, argon atmosphere and a stoichiometric mixture of CdF_2 and RbF powder to which 3, 100, 500, 2000, and 10000 ppm MnF_2 were added.

3.2 Photoluminescence

$RbCdF_3$:Mn^{2+} shows a luminescence maximum at 560 nm, which can be attributed to the Mn^{2+} impurity. This maximum can be seen in the PL and in the XL spectra (Figure 3.2 dashed curves). It is due to the radiative $^4T_{1g}(G) \rightarrow {}^6A_{1g}(S)$ transition of Mn^{2+} in an O_h crystal field symmetry [6, 8].

The PL excitation spectrum recorded before x-irradiation (Figure 3.2 (a), solid curve) shows several maxima, which are also typical for Mn^{2+} in an O_h crystal field. The excitation bands peak at 310, 332, 351, 396, 428, and 513 nm being transitions from the $^6A_{1g}(S)$ ground level to the excited levels $^4T_{1g}(P)$, $^4E_g(D)$, $^4T_{2g}(D)$, $^4A_{1g}(G)$ / $^4E_g(G)$, $^4T_{2g}(G)$, and $^4T_{1g}(G)$, respectively. The excitation band at 240 nm is probably caused by oxygen impurities or a double excitation of two Mn^{2+} ions [17].

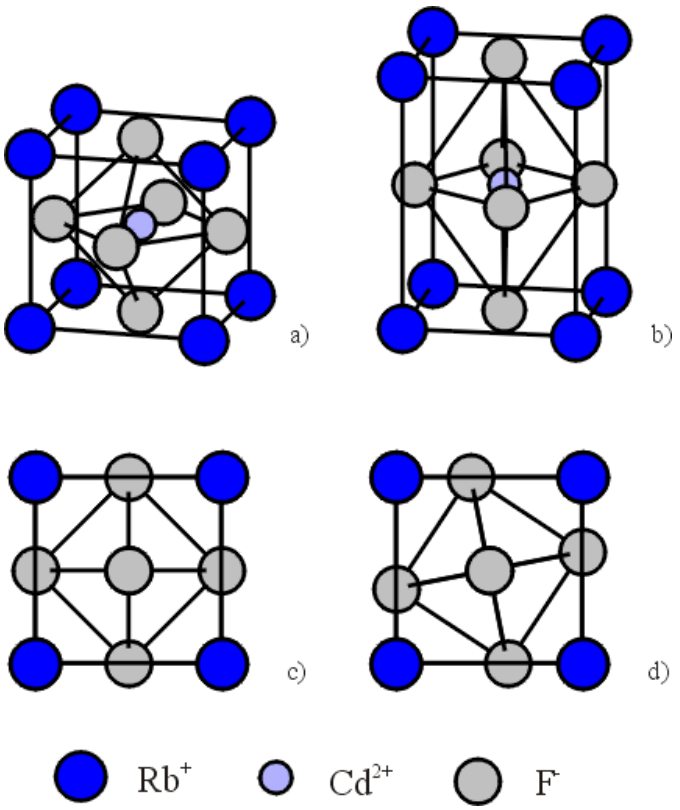

Figure 3.1: Crystal structure of $RbCdF_3$. a) The cubic and b) the tetragonal phase. The tetragonal phase exists at temperatures below 124 K. c) The cubic phase in the *ab*-plane. d) View on the *ab*-plane of the tetragonal phase.

After x-irradiation at RT the intensity of the Mn^{2+} emission is increased significantly (Figure 3.2 (b), dotted curves). The excitation spectrum (Figure 3.2 (b), solid curve) ranging from 200 to 550 nm shows an additional intense band peaking at about 300 nm. The Mn^{2+}-related excitation bands are superimposed by this radiation-induced band; the transitions to the $^4T_{1g}(G)$, $^4T_{2g}(G)$, and the degenerate $^4A_{1g}(G)$ and $^4E_g(G)$ energy levels can still be observed as weak peaks.

UV-irradiation into the band at 300 nm leads to a bleaching of the luminescence intensity. Figure 3.3 (a) shows the decay of the Mn^{2+} luminescence upon bleaching with a laser diode at 375 nm. The decay is not mono-exponential which indicates that there are different types of defects involved in the recombination process. UV-irradiation into the Mn excitation bands should lead to a constant PL signal, which can be observed for an excitation wavelength of 513 nm in Figure 3.3 (b). Contrary to this, irradiating into

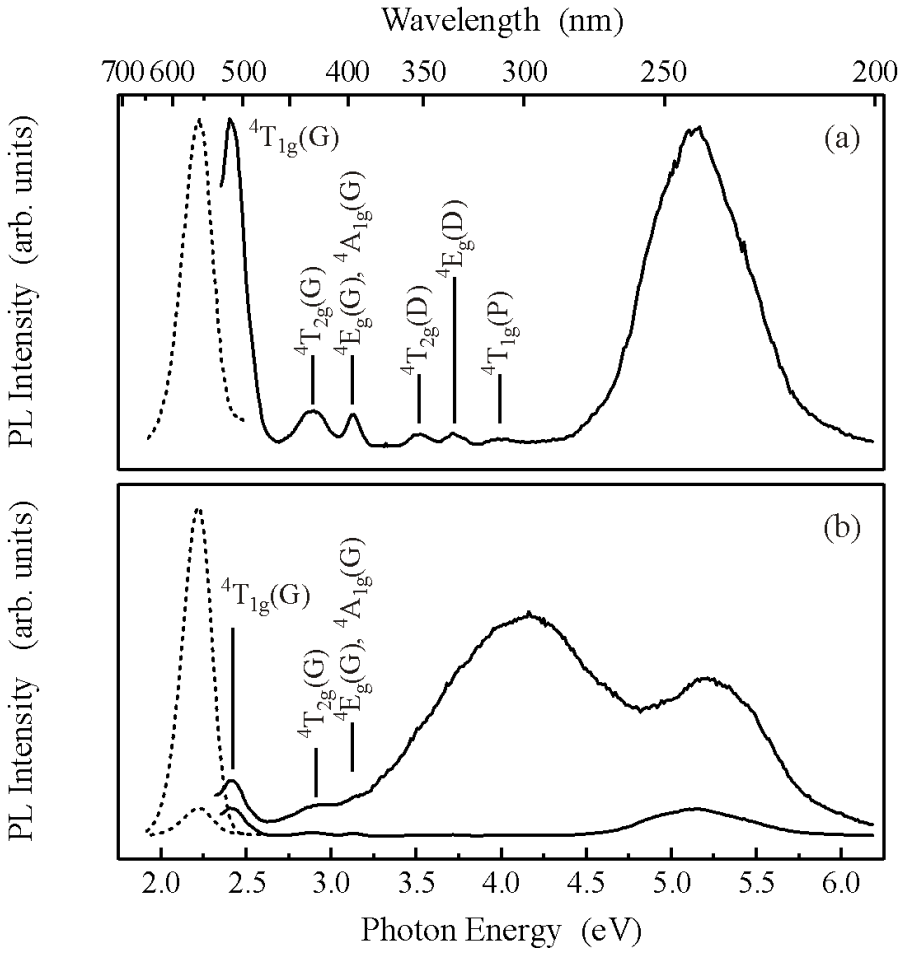

Figure 3.2: (a) PL emission (dotted curve) and excitation (solid) spectra of $RbCdF_3$ doped with 1% Mn^{2+}, recorded (a) before and (b) after x-irradiation (tungsten anode, 60 kV, 15 mA, 5 min). In (b) the spectra recorded before x-irradiation are shown for comparison. The PL was excited at 396 nm; the excitation spectra were detected at 560 nm.

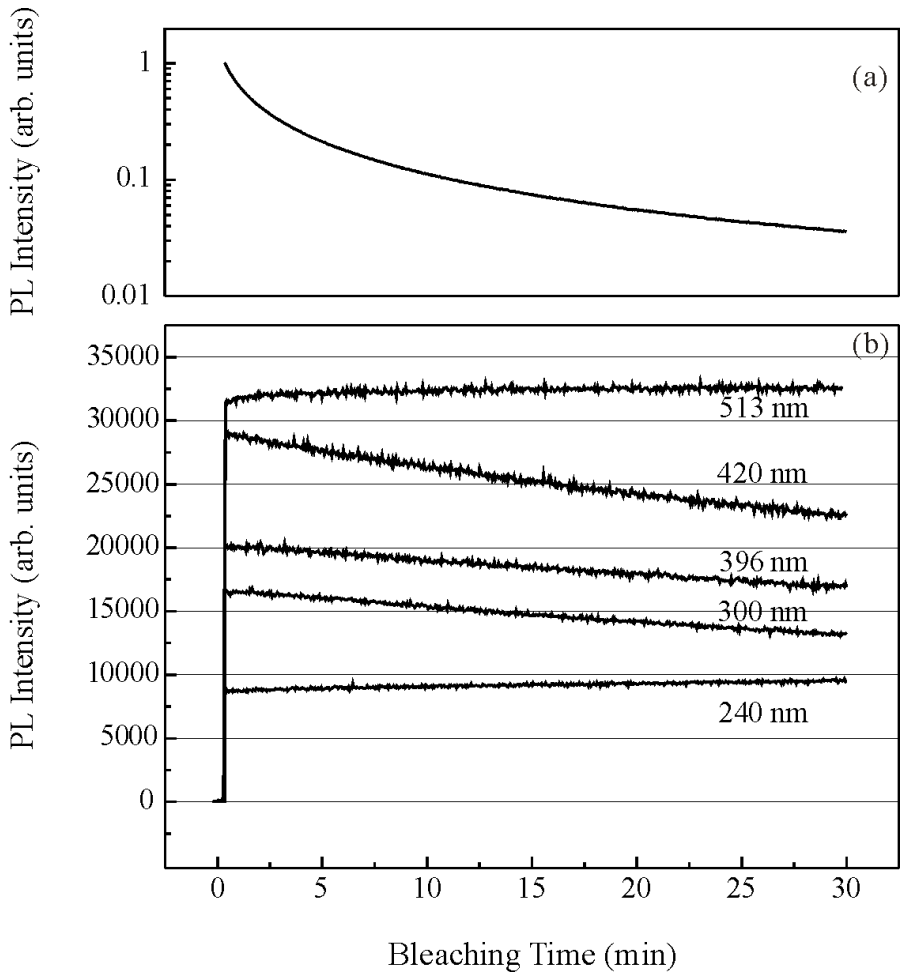

Figure 3.3: (a) PL intensity recorded for an excitation with a Laser-diode at 375 nm. (b) PL intensities for an excitation of a $RbCdF_3$ doped with 1 % Mn^{2+} sample with different wavelengths for a longer period of time. The PL was detected at 560 nm. All spectra were recorded at RT.

the Mn excitation bands at 396 and 420 nm leads to a fading of the PL signal. This effect is due to the broad new excitation band at 300 nm on whose low energy slope these bands are. In principle, for these experiments the largest bleaching effect should be observed for UV-irradiation into the 300 nm band but these measurements were made on the same sample and was x-irradiated only once.

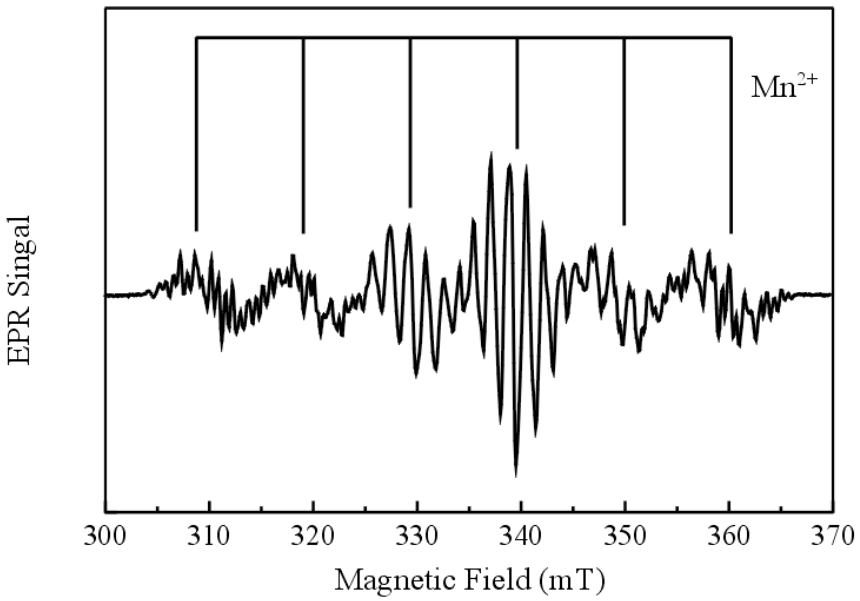

Figure 3.4: EPR spectrum of $RbCdF_3$ doped with 0.2 % Mn^{2+} recorded at RT in X-band (9.35 GHz).

3.3 Magnetic Resonance

3.3.1 Electron Paramagnetic Resonance

A typical EPR spectrum of a $RbCdF_3$:Mn^{2+} sample can be seen in Figure 3.4. In principle six groups of EPR resonance lines can be observed.

The ground state of Mn^{2+} has a half-filled d-shell, i.e., $S = 5/2$ and $L = 0$. Since $L = 0$ the g value should be close to the g value of the free electron; the g value was found to be $g = 1.99$. Additionally the g value and the Mn^{2+} hyperfine interaction (Mn has a nuclear spin of 5/2) are isotropic. The EPR spectra are dominated by the Mn^{2+} hyperfine interaction (A_{hf} (^{55}Mn)$/h = -271$ MHz), whereas the superimposed fine structure splitting due to the crystal field of cubic symmetry is rather small ($a_{\mathrm{cf}}/h =$ 14 MHz) [18]. The lines are additionally split by the superhyperfine interaction with the six nearest fluorine neighbors. The number of Mn^{2+} ions in the crystal can be extracted from the area under the EPR lines.

In Figure 3.5 the PL intensities and the EPR signal intensities for different doping levels are shown. Due to the fine structure splitting of the hyperfine groups the spectra

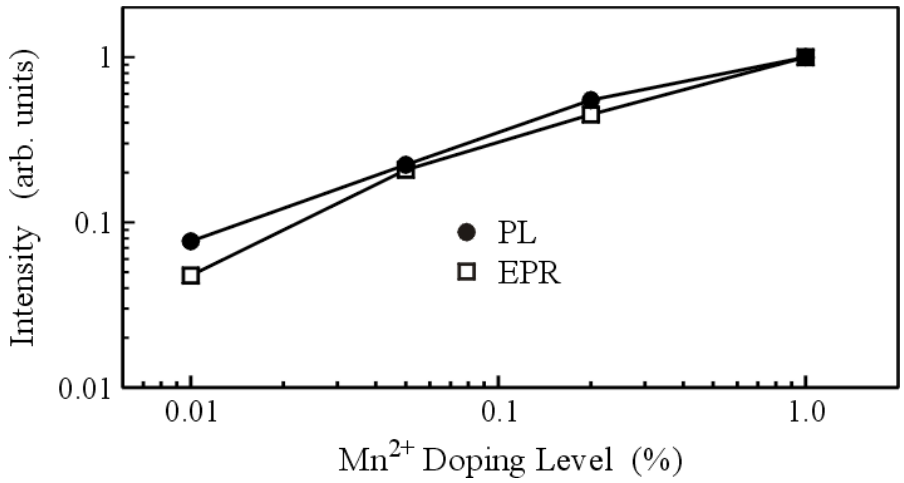

Figure 3.5: PL and EPR signal intensity of Mn^{2+} vs. Mn^{2+} doping level. The line is a guide to the eye.

change significantly for different orientations of the magnetic field. Thus the EPR data points were obtained by recording the spectra for different orientations of the magnetic field (in angular steps of 5°); the spectra were then integrated and averaged. It can be seen, that the Mn^{2+} luminescence is clearly related to the Mn^{2+} embedded in the crystal. Note, that the actual Mn^{2+} content may deviate from the doping level. It can be estimated by fitting the temperature dependence of the magnetization to the Curie-Weiss function. This was done in [19] for another set of Mn-doped $RbCdF_3$.

3.3.2 Optically detected Magnetic Resonance

Figure 3.6 shows a PL-EPR spectrum of a $RbCdF_3$ single crystal doped with 0.0003% Mn. The PL was excited at 1.5 K with the light of a deuterium lamp and a subsequent 212 nm interference filter and was detected in the integral emission using an edge filter KV 470. The spectrum was recorded in the K-band (27.73 GHz) as microwave-induced changes in the PL. It shows a broad resonance band at about 865 mT, which means a g value of g=1.99. In addition, a superimposed structure can be observed which it can be attributed to the Mn^{2+} hyperfine structure in $RbCdF_3$ [18]. Turning the sample away from this orientation leads to a decrease of the PL-EPR signal, i.e. this spectrum can only be observed in one specific orientation.

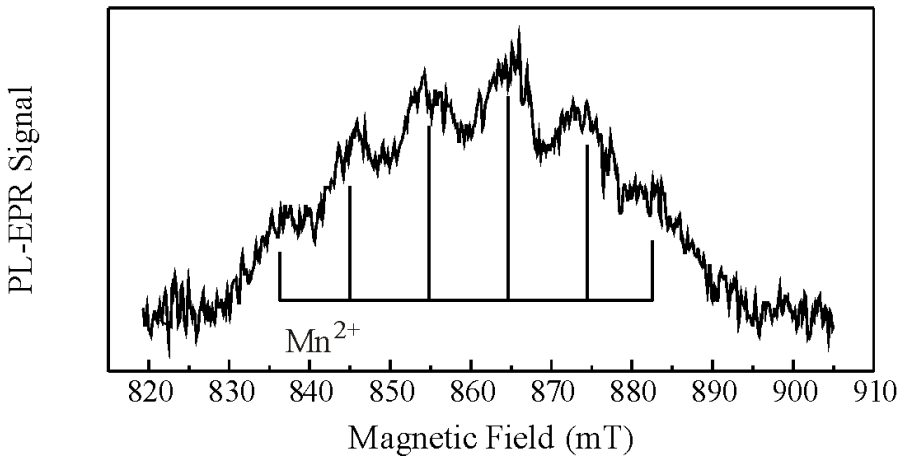

Figure 3.6: PL-EPR spectrum of 0.0003% Mn-doped $RbCdF_3$ crystal. The spectrum was recorded as microwave induces changes in the integral PL at 1.5 K applying a microwave frequency of 23.73 GHz. The PL was excited with a deuterium lamp and a subsequent 212 nm interference filter and detected in the integral luminescence with an edge filter (KV 470).

3.3.3 Electron Paramagnetic Resonance after x-irradiation

Figure 3.7 shows the change in the EPR signal intensity after x-irradiation for different periods of time. After intense x-irradiation the Mn^{2+} signal intensity could be reduced by 15-20% of its original value. As already mentioned above, the EPR data points were obtained by recording the spectra for different orientations of the magnetic field (in angular steps of 5°); the spectra were then integrated and averaged. The error bars are the root mean square deviation of the average value. As already observed by Dotzler et al. [19] a saturation effect can be found upon prolonged radiation. We did, however, not observe any resonance lines from the radiation-induced F centers. We assume that the Mn^{2+} EPR signal overlaps the (probably broad) F center resonance which can thus not be detected. The original Mn^{2+} EPR signal intensity can be restored upon bleaching with a laser diode (10 mW) at 375 nm (Figure 3.8).

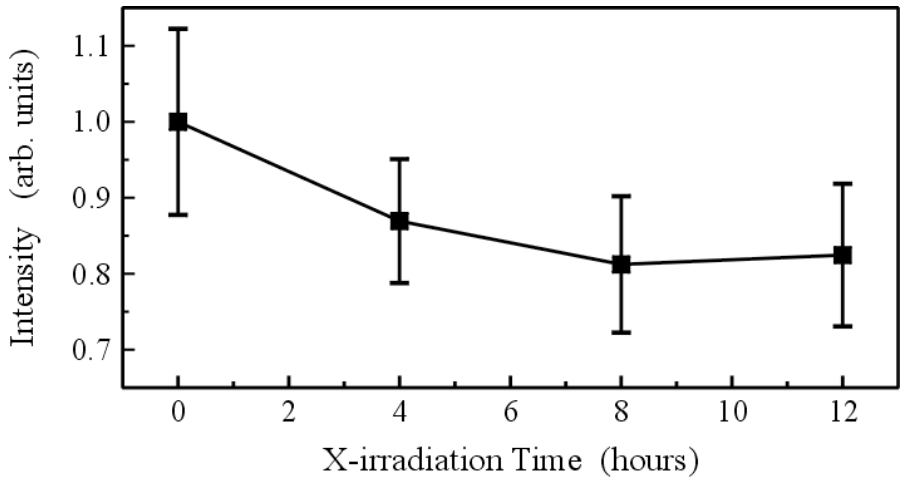

Figure 3.7: EPR signal intensity of Mn^{2+} in 0.0003% Mn-doped $RbCdF_3$ vs. x-irradiation time; the x-irradiation was carried out with a tungsten anode (50 kV, 30 mA). The line is a guide to the eye.

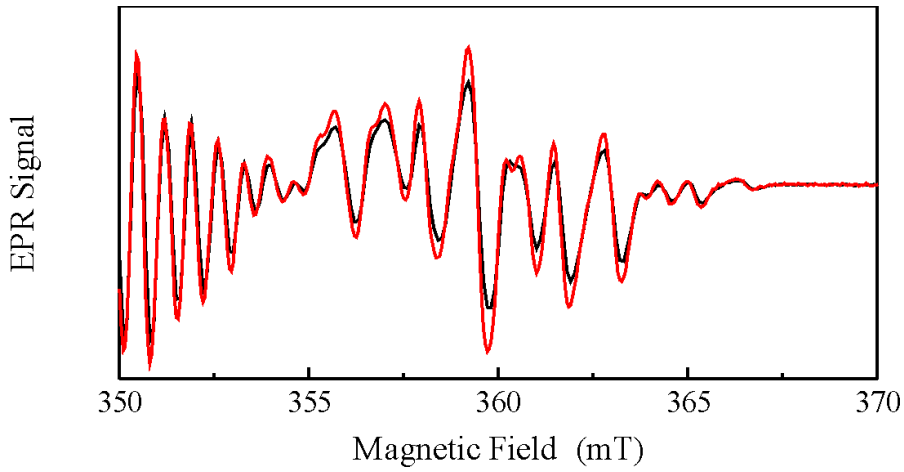

Figure 3.8: X-band EPR spectra showing one of the Mn^{2+} hyperfine groups in 0.0003% Mn-doped $RbCdF_3$. The spectra were recorded after 12 hours x-irradiation (black curve) and after subsequent bleaching with a laser diode at 375 nm (red curve). The bleaching was carried out in situ (inside the cavity), i.e., the spectra before and after bleaching were recorded using the same experimental conditions, in particular, the same orientation of the magnetic field.

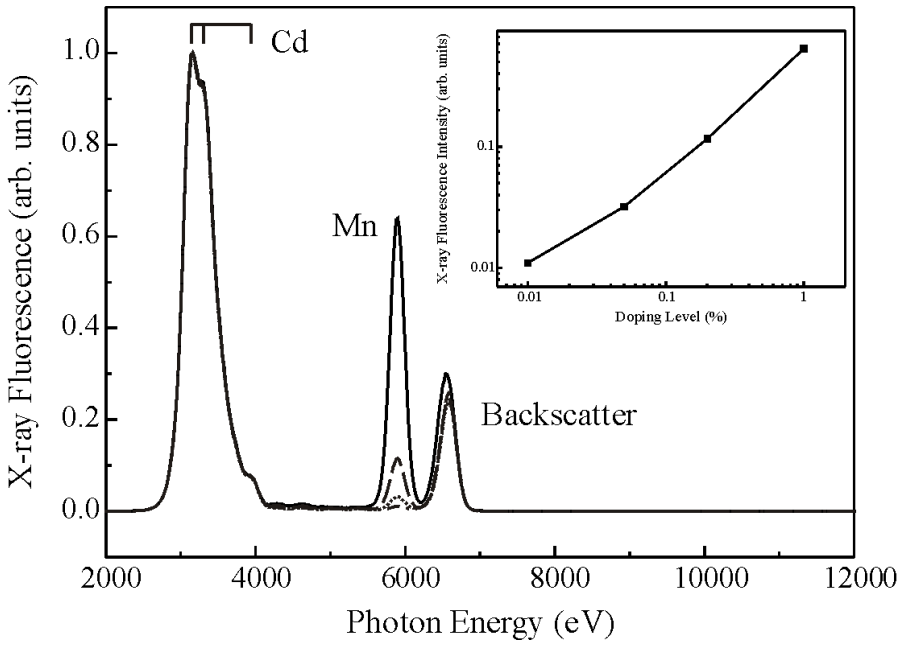

Figure 3.9: Normalized x-ray fluorescence of Mn-doped $RbCdF_3$. The doping levels are 1% (solid curve), 0.2% (dashed curve), 0.05% (dotted curve), and 0.01% (dash-dotted). As excitation a monochromatic x-ray beam with an energy of 6640 eV was used. The inset shows the peak values of the Mn x-ray fluorescence for different doping levels.

3.4 Beamline Experiments

3.4.1 X-ray Fluorescence

X-ray fluorescence spectra of $RbCdF_3$ with Mn doping levels of 1%, 0.2%, 0.05%, and 0.01% are shown in Figure 3.9. The strongest fluorescence peak is centred about 3200 eV, having smaller maxima at 3150, 3285, and 3935 eV. They are due to the Cd $L_{\alpha 1,2}$, $L_{\beta 1}$, and $L_{\gamma 2,3}$-transitions of the host lattice. The peak at 5880 eV can be attributed to the K-series of the Mn dopant, whereas the maximum at 6580 eV is the backscatter peak, which is an inelastic scattering of the exciting x-irradiation. The inset of Figure 3.9 shows the peak values of the Mn x-ray fluorescence versus doping level. It is apparent, that the value of the peak is related to the Mn doping level.

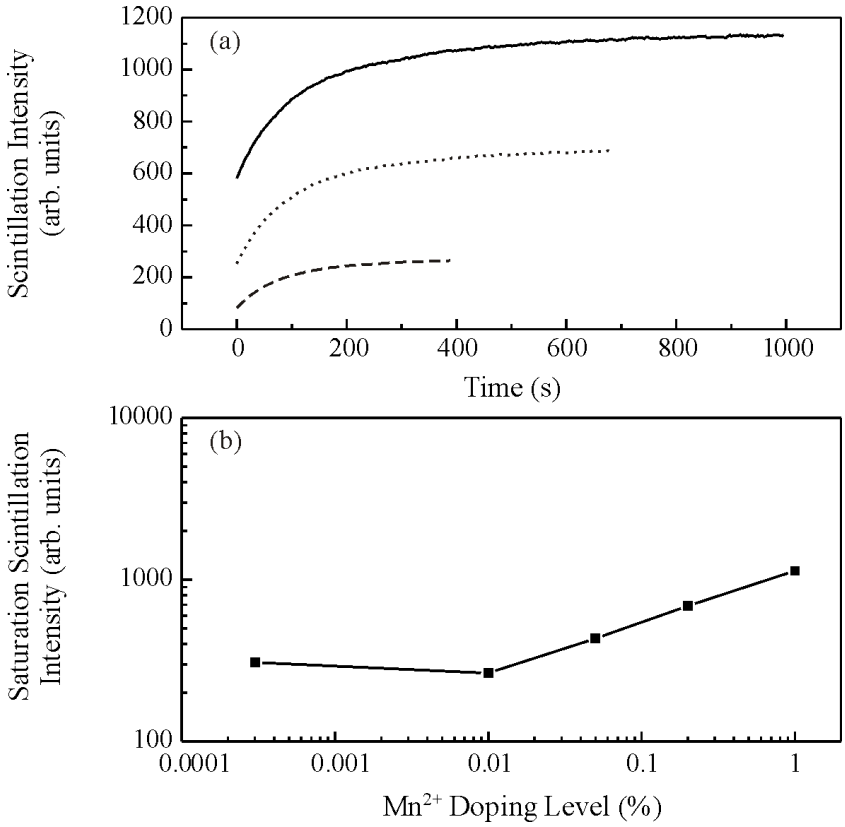

Figure 3.10: (a) Increase of the scintillation intensities in Mn-doped $RbCdF_3$ upon x-irradiation with a photon energy of 17 keV. The doping concentrations were 1% (solid curve), 0.2% (dotted), and 0.01% (dashed). (b) Saturation value of the scintillation intensities versus Mn^{2+}-doping level; full quares represent the experimental data points, the line is a guide to the eye.

3.4.2 Scintillation Intensity

In the following section the scintillation intensity of Mn-doped $RbCdF_3$ is described. The measurements were performed at the 5BM-C beamline of the Advanced Photon Source (Argonne National Laboratory). A 6 mm (horizontal) × 4 mm (vertical) monochromatic x-ray beam is used as excitation light source. The scintillation intensity of the sample is detected by a cooled charge-coupled device (CCD) camera through a 4X objective lens.

Continuous x-irradiation leads to an increased XL intensity. This effect is shown in Figure 3.10, where the samples where irradiated with x-rays having an energy of 17 keV. The different values at 0 s are due to the different doping levels of the samples, i. e. 1% (solid curve), 0.2% (dotted), and 0.01% (dashed). In Figure 3.10 (b) the saturation

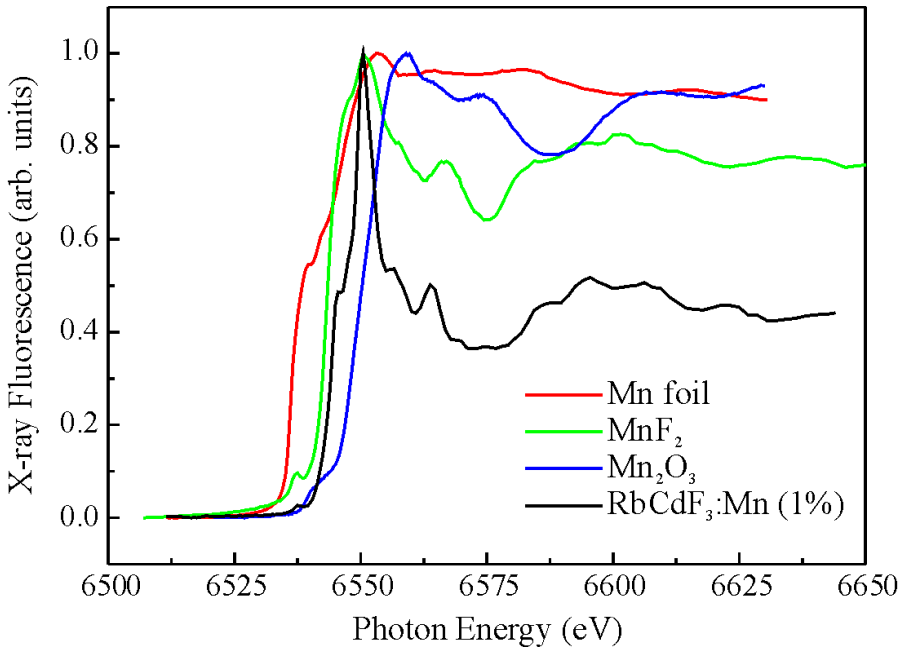

Figure 3.11: Normalized XANES spectra of 1% Mn-doped $RbCdF_3$ single crystal (black curve), Mn metal foil (red curve), MnF_2 powder (green curve), and Mn_2O_3 (blue curve). The spectra for $RbCdF_3$:Mn, Mn foil, and MnF_2 were recorded in fluorescence mode, the one for Mn_2O_3 was taken from [20].

value of the scintillation intensities is plotted. For highly-doped samples the saturation value of the scintillation intensity clearly corresponds to the Mn-doping level. The strong deviation from linearity for the 0.0003% Mn-doped sample is probably caused by the the crystal growth process, where possibly too much MnF_2 was added to the melt.

3.4.3 EXAFS on Mn-doped $RbCdF_3$

EXAFS spectra of different Mn compounds and $RbCdF_3:Mn^{2+}$ are shown in Figure 3.11. The highest absorption for Mn in $RbCdF_3$ is at 6550 eV, what corresponds to the highest absorption of the divalent Mn in MnF_2 lying also at 6550 eV. The absorption maxima of the metallic Mn foil is at 6553 eV and of trivalent Mn in Mn_2O_3 at 6559 eV. A normalized EXAFS spectrum of a 1% Mn-doped $RbCdF_3$ can be seen in Figure 3.12. The XANES spectra for 0.05%, 0.2%, and 1% doping levels of Mn in $RbCdF_3$ are shown in Figure 3.13 for comparison. All spectra show the same structure in their oscillations. There are only slight differences in the maximal values of the absorption oscillations. Due to the bad

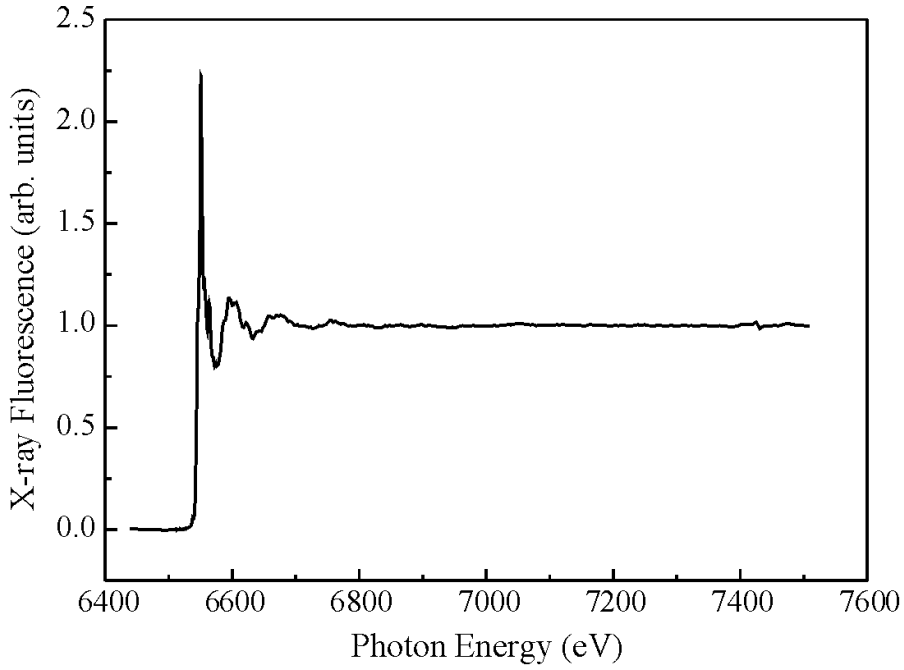

Figure 3.12: Normalized EXAFS spectrum of 1% Mn-doped $RbCdF_3$, recorded in fluorescence mode.

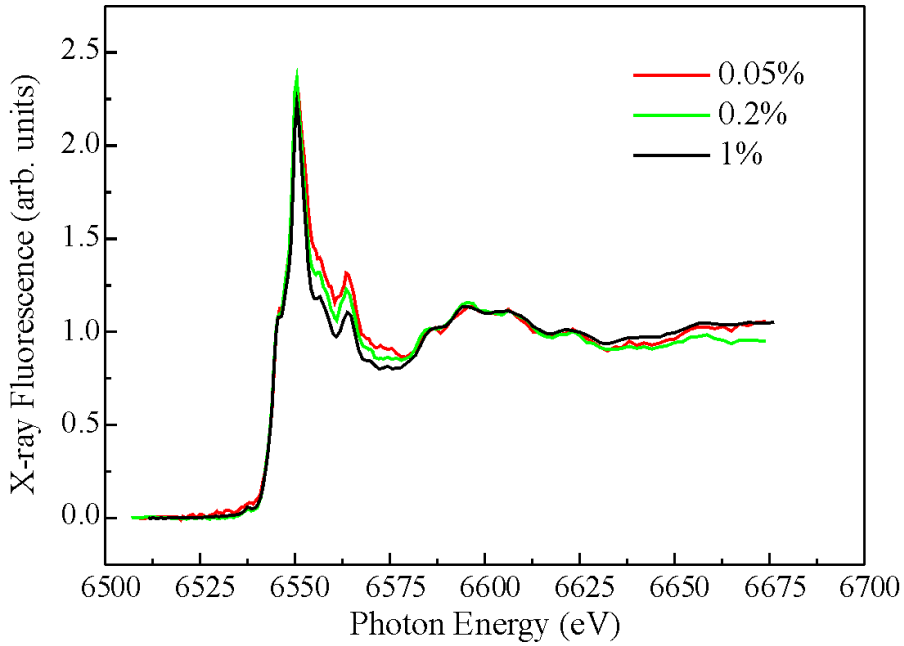

Figure 3.13: Normalized XANES spectra of Mn-doped $RbCdF_3$. The doping levels are 1% (black curve), 0.2% (green curve), and 0.05% (red curve). The spectra were recorded in fluorescence mode.

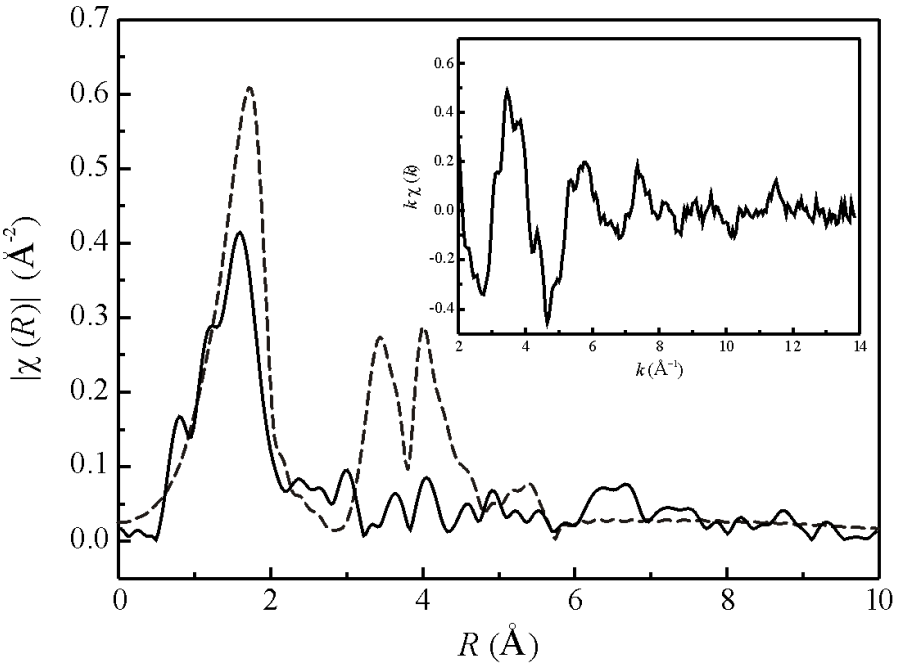

Figure 3.14: The solid curve shows the Fourier Transform of the Mn K-edge of Mn-doped $RbCdF_3$. The inset depicts the normalized k-weighted EXAFS. The solid lines are the experimental data and the dashed line is the simulation.

signal-to-noise ratio for the 0.2% and the 0.05% Mn-doped samples an EXAFS analysis could only be done for the 1% doped sample. The Fourier Transform of the Mn K-edge in $RbCdF_3$ is depicted in Figure 3.14 (solid curve), with the corresponding normalized k-weigthed EXAFS in the inset. A calculation is also shown in Figure 3.14 (dashed curve) for comparison. The calculation was carried out using the Artemis program of the Athena program package [21].

The most important paths for the calculated spectrum and their contribution to the total spectrum can be seen in Figure 3.15. Path one which is due to the six F^- ions lying in a <100> direction gives the most significant contribution to the Fourier Transform. Representatively one of the six ions is marked with 1. The second path is attributed to the 24 neighboring F^- pairs, marked with 2. Its contribution is much smaller and has an opposite sign with respect to path one, which leads to a dip at 3 Å in the total spectrum of paths one and two. The third path is due to eight Rb^+ ions lying in a <111> direction from the Mn core ion; this leads to the peak at 3.5 Å. The fourth peak at about 4.2 Å is due to a path from the core ion into a <100> direction to the 6 neighboring Cd^{2+} ions.

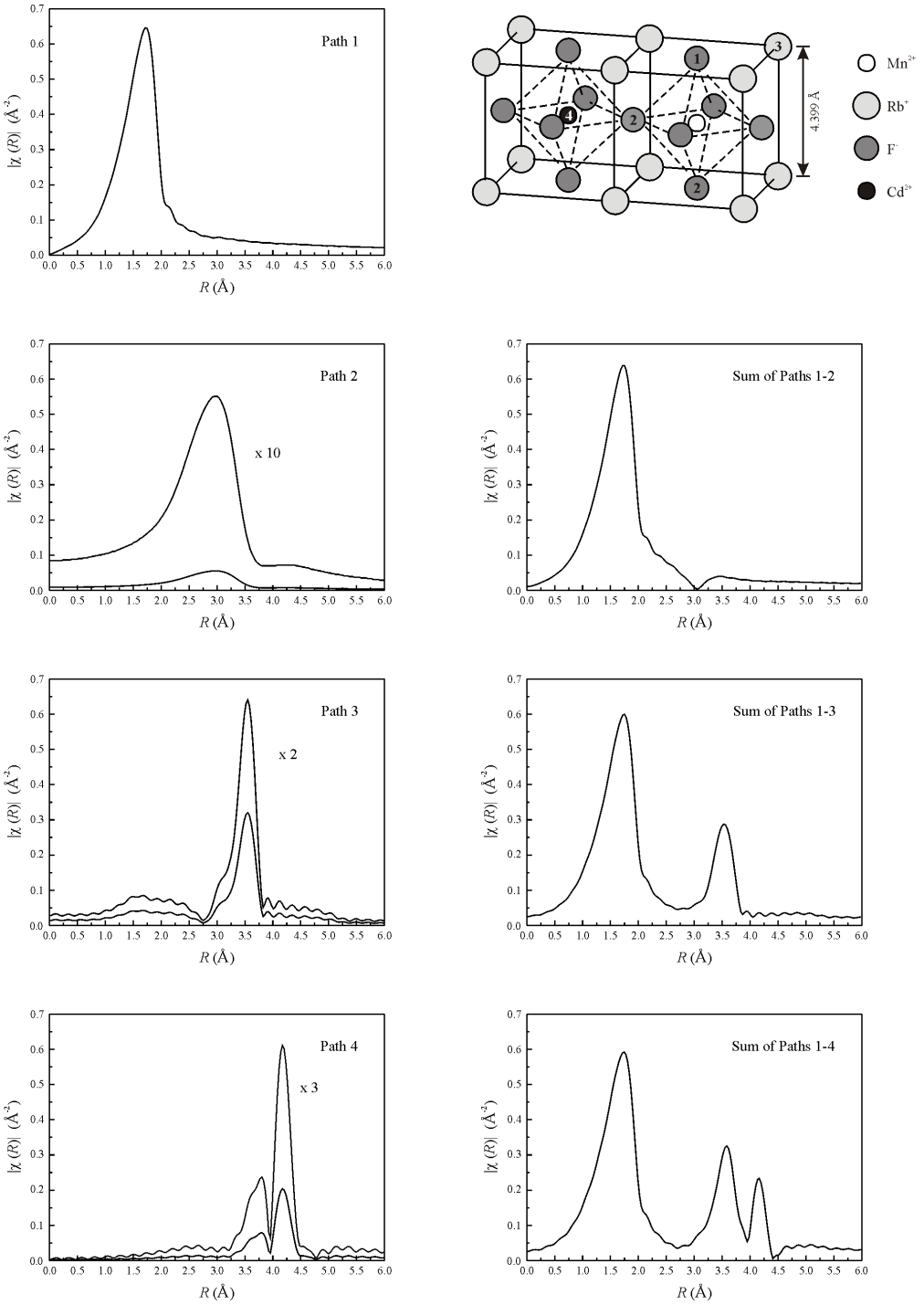

Figure 3.15: Fourier Transforms of the different paths as indicated in the model, see top right corner. The left side shows the Fourier transforms of the single path, the right side depicts the the sum of the corresponding paths.

3.5 Discussion

Mn-doped $RbCdF_3$ shows typical Mn^{2+} related PL emission and excitation spectra. The maximum at 230 nm is generally assumed to be due to oxygen impurities in the crystal. Another explanation was proposed by Ferguson [17]: The band at 230 nm could be due to a simultaneous electronic excitation of a pair of Mn^{2+} ions. Thus, the band could be an excitation of $^4T_{1g}(G)$ and $^4E_g(G)$ states.

Due to the charge state of the Mn dopant Mn^{2+} probably substitutes for divalent Cd. ENDOR measurements supported this idea [15]. This model was used for the calculation of EXAFS. It can be seen that the first and most intense shell can be attributed to the six F^- ions forming an octahedron around the Mn dopant. The second and the third shell are due to Rb and Cd ions, respectively. The experimental spectrum is in good agreement with the calculated spectrum, in particular for the fluorine neighbors. The shells attributed to Rb and Cd cannot be seen so clearly.

Losada et al. [2] found in Mn-doped $RbCdF_3$ after x-irradiation an absorption band at 310 nm. They also found an increased Mn^{2+} luminescence. They suggested that defects close to Mn^{2+} were created by x-irradiation. The defects perturb the Mn^{2+} environment. Because of this, the previously spin and parity forbidden transition get partially allowed and an enhanced Mn^{2+} luminescence can be observed. However, the same absorption band at 310 nm was also found in undoped $RbCdF_3$ after x-irradiation. Lifetime measurements of x-irradiated samples excited at 310 nm also made by Losada et al. [2] showed the same lifetime value as the unirradiated sample. This shows that the Mn^{2+} luminescence found in irradiated crystals comes from unperturbed Mn^{2+} ions. Since the 310 nm absorption band is caused by intrinsic defects (F-centers) but the emission is due to Mn^{2+} ions, there is probably an energy transfer between these intrinsic defects and the manganese. It was suggested by Losada et al. and in recent work from Dotzler et al. [19] that x-irradiation produces Mn^{3+} ions and electron trap centers (F-centers). Upon optical excitation of the radiation-induced absorption band the trapped electron is released and recombines with a Mn^{3+} ion in the vicinity, followed by a Mn^{2+} emission. The bleaching effect is thus related to the destruction of the defect centers created during x-irradiation.

After x-irradiation the PL excitation spectrum shows that the excitation bands at 297 and 345 nm are more enhanced than the other bands. In case of a perturbed Mn environment an enhancement of all Mn^{2+} excitation bands would be expected. But as

only two excitation maxima are enhanced, this increase is possibly not associated to the perturbation produced by defects close to the Mn^{2+} ions but to the fact that the absorption band at 310 nm superimposes the excitation spectrum. Therefore, it is likely that it is due to energy transfer between these intrinsic defects and the manganese ion, as mentioned above.

The bleaching effect, seen in Figure 3.3, where the bands at 396, 343 and 293 nm show a decreasing PL intensity, is probably related to the destruction of defect centers created during X-irradiation [22]. The EPR measurements showed that the number of Mn^{2+} ions is reduced by X-irradiation and can be restored by optical bleaching. This agrees with the model suggested by Dotzler et al. [19] that optically stimulable Mn^{3+}-F complexes are formed by X-irradiation.

4 EXAFS on Eu-doped CaF_2

A comparable problem like Mn^{2+} in $RbCdF_3$:Mn is Eu^{2+} in CaF_2. The crystal structure of CaF_2 is shown in Figure 4.1. The dopant is located in the center of a fluorine cube. Different vacancies and impurities were discussed for this compound. In the following section preliminary results of EXAFS measurements made at the Advanced Photon Source (APS) and at HASYLAB are shown.

4.1 Advanced Photon Source

The x-ray fluorescence spectrum of 2% Eu-doped CaF_2 is shown in Figure 4.2. It shows three emission peaks at 3690, 5850, and 6870 eV, which can be attributed to transitions of the Ca K-series, Eu $L_{\alpha 1,2}$ line and backscattered x-rays (x-rays inelastically scattered at the sample onto the detector), respectively. The normalized fluorescence Eu L_{III}-edge and Eu L_{II}-edge EXAFS spectra are shown in Figure 4.3. The corresponding k-weighted EXAFS of the Eu L_{III}-edge (inset) and the Fourier transform spectrum are shown in Figure 4.4; the analysis was done using the Athena Software [21]. There are two dominant shells at approximately 1.7 and 3.5 Å.

4.2 HASYLAB

Comparable experiments were also performed at the E4 beamline of HASYLAB in Hamburg. In contrast to the previous measurements these spectra were recorded in absorption. Approximately 10 mg of 0.1% and 2% Eu-doped CaF_2 were crushed and mixed with a cellulose powder. These were afterwards pressed in pellets, which were used for the experiments.

The x-ray absorption spectrum of 2% Eu-doped CaF_2 can be seen in Figure 4.5 (black curve). In principle, it shows the same features as the spectra recorded at the APS

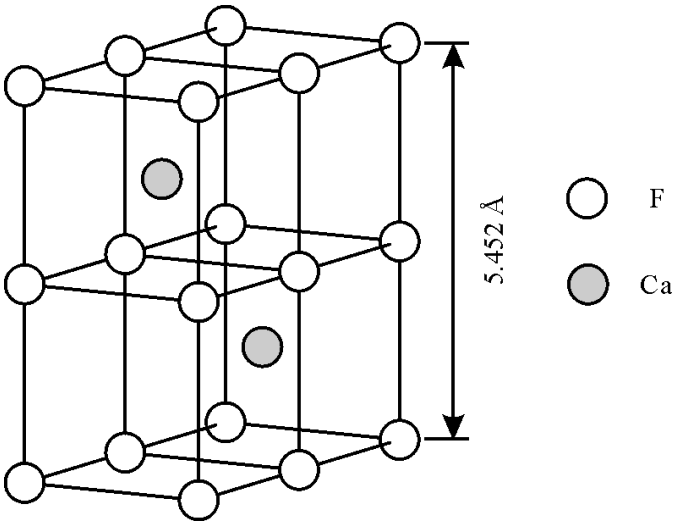

Figure 4.1: Crystal structure of CaF_2. The ionic radii are Ca^{2+} 0.99 Å, Eu 1.09 Å, and F 1.33 Å.

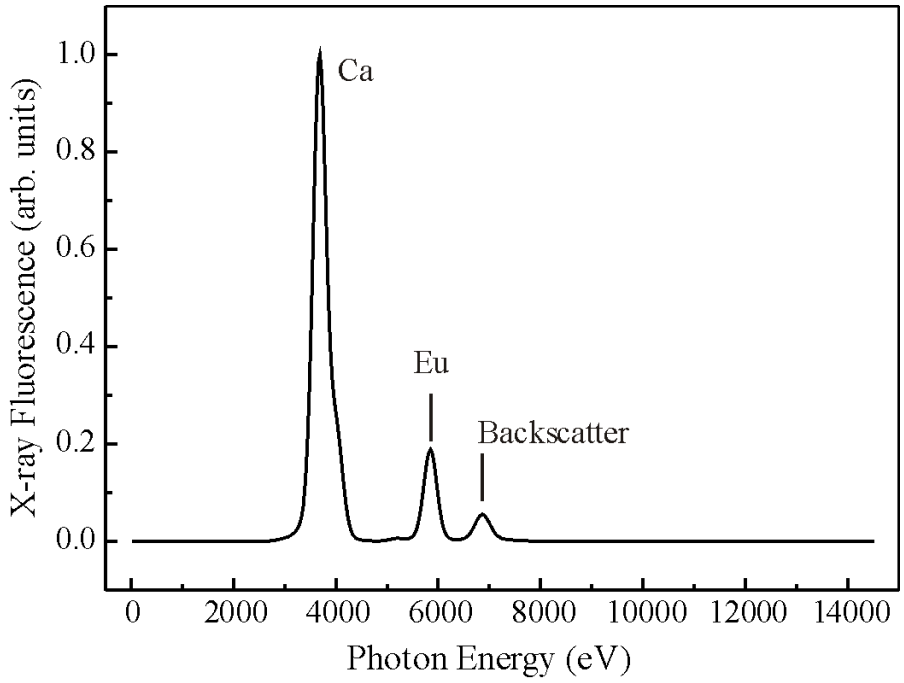

Figure 4.2: Normalized x-ray fluorescence spectrum of 2% Eu-doped CaF_2, recorded for an excitation energy of 7080 eV.

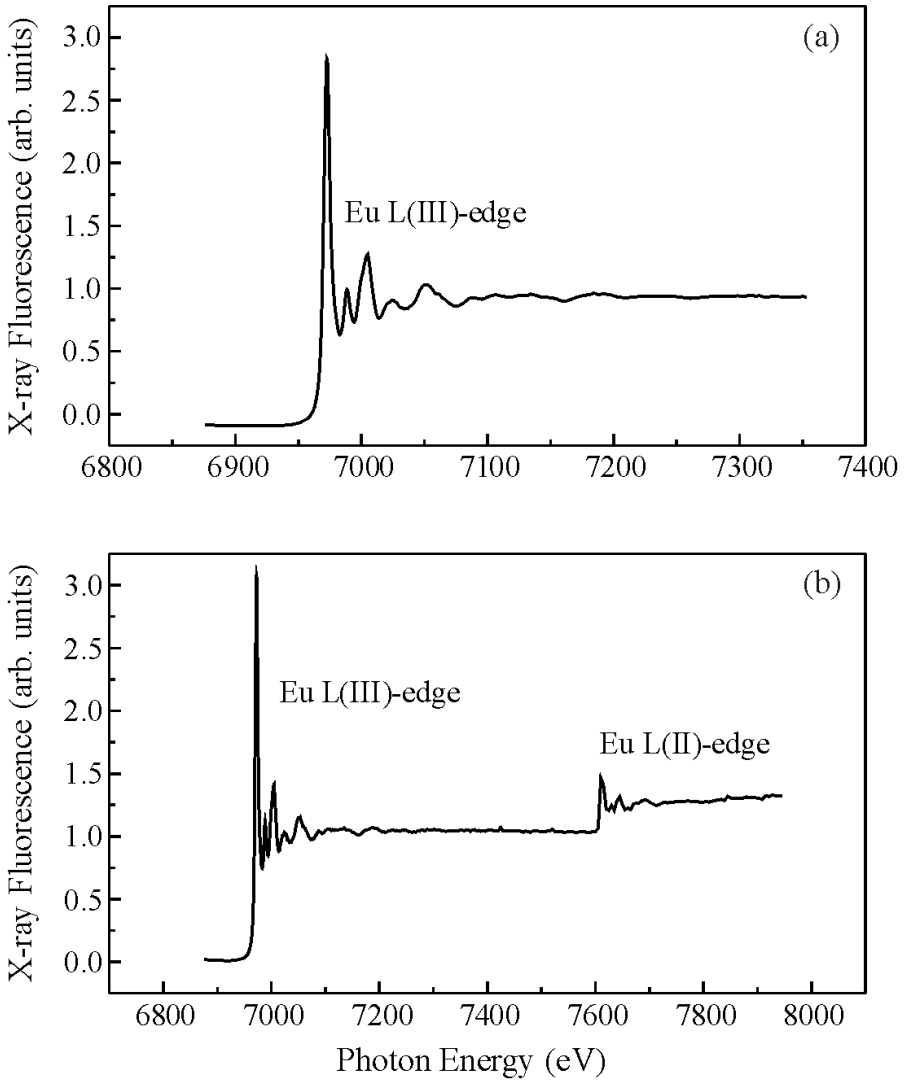

Figure 4.3: (a) Normalized EXAFS spectrum of 2% Eu-doped CaF_2 at the Eu L_{III}-edge and (b) at the Eu L_{II}-edge, recorded in fluorescence mode.

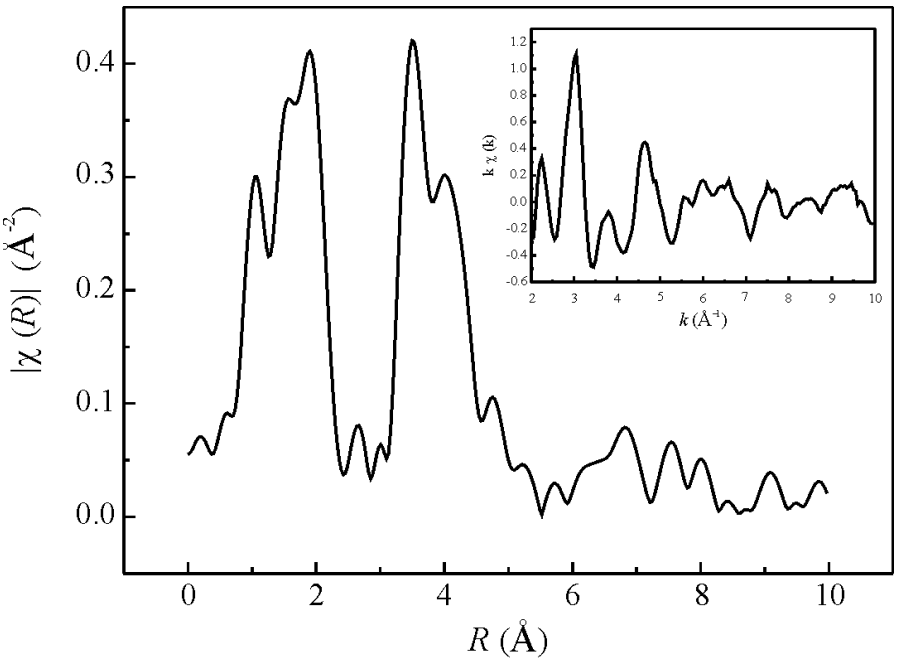

Figure 4.4: Fourier transform of the Eu L_{III}-edge in 2% Eu-doped CaF_2. The inset shows the normalized EXAFS (k) weighted of the Eu L_{III}-edge in 2% Eu-doped CaF_2.

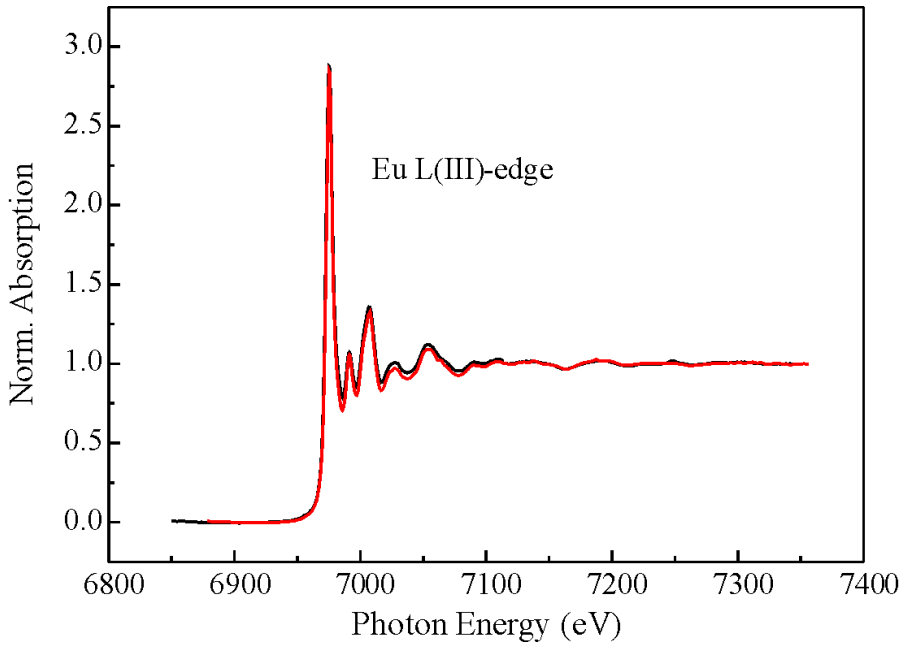

Figure 4.5: Normalized EXAFS spectrum of 2% Eu-doped CaF_2 at the Eu L_{III}-edge, recorded in absorption (black curve). The spectrum recorded in fluorescence mode at the APS is shown for comparison (red line).

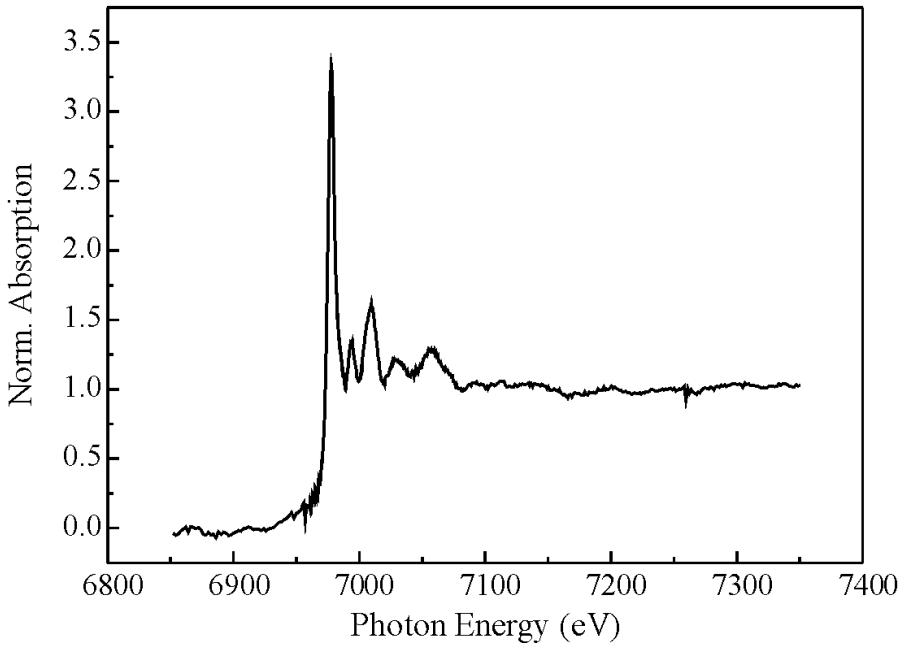

Figure 4.6: Normalized EXAFS spectrum of 0.1% Eu-doped CaF_2 at the Eu L_{III}-edge, recorded in absorption.

(red curve), which was further supported by a preliminary analysis of this experiment. Despite the weaker beam intensity the HASYLAB absorption spectra of the 2% Eu-doped sample have a similar signal-to-noise ratio as the spectra recorded in fluorescence mode at the APS.

The x-ray absorption spectrum of 0.1% Eu-doped CaF_2 is shown in Figure 4.6. Although the signal-to-noise ratio is much weaker than that for the 2% doped sample the EXAFS spectrum shows similar oscillations as already seen in Figure 4.5 for the 2% doped sample.

The absorption setup at the E4 beamline at HASYLAB allowed to record the x-ray absorption of a 0.1% Eu-doped CaF_2 sample in a relatively good signal-to-noise ratio. For further experiments, EXAFS spectra should preferably be recorded in absorption instead of fluorescence mode.

4.3 Discussion

Calculations of the Fourier transform were performed with the Artemis program [21] package and are shown in Figures 4.7, 4.8, and 4.9. The models used for the calculations are shown as well; these show only the nearest neighbors of the Eu^{2+} dopant. The white circles represent F^- ions, the gray ones Eu^{2+} ions, the black ones O^{2-} ions; the boxes are F-vacancies.

The calculations for an unperturbed Eu^{2+} dopant in CaF_2, with one F-vacancy and a combination of one F-vacancy with one O^{2-} impurity are shown in Figure 4.7. The most significant difference in the spectra can be seen in the first shell at approximately 1.7 Å. An F-vacancy leads to a decrease of this peak, whereas an O^{2-} ion does not affect the Fourier transform considerably. In Figure 4.8 the possible combinations of two F-vacancies are shown. In principle there are three ways to arrange an F-vacancy pair: Along <100>, along <110> and along <111>. All three configurations show the same Fourier transform, thus it is not important, which two F^- ions are missing from a possibility of six. Compared to the Fourier transform of an Eu-v_F complex in CaF_2 the complex consisting of two F-vacancies shows a much lower peak at 1.7 Å; i.e. the less F-ions in the vicinity of a Eu^{2+} ion the smaller the first shell.

In [23] different models of the surrounding of an Eu-dopant in CaF_2 have been presented. Three of them and their Fourier transform are shown in Figure 4.9. The figure illustrates, that the most significant changes in the spectra are due to the number of missing F^--ions. The height of the first peak decreases with decreasing number of surrounding F^--ions. In contrast an increasing number of substituting O^{2-}-ions leads only to a slight increase of the second and third shell at 3.5 Å and at 3.9 Å, respectively.

At this point, the analysis indicates that a complex consisting of two fluorine vacancies in the vicinity of an Eu^{2+} ion leads to the EXAFS spectrum observed. A statement about the positions of the fluorine vacancies cannot be made. However, this interpretation is questionable since recent Mössbauer investigations on Eu-doped CaF_2 [24] showed, that oxygen neighbors do not play such a dominant role as suggested in [23][1].

[1] Furthermore this assumption is supported by a work published after completion of this thesis [25]. The Eu-ion seems to be in an cubic surrounding with no pertubation in the vicinity.

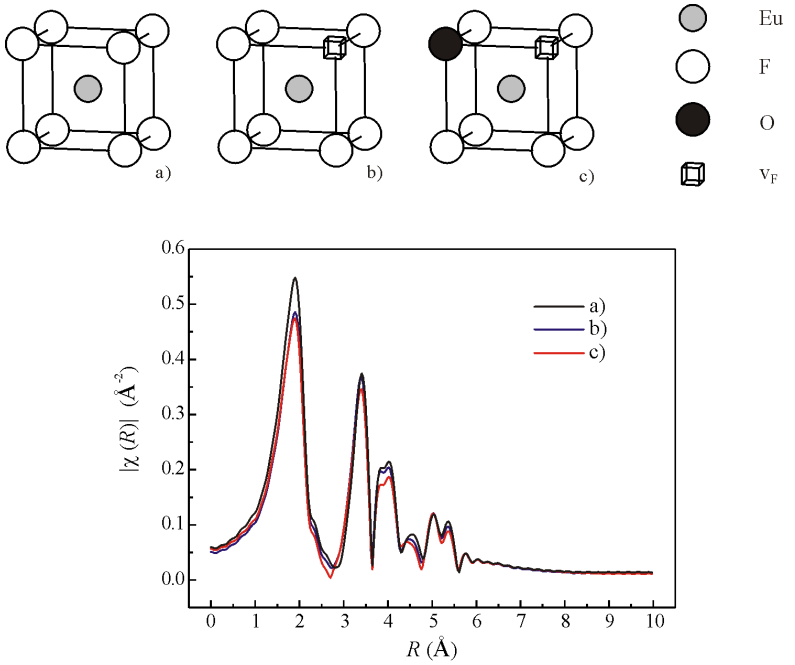

Figure 4.7: Model and Fourier transform of the Eu L_{III}-edge in 2% Eu-doped CaF_2.

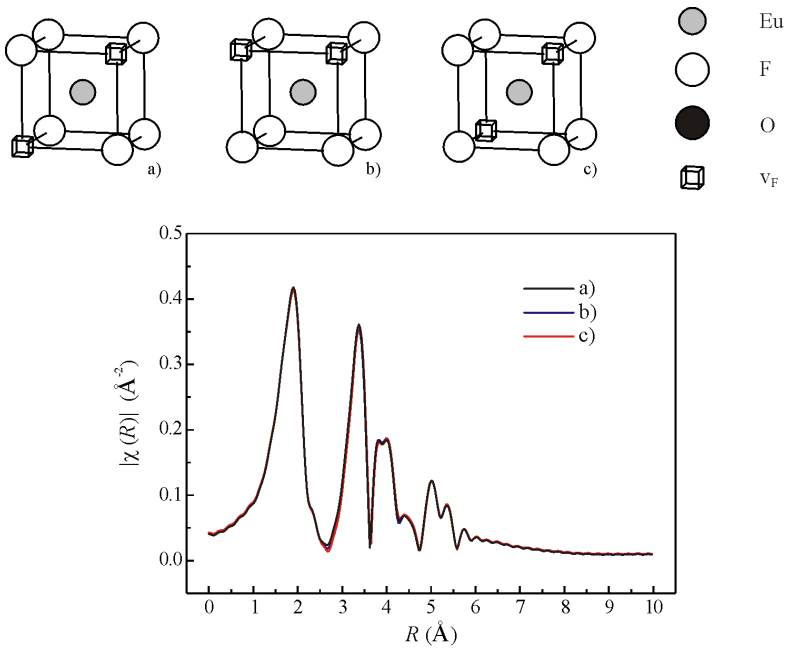

Figure 4.8: Model and Fourier transform of the Eu L_{III}-edge in 2% Eu-doped CaF_2.

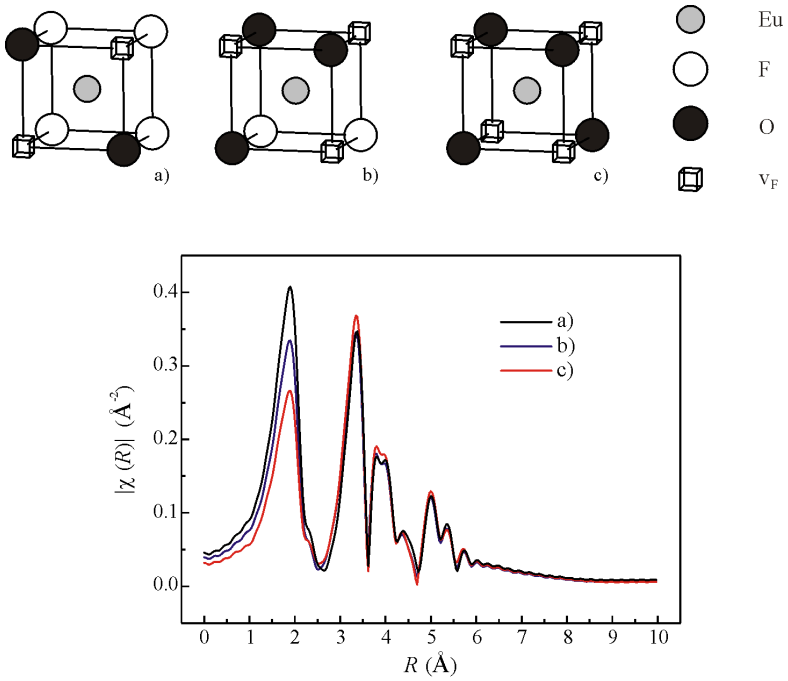

Figure 4.9: Model and Fourier transform of the Eu L_{III}-edge in 2% Eu-doped CaF_2.

5 The Inverse Perovskite $LiBaF_3$

5.1 Crystal Structure

$LiBaF_3$ is very different from the other crystals discussed earlier. Lithium has an oxidation state of +1 ($r = 0.68$ Å) and barium of +2 (1.34 Å) [16].

Since $LiBaF_3$ has a tolerance factor of 0.94, it has a cubic perovskite structure. It has no distortions even at low temperatures [26] and the lattice parameter has a value of $a = 3.995$ Å [26].

However, the structure of $LiBaF_3$ is different from that of $RbCdF_3$. It has a so-called inverse perovskite structure [27]. The monovalent Li^+ ion is surrounded by a fluorine octahedron and Ba^{2+} is surrounded by 12 fluorines.

Although Mn^{2+} has the same charge as Ba^{2+} it does not substitute for the Ba ion. Yosida [28] showed that the Mn^{2+} ion substitutes for the Li^+ ion, which is surrounded by a fluorine octahedron. This is the same as in the other samples. Mn^{2+} is located on the Me site in Figure 2.1 and so it has the same environment as Mn^{2+} in the other two crystals.

Single crystals of Mn-doped $LiBaF_3$ were grown in the Paderborn crystal growth laboratory using the Bridgman method with a vitreous carbon crucible, argon atmosphere and a stoichiometric mixture of LiF and BaF_2 powder to which 2000 molar ppm of MnF_2 were added.

5.2 X-ray Fluorescence

The X-ray fluorescence spectrum of 0.2% Mn-doped $LiBaF_3$ shows several maxima, see Figure 5.1. The peaks at 4460, 4840, 5140, and 5540 eV can be allocated to transitions of the L-series of Bai; i.e. $L_{\alpha 1,2}$, $L_{\beta 1}$, $L_{\beta 2}$, and $L_{\gamma 1}$. The Mn K-series can only be seen as shoulder of the Ba L-series at 5780 eV. The backscatter peak can be found at 6540 eV.

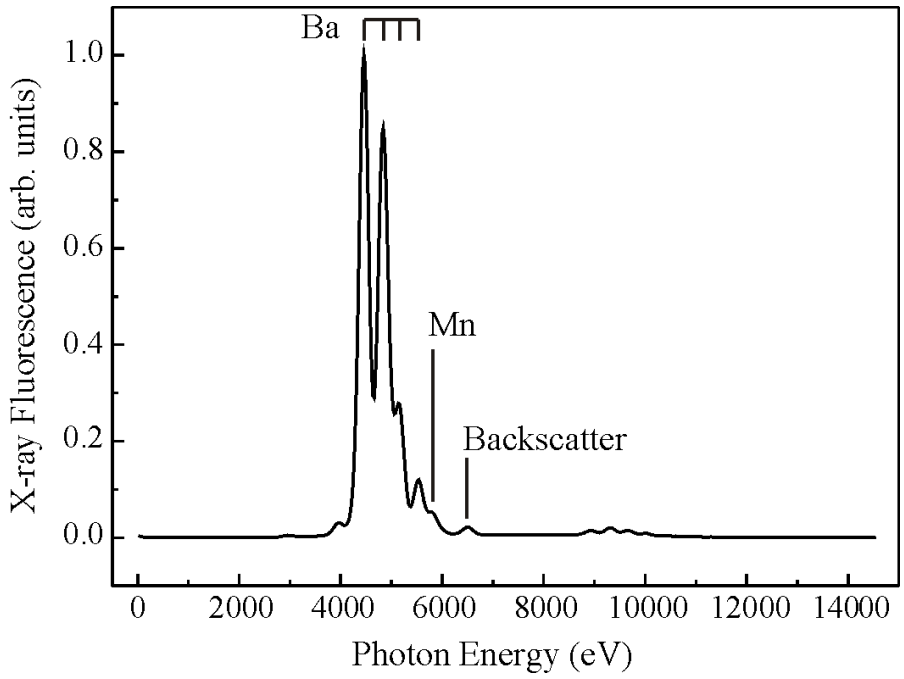

Figure 5.1: Normalized x-ray fluorescence of 0.2% Mn-doped $LiBaF_3$. For excitaion a monochromatic x-ray beam with an energy of 6640 eV was used.

5.3 Oxygen Vacancy Complex

Mn^{2+} emits at 712 nm and has a characteristic excitation spectrum. After x-irradiation the magnetic circular dichroism (MCD) of the optical absorption indicated that an F-type center interacts with the Mn^{2+} dopant.

In oxygen-doped $LiBaF_3$ Shiran and Voronova [29] found a luminescence band peaking at 420 nm which is caused by the oxygen dopant. Besides the Mn^{2+} emission we found in Mn-doped $LiBaF_3$ luminescence bands peaking at 423 and 480 nm. These bands correspond to those observed in oxygen-doped $LiBaF_3$ [29] and are tentatively attributed to oxygen impurities which are difficult to avoid in fluoroperovskites.

5.3.1 Photoluminescence

Figure 5.2 (a) shows the PL emission (solid curve) and excitation (dashed and dotted curves) spectra of an oxygen-related complex in Mn-doped $LiBaF_3$. In PL, one band is peaking at 423 nm and a weaker one at 480 nm. The corresponding excitation spectra

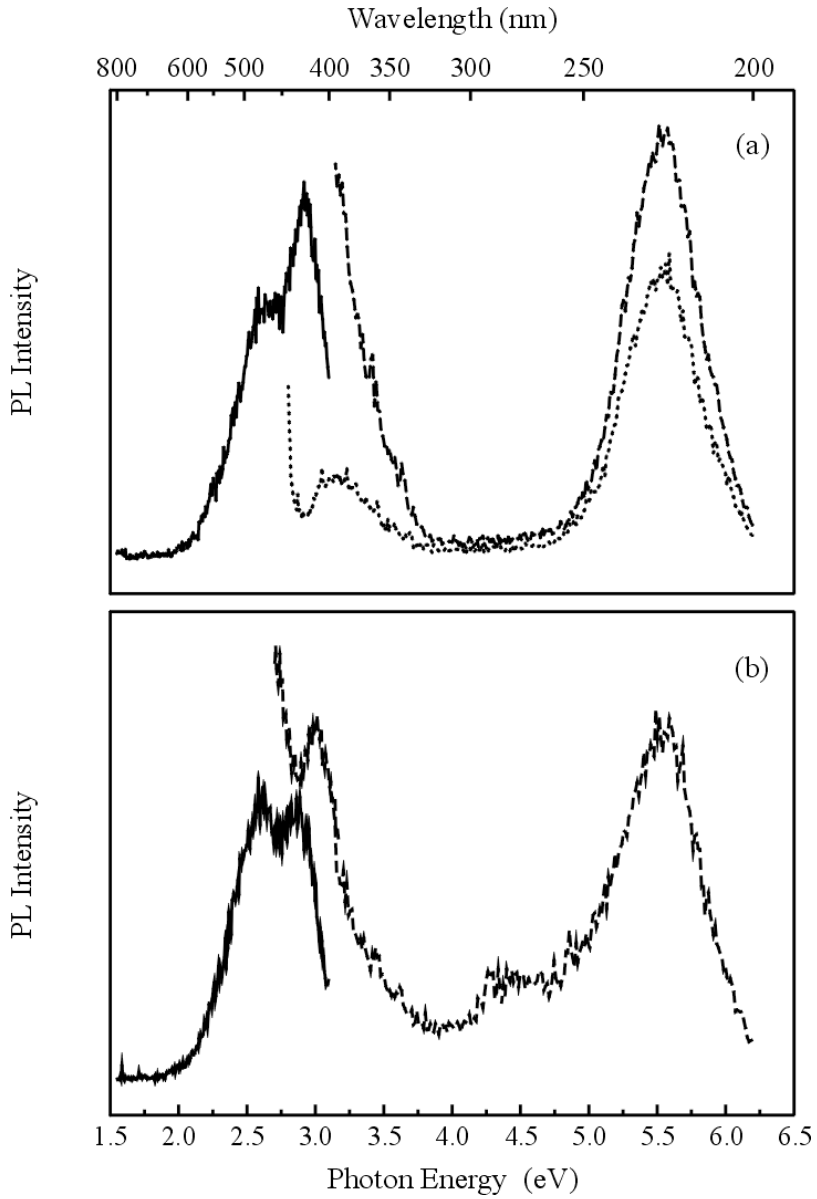

Figure 5.2: (a) PL emission (solid curve) and excitation (dashed and dotted curves) spectra of an oxygen-related complex in 0.2% Mn^{2+}-doped $LiBaF_3$ recorded at RT. The PL was excited at 220 nm. The excitation spectra were detected at 423 nm (dashed) and 480 nm (dotted). The increase in the excitation spectra is caused by incident excitation light. (b) PL emission (solid curve) and excitation (dashed curve) spectra of an oxygen-related complex in $LiBaF_3$:Mn^{2+} recorded at 20 K. The PL was excited at 220 nm; the excitation spectrum was detected at 475 nm. The excitation spectrum detected at 430 nm is not shown; it is identical to the one detected at 475 nm.

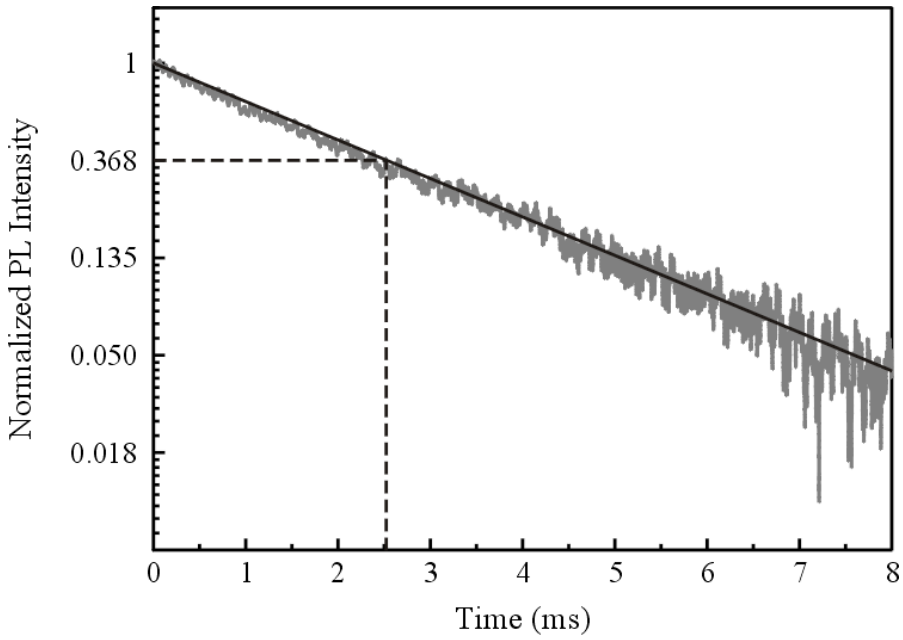

Figure 5.3: PL lifetime of an oxygen related complex in 0.2% Mn^{2+}-doped $LiBaF_3$ at RT excited with a nitrogen flash-lamp and detected at 423 nm.

show intense bands at 220 and 398 nm. The radiative lifetime of the 423 nm luminescence is (2.5±0.3) ms (Figure 5.3). The 423 and 480 nm luminescence bands are not caused by the Mn dopant.

At 20 K the 423 and 480 nm PL bands do not change significantly. Here both luminescence bands have the same intensity and peak at about 430 and 475 nm. Their excitation spectra are identical with their maxima at 220 and 412 nm (Figure 5.2 (b)).

5.3.2 Photoluminescence detected Electron Paramagnetic Resonance

The ground state of an O^{2-} impurity is diamagnetic and can thus not be detected by EPR. However, the excited state of O^{2-} can become paramagnetic if the excited electron and the remaining unpaired electron have parallel spins, i.e. if the excited $(O^{2-})^*$ is in a triplet state.

Figure 5.4 shows a PL-EPR spectrum detected in the oxygen-related luminescence bands found in Mn^{2+}-doped $LiBaF_3$. The spectrum was recorded in the K-band (23.73 GHz) for a magnetic field orientation parallel to [110]. The PL was excited at 1.5 K

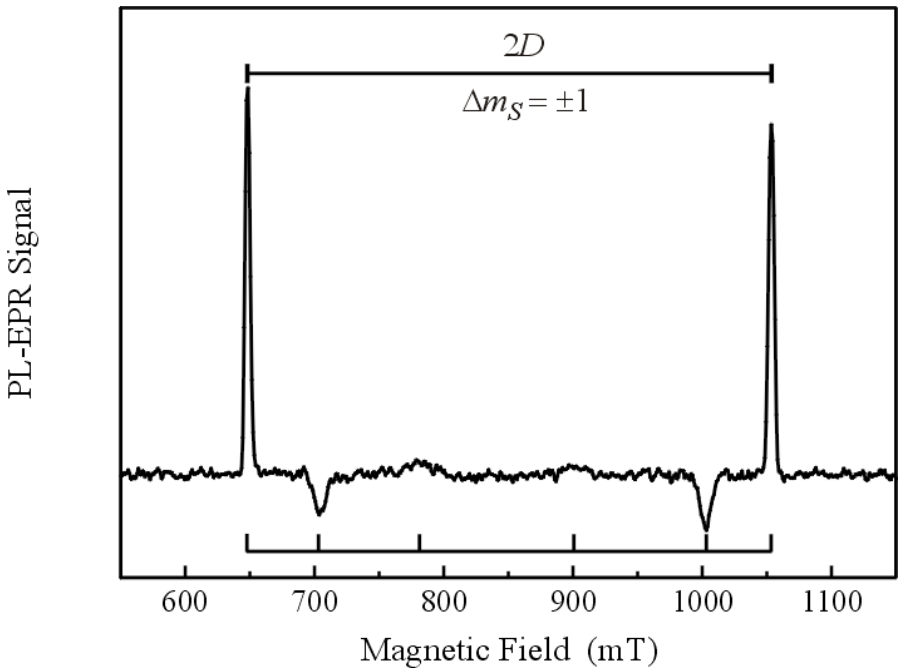

Figure 5.4: PL-EPR spectrum of an oxygen-related complex in $LiBaF_3$:Mn^{2+} for an orientation of the magnetic field parallel to [110]. The spectrum was recorded as microwave-induced changes in the integral PL at 1.5 K applying a microwave frequency of 23.73 GHz. The PL was excited with a deuterium lamp and a subsequent 218 nm interference filter and detected in the integral luminescence with an edge filter (KV 380).

with a deuterium lamp and a subsequent 218 nm interference filter and detected in the integral luminescence with a 380 nm edge filter. The angular dependence of these lines for a rotation of the magnetic field in a {110} plane is presented in Figure 5.5. We used the spin Hamiltonian of a triplet spin ($S = 1$) system with an orthorhombic fine structure (FS) tensor to analyze the angular dependence of the PL-EPR line, i.e.

$$\mathcal{H} = \mu_{\mathrm{B}} \cdot \vec{B} \cdot \underline{\underline{g}} \cdot \vec{S} + \vec{S} \cdot \underline{\underline{D}} \cdot \vec{S} \tag{5.1}$$

where $\underline{\underline{g}}$ and $\underline{\underline{D}}$ are the g and D tensors, μ_{B} is the Bohr magneton, $\vec{B}$ is the magnetic field vector and $\vec{S}$ is the electron spin operator. The orientations of the g and D tensors can be described with a set of Euler angles. In the principal axes system the g tensor is characterized by its three principal values g_{xx}, g_{yy}, and g_{zz}. The D tensor can be expressed with the two FS values D and E in the principal axes system which have the

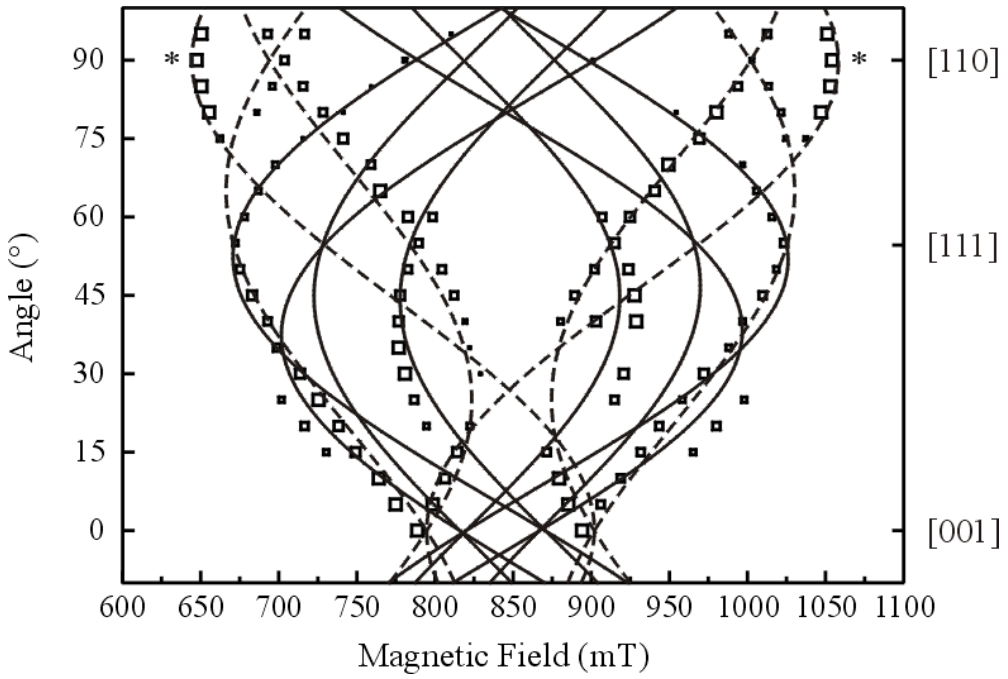

Figure 5.5: Angular dependence of the PL-EPR lines, recorded for a rotation of the magnetic field in a {110} plane. The spectra were recorded as microwave-induced changes in the integral PL at 1.5 K applying a microwave frequency of 23.73 GHz. The PL was excited with a deuterium lamp and a subsequent 218 nm interference filter and detected in the integral luminescence with a 380 nm edge filter. The open squares represent the experimental line position; the dashed and solid (two-fold degenerate) lines are calculated by using the FS parameters of Table 5.3.2. The lines marked with "$*$" consist of two magnetically non-equivalent lines, which cannot be resolved here.

usual meaning as the axial ($D = 3/2 \cdot D_{zz}$) and the non-axial ($E = 1/2 \cdot (D_{xx} - D_{yy})$) parts, respectively (see e.g. [30]). The choice of the z axis corresponds to the maximal absolute value of the FS splitting. The calculated EPR angular dependence for a rotation of the magnetic field in a {110} plane is shown in Figure 5.5 by solid lines. The parameters are listed in Table 5.3.2. All observed resonances are due to "allowed" ($\Delta m_S = \pm 1$) transitions. The principal axes z of the g and the D tensors are assumed to be collinear and parallel to a <110> direction. The x and y axes of the g and D tensors are rotated by an angle of 25° about the z axis and are thus not aligned along any crystal axes.

In principle, a triplet spin system having orthorhombic symmetry with the principle axis, z, along a <110> direction should show six magnetically non-equivalent center

orientations, if the x and y axes of the D tensor are aligned exactly along the crystal axes <100> and <110>. In our case neither the x nor the y axis coincides with a <100> or a <110> direction. Thus, each of the six orientations mentioned above is split in two further magnetically non-equivalent center orientations. The spectrum of each center orientation should be split by the fine structure interaction into two lines symmetrical about $g = 2$. Altogether up to 24 resonance lines could appear in the PL-EPR spectra. The largest splitting of $2D$ is for the magnetic field parallel to a <110> direction. However, for a rotation of the magnetic field in a {110} plane the angular dependence shows only up to 16 resonance lines, 8 of which are two-fold degenerate (see Figure 5.5). The number of lines is reduced to 8 for $B\|$<110> and to 4 for $B\|$<100>. Note, that for $B\|$<110> only 6 lines can be observed in the experimental spectrum (indicated by bars in Figure 5.4). It was not possible to determine the sign of the FS parameter D, experimentally by e.g. magnetic circular polarization of emission (MCPE) measurements.

The highest PL-EPR line intensity was obtained for a photon energy of 2.7 eV (460 nm) which corresponds to the low temperature luminescence spectrum of Figure 5.2 (b) (solid curve). The best excitation energy using a set of interference filters was found to be at approximately 5.7 eV (218 nm) which is in agreement with the excitation spectrum depicted in Figure 5.2 (b) (dashed curve).

g_{xx}	g_{yy}	g_{zz}	$\lvert D/g_e\beta_e\rvert$ (mT)	$\lvert E/g_e\beta_e\rvert$ (mT)	ϑ (°)
1.97	1.98	1.98	207	52	25
±0.01	±0.01	±0.01	±2	±2	±1

Table 5.1: Parameters of the spin Hamiltonian (equation 5.1) for an oxygen-related luminescence center in Mn-doped $LiBaF_3$. The z-axis of the g and D tensor, respectively, is parallel to a <110> direction. The x and y axes are not aligned along the crystal axes. The x axis is tilted in a {110} plane by an angle ϑ with respect to a <100> direction.

5.3.3 Discussion

The analysis of the PL-EPR data shows that the triplet state of the 460 nm luminescence can be described by g and D tensors with the z axes along a <110> direction. The x and y axes are not aligned along the crystal axes. The x axis is tilted in a {110} plane by an angle of 25° with respect to a <100> direction. The g values as well as the spectral position of the 460 nm luminescence are very similar to those found for oxygen-vacancy complexes in other fluoride crystals [31–33]. Thus, we assign our luminescent triplet state to an oxygen impurity center in $LiBaF_3$. O^{2-} usually substitutes for fluorine and has an extra negative charge which is usually compensated by an fluorine vacancy nearby [31–33]. In $LiBaF_3$ the O_F^{2-}-v_F complex is aligned along a <110> direction which is in agreement with the orientation of the principal axis z of the D tensor. However, we still have to find an explanation for the observation that the x and y axes are not aligned along the crystal axes, but tilted in a {110} plane. We assume a perturbation close to the oxygen-vacancy complex, e.g. Mn^{2+} at a Ba^{2+} site (Figure 5.6). In this case no additional charge compensation is necessary. The connecting line between the center of an unrelaxed O_F^{2-}-v_F complex and the Ba^{2+} site nearby makes an angle of 35° with respect to a <100> direction. However, relaxations in the O_F^{2-}-v_F-Mn_{Ba}^{2+} complex might lead to the measured angle of 25°. Note, that the ionic radius of the Mn^{2+} ion (0.80 Å) is much smaller than that of the Ba^{2+} ion (1.34 Å).

In principle, there would be two further alternatives for an oxygen-related complex considering the necessary charge compensation: (i) Mn^{2+} at a Li^+ site or (ii) a Mn ion in its possible charge state of Mn^{3+} at a Ba^{2+} site. The first possibility can be excluded because the O_F^{2-}-Mn_{Li}^{2+} complex would be aligned along a <100> direction. For (ii) the O_F^{2-}-Mn_{Ba}^{3+} complex would be aligned along a <110> direction, but in this case we cannot explain the tilt of the x and y axes of the D tensor with respect to the crystal axes.

5.4 Mn-related Complex

Beside this oxygen vacancy complex having its emission at 420 nm, Mn^{2+} shows its characteristic luminescence at 710 nm. This dopant can be observed in EPR, but in PL-EPR no resonance lines could be observed in this emission band.

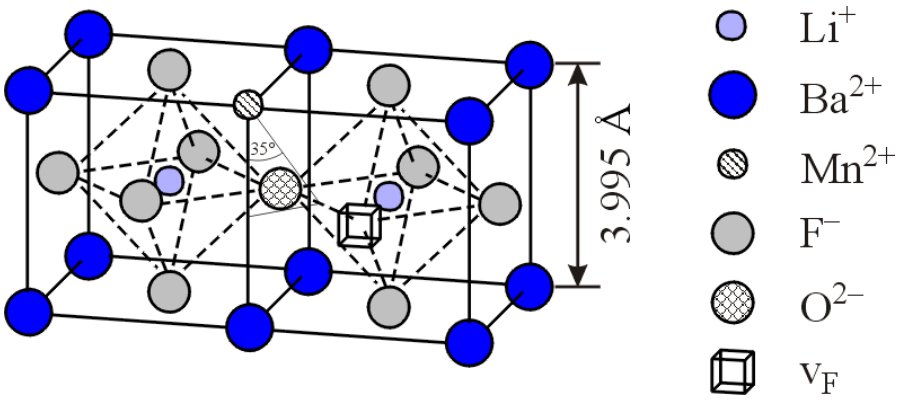

Figure 5.6: Model of the O_F^{2-}-v_F-Mn_{Ba}^{2+} complex in Mn-doped $LiBaF_3$.

5.4.1 Photoluminescence

At RT Mn-doped $LiBaF_3$ shows a broad emission at 710 nm, which can be attributed to the Mn^{2+} dopant, see Figure 5.7 (a). The corresponding excitation spectrum shows several maxima between 300 and 620 nm. These are due to the excited states of Mn^{2+} in an O_h crystal field symmetry as indicated. The excitation bands at 210 and 255 nm are probably caused by an oxygen impurity [29] or higher excited states of Mn^{2+} [17].

While at 20 K the Mn^{2+} emission is still at 710 nm the Mn^{2+} excitation bands are completely superimposed by a broad excitation band at about 510 nm, see Figure 5.7 (b). This band is temperature dependent, i.e. it increases with decreasing temperature, what can be seen in Figure 5.8 (a), where the excitation spectra for the 710 nm band is shown for different temperatures. At about 80 K its intensity starts to increase significantly, see Figure 5.8 (b).

After x-irradiation a broad emission band at 610 nm can be observed at RT; the band at 710 nm remains as a small shoulder of the 610 nm band, see Figure 5.9 (a). The corresponding excitation spectrum shows an intense band at 465 nm and a broad one at about 530 nm.

At 20 K, RT x-irradiated $LiBaF_3$:Mn has two emission bands: One at 610 nm and the second at 720 nm, see Figure 5.9 (b). The excitation spectrum of the 610 nm is comparable to the spectrum recorded at RT. There is an intense band at about 460 nm and a broad one at about 550 nm with the full width at half maximum, however, smaller than at RT. In addition, two new bands in the UV spectral range can be observed at 340

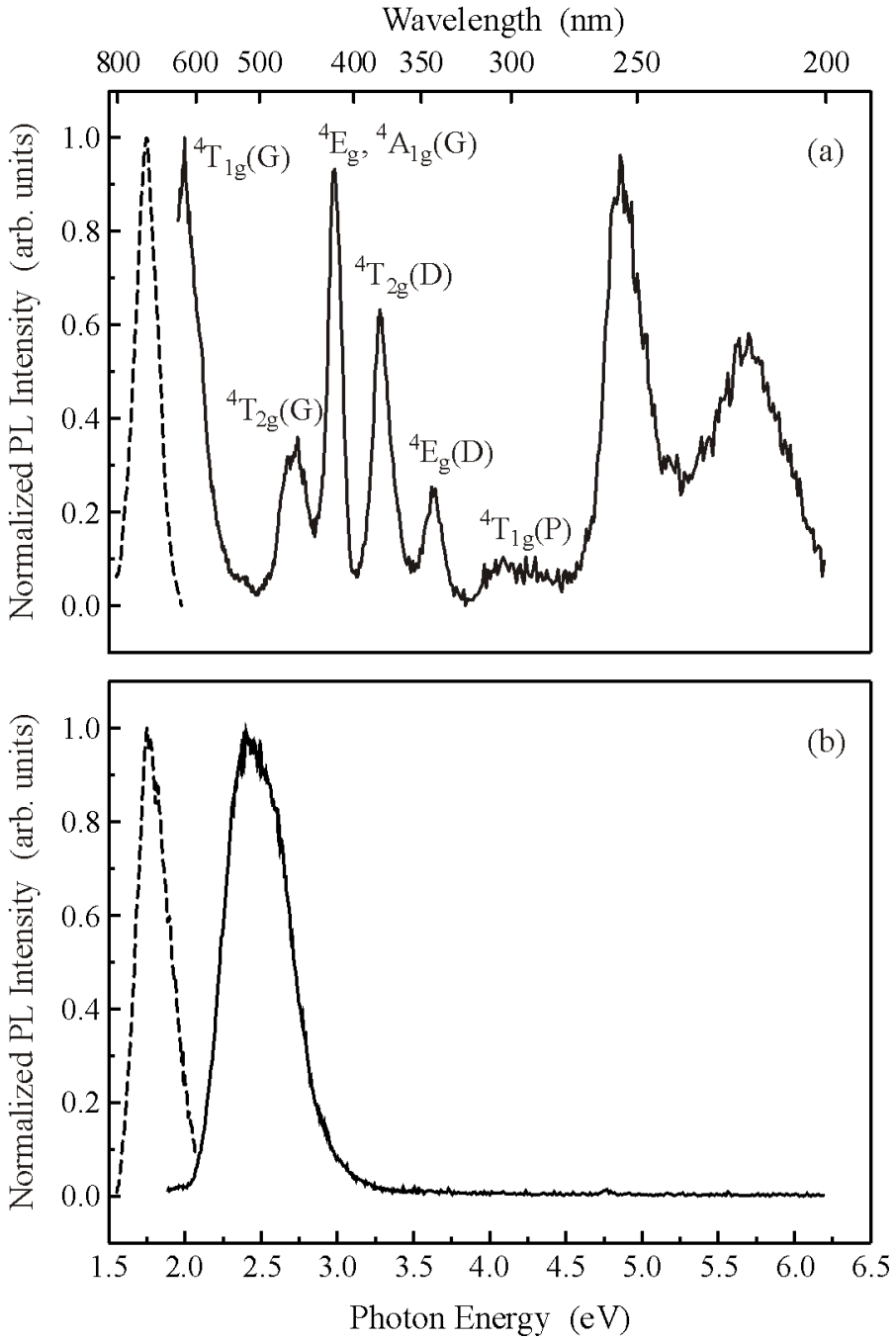

Figure 5.7: PL emission (dashed curves) and excitation (solid curves) spectra of Mn-doped $LiBaF_3$. (a) RT: The PL was excited at 255 nm; the PL excitation spectrum was detected at 710 nm. (b) 20 K: The PL was excited at 510 nm; the PL excitation was detected at 710 nm.

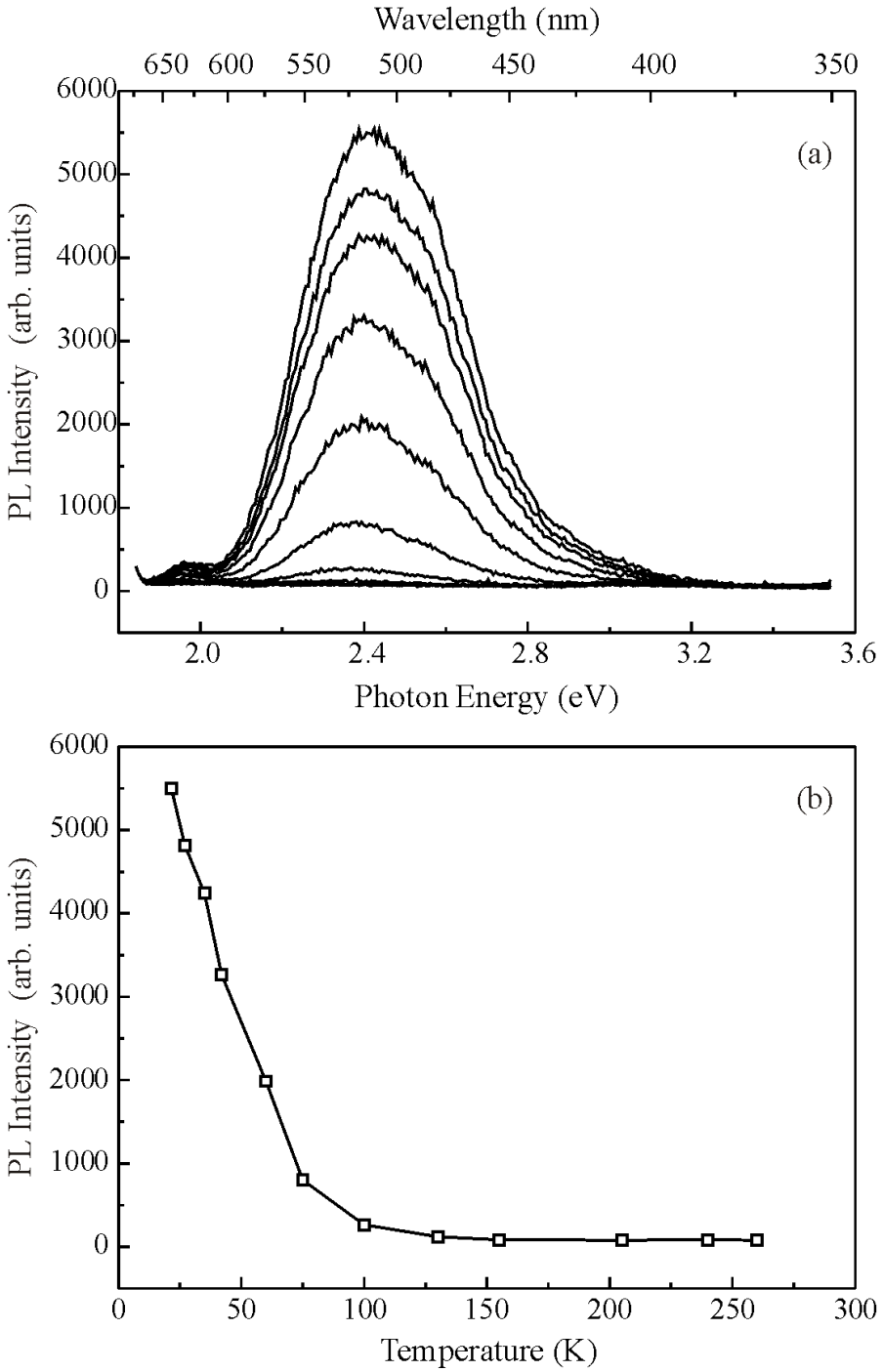

Figure 5.8: (a) Excitation spectra of Mn-doped $LiBaF_3$ detected at 710 nm and different temperatures. The intensity decreases with increasing temperature. (b) shows the PL emission intensity excited at 510 nm versus temperature.

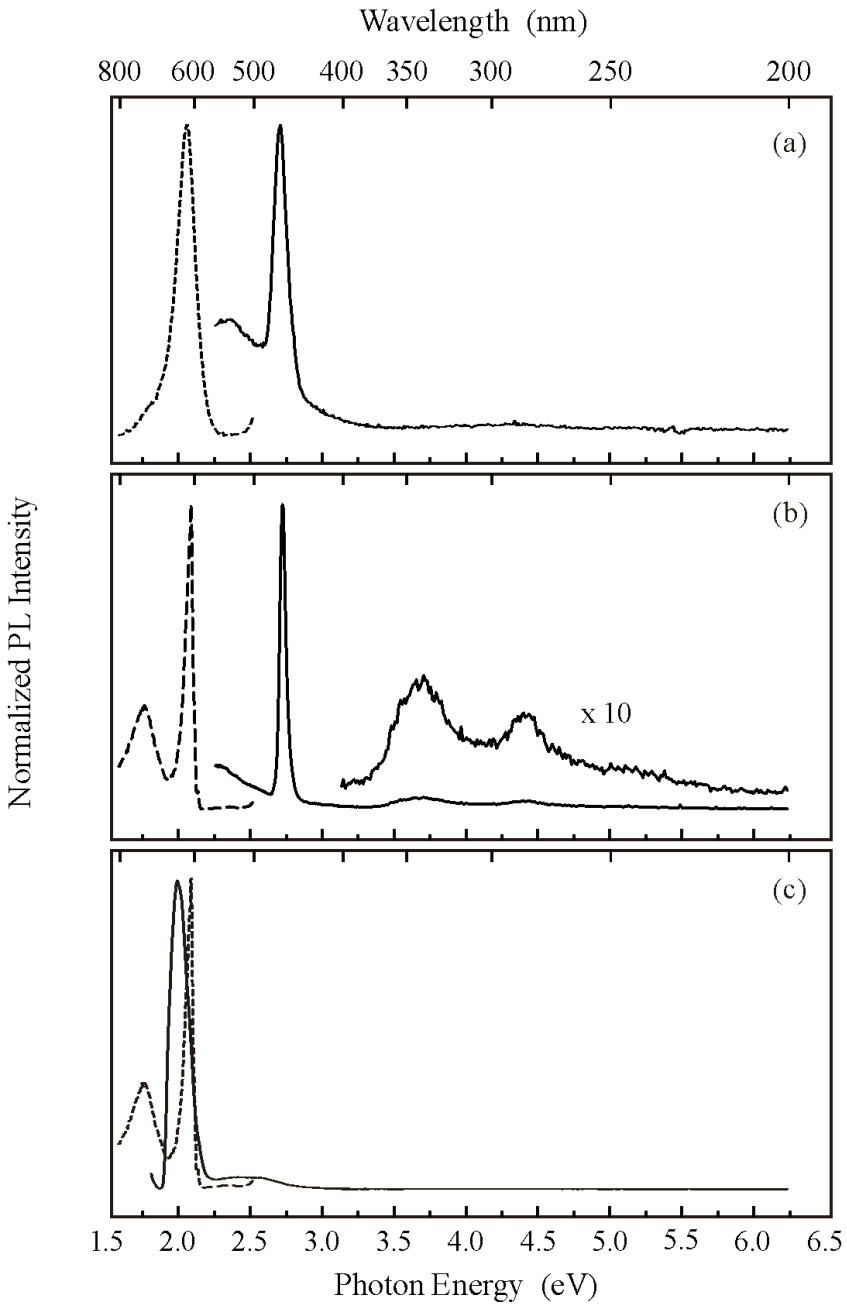

Figure 5.9: PL emission (dashed curves) and excitation (solid curves) of Mn-doped $LiBaF_3$ x-irradiated at RT. (a) RT: The PL emission was excited at 460 nm; the PL excitation spectrum was detected at 610 nm. (b) 20 K: The PL was excited at 460 nm; the PL excitation spectrum was detected at 610 nm. (c) 20 K: The PL emission was excited at 460 nm; the PL excitation spectrum was detected at 710 nm.

and at 280 nm. The excitation spectrum of the 720 nm emission band (spectrum not shown) has an intense excitation peak at 630 nm superimposed on the broad excitation band at about 510 nm which has already been observed in the non-irradiated sample.

5.4.2 Photoluminescence detected Electron Paramagnetic Resonance

Figure 5.10 shows the PL-EPR spectra of Mn-activated $LiBaF_3$, recorded in the 610 nm luminescence band after x-irradiation at RT. The spectra were recorded at a microwave frequency of 23.6 GHz (K-band) for an orientation of the magnetic field parallel to the <110>, the <111>, and the <100> direction, respectively. The PL was excited at 1.5 K with a deuterium lamp and a subsequent DUG 11 band-pass filter and detected in the integral luminescence with a 550 nm edge filter (KV 550).

The angular dependence of the PL-EPR lines indicates that we again deal with a triplet spin state system ($S = 1$). The principal axis, z, of the fine structure tensor is close a <110> direction. But compared to the oxygen vacancy complex the angular dependence is completely different. But an analysis the same spin Hamiltonian as shown in Equation 5.1.

The resonances in the magnetic field ranging from 300 to 1600 mT are due to 'allowed' ($\Delta m_S = \pm 1$) transitions; the resonances at about 200 mT can be attributed to 'forbidden' ($\Delta m_S = \pm 2$) transitions. The forbidden transitions are opposite in sign but comparable in intensity.

For this rotation of the magnetic field in a (110) plane the angular dependence shows up to 12 resonance lines, which are reduced to eight lines for a magnetic field parallel to <110>, indicated by bars is Figure 5.10. For the magnetic field parallel to <111> three lines can be observed and six lines for the magnetic field parallel to the <100> direction, i.e. most of the lines are degenerate (Figure 5.10). The largest splitting of the resonance lines is for a magnetic field parallel to a <110> direction. It was not possible to determine the sign of the FS parameter, D, experimentally by MCPE measurements.

The PL-EPR spectra show, however, additional resonances, e.g. one of it for a magnetic field orientation parallel to a <111> direction (marked with an asterisk in Figure 5.10). These resonances are tentatively assigned to a second Mn-related luminescence center having the same symmetry but different g and FS parameters. A detailed analysis of this center is in progress.

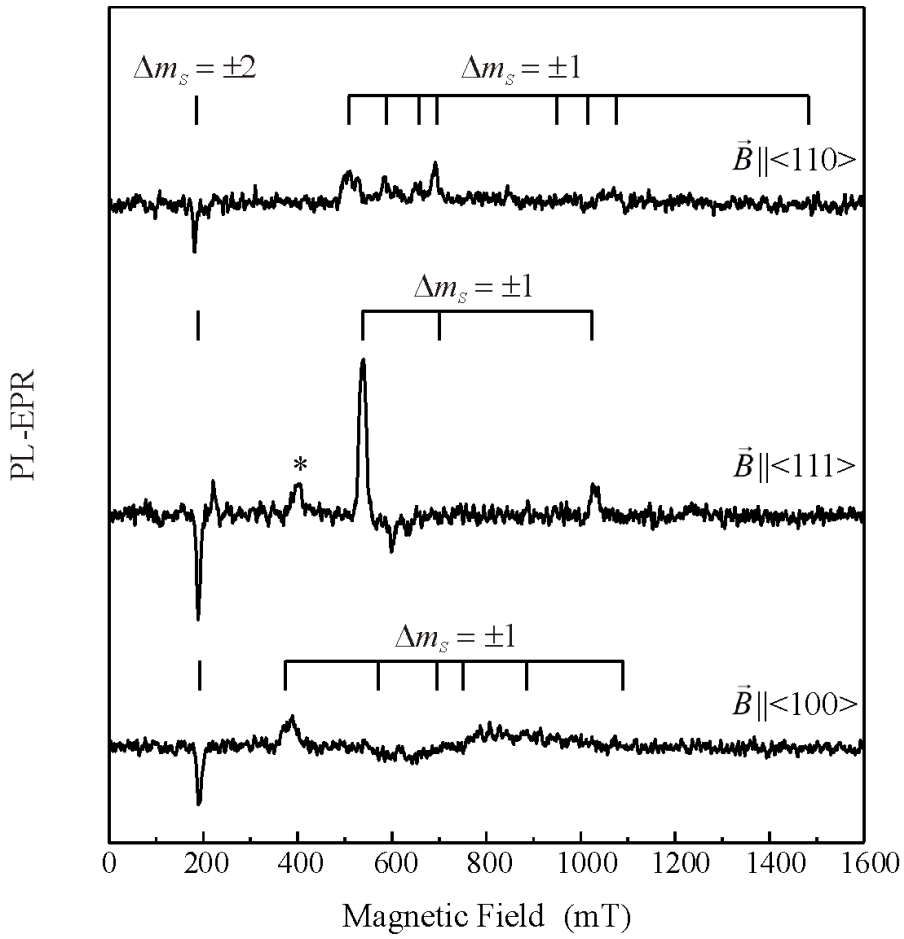

Figure 5.10: PL-EPR spectra of a Mn-related complex in x-irradiated $LiBaF_3$:Mn. The spectra were recorded at 1.5 K and a microwave frequency of 23.97 GHz for different orientations of the magnetic field with respect to the crystal axis system. The PL was excited using a deuterium lamp and a subsequent band-pass filter (DUG 11) and detected in the integral luminescence using an edge filter (KV 550).

The highest PL-EPR line intensity was obtained for a photon energy of about 2 eV (610 nm), which corresponds to the low temperature photoluminescence spectrum (Figure 5.9 (b), dashed curve). The best excitation energy using a band-pass filter was found to be between 3.1 and 5 eV (250 to 400 nm) which is in agreement with the excitation spectrum depicted in Figure 5.9 (b), solid curve. Although a significant higher luminescence intensity could be achieved by exciting into the radiation-induced defect band at about 460 nm, we did not want to have any direct excitation of the Mn^{2+} bands and focused thus on the UV excitation bands.

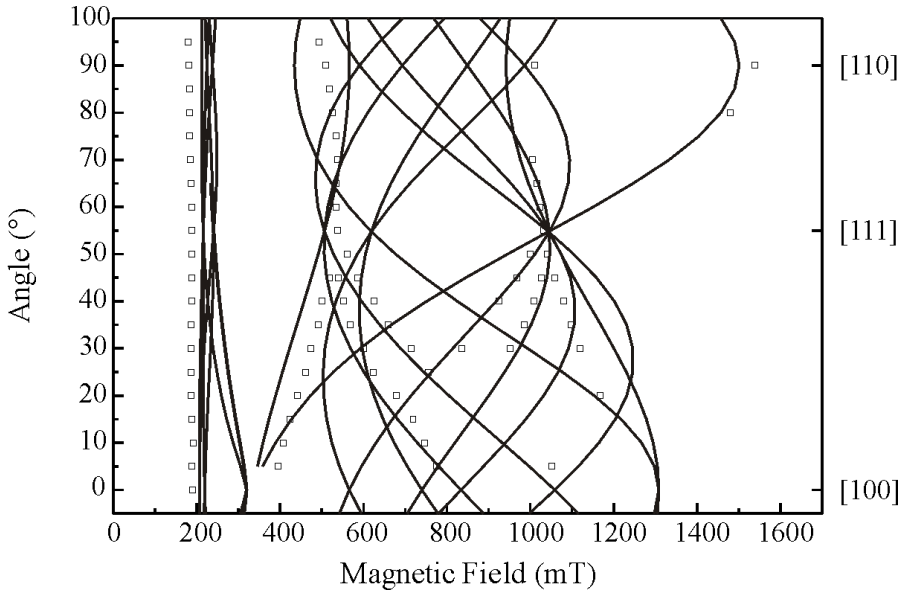

Figure 5.11: Angular dependence of the PL-EPR lines with forbidden transitions, recorded for a rotation of the magnetic field in a {110} plane. The spectra were recorded as microwave-induced changes in the integral PL at 1.5 K applying a microwave frequency of 23.97 GHz. The PL was excited with a deuterium lamp and a subsequent band-pass (DUG 11, 240 nm $< \lambda_{exc.} <$ 400 nm) and detected in the integral luminescence using an edge filter (KV 550, $\lambda_{em.} > 550$ nm). The open squares represent the experimental line position; the solid (two-fold degenerate) lines are calculated by using the FS parameters of Table 5.4.2 (a).

The angular dependence of the PL-EPR lines is shown in Figures 5.11 and 5.12. For the angular dependence with the forbidden transitions the fit is not very good. There are significant deviations from the recorded data points. A fit for the angular dependence without the forbidden transitions is in better agreement with the experimental results. However, both fits show have the same symmetry an comparable g and FS parameters, see Table 5.4.2.

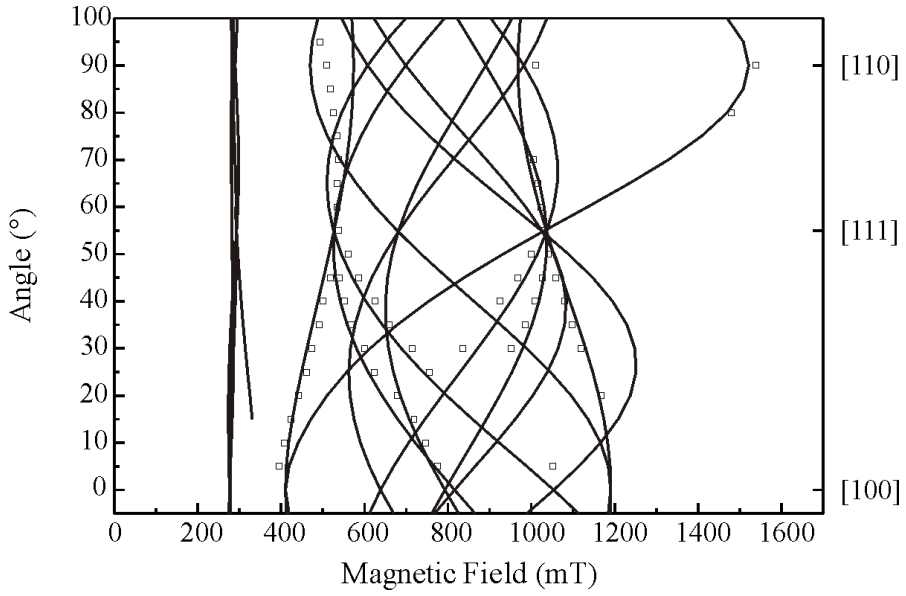

Figure 5.12: Angular dependence of the PL-EPR lines without forbidden transitions, recorded for a rotation of the magnetic field in a {110} plane. The spectra were recorded as microwave-induced changes in the integral PL at 1.5 K applying a microwave frequency of 23.97 GHz. The PL was excited with a deuterium lamp and a subsequent band-pass (DUG 11, 240 nm $< \lambda_{\text{exc.}} <$ 400 nm) and detected in the integral luminescence using an edge filter (KV 550, $\lambda_{\text{em.}} > 550$ nm). The open squares represent the experimental line position; the solid (two-fold degenerate) lines are calculated by using the FS parameters of Table 5.4.2 (b).

5.5 Discussion

The luminescence properties of Mn-activated $LiBaF_3$ are complex: At RT, PL emission and excitation spectra of non-irradiated, Mn-doped $LiBaF_3$ show the typical features of the Mn^{2+} dopant; at low temperature, however, a new broad excitation appears at about 510 nm. After RT x-irradiation, the PL emission spectra show a new emission band at about 610 nm while the PL excitation spectra show radiation induced absorption bands at 460 nm, 530 nm, and in the ultraviolet spectral range. Many different defects, intrinsic or radiation-induced, are involved in the luminescent processes.

In [34] it has already been proposed, that an F-type center is responsible for the radiation-induced 460 nm absorption/excitation band. Based on magnetic circular dichroism of the optical absorption (MCD) and MCD-detected EPR measurements it was assumed that the F-type center interacts with an $S \geq 1$ center.

	g_{xx}	g_{yy}	g_{zz}	$\lvert D/g_e\beta_e\rvert$ (mT)	$\lvert E/g_e\beta_e\rvert$ (mT)
(a)	2.08	1.97	1.97	640	85
	±0.02	±0.02	±0.02	±30	±10
(b)	2.07	2.04	1.88	605	61
	±0.02	±0.02	±0.02	±30	±10

Table 5.2: Parameters of the spin Hamiltonians (Equation 5.1) for the Mn-related center in Mn-activated $LiBaF_3$; (a) considering the forbidden transition, (b) without the forbidden transitions. In both cases the z-axis of the g and the D tensor, respectively, is close to a <110> direction.

The PL-EPR experiments showed that there is at least one radiation-induced, luminescent spin triplet system in Mn-doped $LiBaF_3$ after x-irradiation. This Mn-related triplet system can be described by a FS tensor with its z-axis close to a <110> direction; the slight deviation from the <110> direction has a value of $\theta = 8°$. It might be due to a perturbation in the vicinity of luminescent spin triplet system. This perturbation has not been analyzed yet.

6 The Persistent Phosphors MAl_2O_4 (M = Ca, Sr)

Presently most persistent phosphors are sulfides like ZnS, CdS, CaS, and SrS. More recently the RE doped aluminates MAl_2O_4 (M = Ca, Sr) have been developed to fill this role [3, 5, 35–40] and these are the subject of investigations described in this chapter. Both systems emit a purple/green luminescence originating from the optical activator Eu. Even the single doped systems show phosphorescent behavior. However, the phosphorescent decay time can be significantly increased for $SrAl_2O_4$ (SAO) by Dy co-doping and for $CaAl_2O_4$ (CAO) by Nd co-doping, see Figure 6.1. Despite many years of study the complete mechanism of this persistent phosphorescence is still not understood though several electron and hole trapping mechanisms have been proposed: RE traps are considered to have the dominant role in [35, 36, 39] for the recombination process, but intrinsic electron and hole traps have been put forward as the source of the traps in [5, 38].

The first model for the recombination process was proposed by Matsuzawa et al. [4] and is described as follows: after excitation of the Eu^{2+} ion a hole is being released and then trapped close to the Dy^{3+} or Nd^{3+} dopant, respectively. Upon thermal activation the hole is released from Dy^{4+} to the valence band and recombines at the Eu^{+} ion, which leads to the persistent luminescence. This mechanism was further supported by thermoluminescence measurements and consequently has been widely adopted.

In a recently published paper [41] an alternate mechanism was proposed. A new level scheme for SAO-ED is shown in Figure 6.2. Here it can be seen, that an excited Eu ion promotes an electron to the conduction band, which is subsequently trapped at a Dy ion. Thermally activated release from the Dy^{2+} ion leads to the persistent luminescence. However, in this work low temperature recombination luminescence is primarily investigated and discussed.

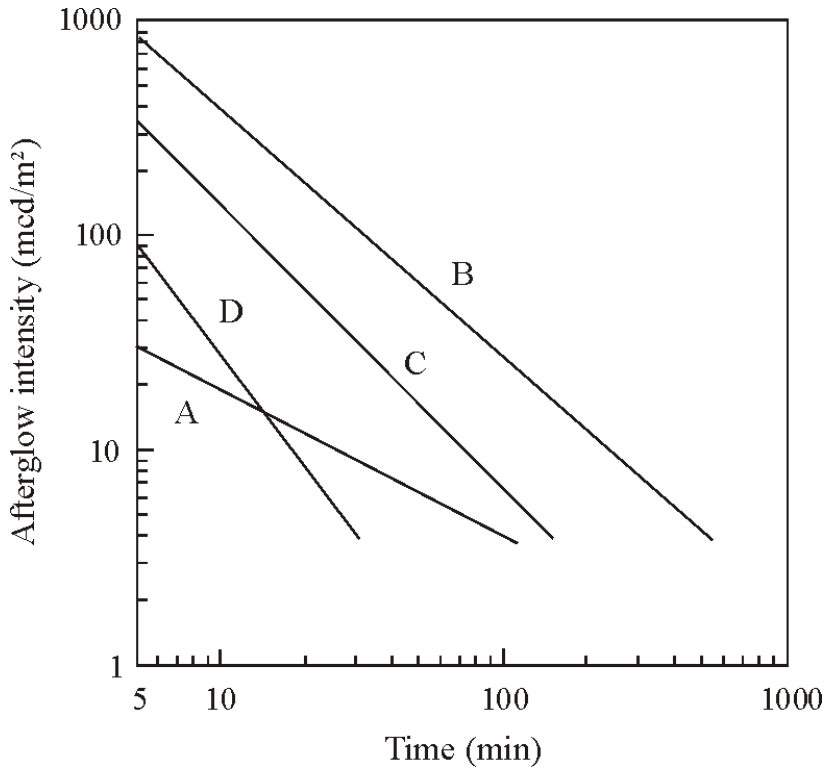

Figure 6.1: Phosphorescence characteristics taken from [4]. The afterglow was measured at RT after 10 min exposure to 200 lx of D_{65} light (standard light). A: $SrAl_2O_4:Eu^{2+}$, B: $SrAl_2O_4:Eu^{2+},Dy^{3+}$, C: $SrAl_2O_4:Eu^{2+},Nd^{3+}$, and D: commercially used ZnS:Cu,Co.

6.1 Sample Preparation

CAO and SAO single crystals were grown at the University of Georgia, using the laser heated pedestal growth (LHPG) method [43]. This method allows the growth of good quality single crystals in fiber form; the crystalline samples used in this study were approximately 100 μm in diameter and 1 cm in length. LHPG samples grow in the same orientation as the seed that is used to grow them; the orientation of the seeds we used was not known hence the fibers used here were of undetermined orientation. For the SAO single crystals a stoichiometric mixture of $SrCO_3$ and Al_2O_3 was used and the growth chamber was filled with a 5% H_2-N_2 mixture. The single crystals were doped with 0.07% Eu (SAO-E) or Dy (SAO-D), and with Eu and Dy (SAO-ED), respectively. For the CAO single crystals a stoichiometric mixture of $CaCO_3$ and Al_2O_3 was used. They were also doped with 0.07% Eu (CAO-E) or Nd (CAO-N), and with Eu and Nd (CAO-EN), respectively.

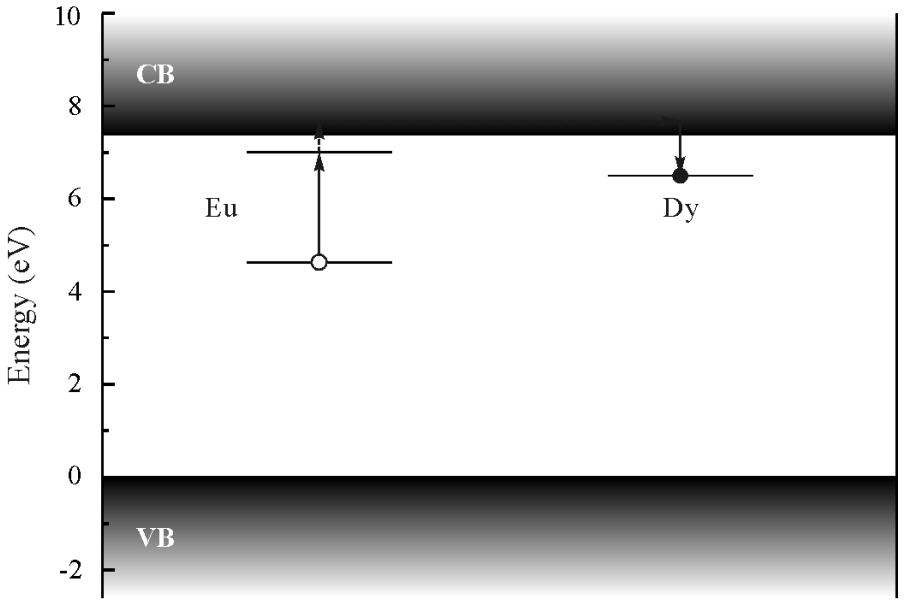

Figure 6.2: Energy level scheme of $SrAl_2O_4$:Eu,Dy [42].

6.2 Photoluminescence and Recombination Luminescence

The PL spectra for CAO and SAO single crystals were recorded at RT and 20 K, respectively. CAO-E shows an intense luminescence peaking at 437 nm at RT and at 20 K an intense luminescence peaking at 437 nm. While the emission band recorded at RT is rather broad (0.36 eV) with a small shoulder at about 465 nm, the one recorded at 20 K is narrower (0.21 eV) (see Figure 6.3). CAO-E co-doped with Nd has identical PL spectra. At RT both samples show a strong RL signal at 437 nm (see Figure 6.4) after excitation at 350 nm. This luminescence band can be allocated to the $5d$-$4f$ transition of a Eu^{2+} ion. The decay time of the co-doped sample is much longer than that of the one doped only with Eu. Compared to the PL spectra the RL spectra of these samples are slightly shifted to higher energies, but show basically the same bands. The shoulder at 465 nm could not be observed in the RL. At 20 K the situation is reversed: The sample only doped with Eu alone has a stronger RL than the co-doped sample. The CAO-EN crystal shows almost no RL signal.

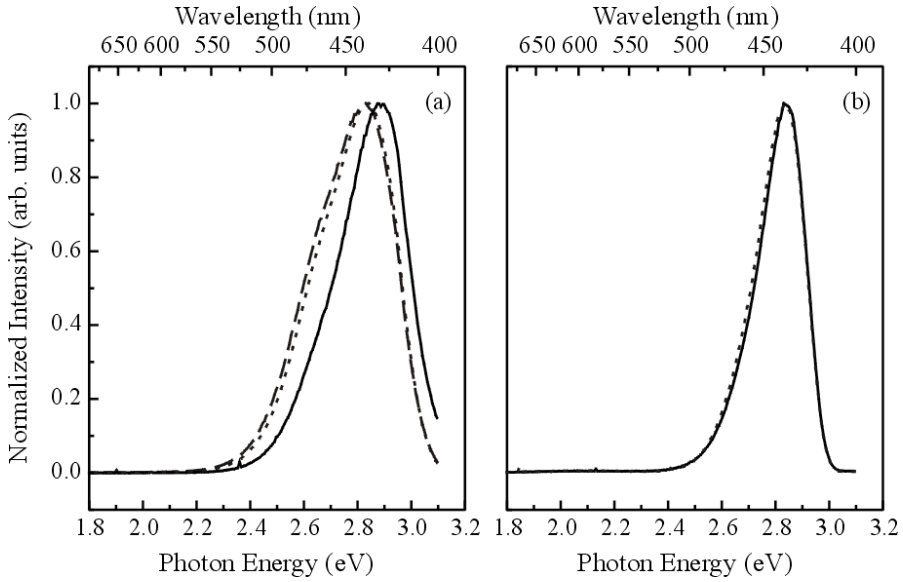

Figure 6.3: (a) Normalized PL spectra of CAO-E (dotted curve), CAO-EN (dashed) excited at 350 nm and normalized RL spectrum of CAO-EN (solid) after excitation at 350 nm, recorded at RT. (b) Normalized PL spectra of CAO-E (dotted) and CAO-EN excited at 350 nm, recorded at 20 K.

Figure 6.5 shows the PL and RL spectra of SAO-E and SAO-ED, recorded at RT and 20 K, respectively. Only one intense emission peaking at 518 nm can be observed at RT. At 20 K a second emission band appears at 442 nm. The 518 nm emission is shifted to 524 nm. The RL spectra recorded at RT show the same peak positions as those seen in the PL spectra. The RL decay of these emissions is comparable to the ones found in CAO. At RT, both SAO-ED and SAO-E show a significant RL with the RL of SAO-ED much more intense and much longer (see Figure 6.6). At 20 K there is almost no RL detectable at 524 nm in SAO-E. But at 442 nm an RL intensity can be observed, which is more intense than the RL of SAO-E at RT.

Nevertheless, it is possible to induce a recombination luminescence at low temperatures by irradiating the samples with the integral light of a deuterium lamp for 30-60 minutes. The RL spectrum of CAO (Figure 6.7 (a), dotted curve) shows luminescence bands at about 310 and 800 nm. Samples additionally doped with Eu, Nd, or Eu and Nd show further bands. CAO-E shows an additional band at 440 nm, CAO-N has an additional band at 880 nm. Figure 6.7 (a), solid curve, shows the RL spectrum for the Eu- and Nd-doped sample. The band at about 440 nm can be attributed to Eu^{2+} [36] whereas the sharp peak at 880 nm can be attributed to Nd^{3+} [44].

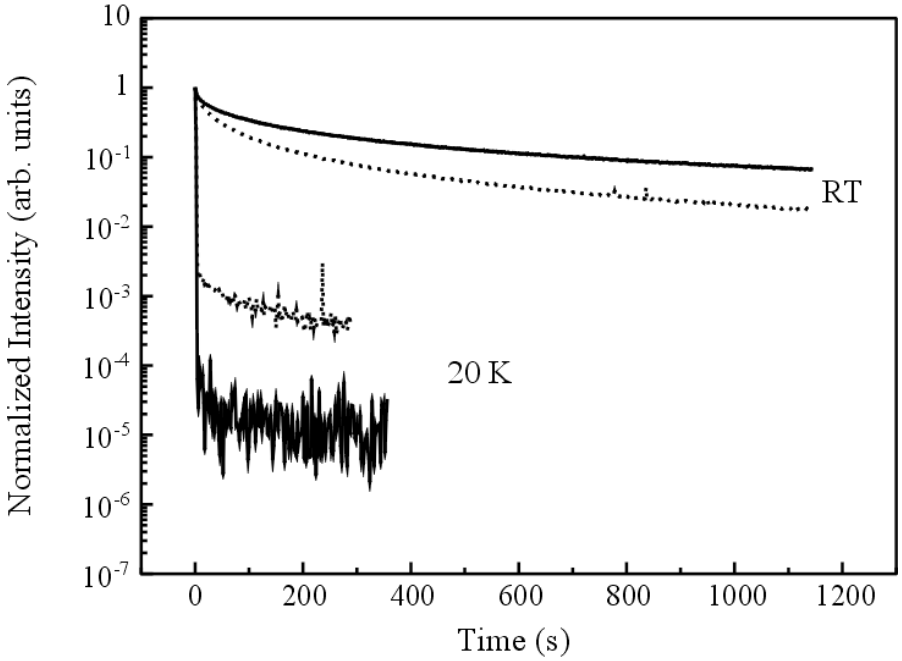

Figure 6.4: Normalized RL decay of CAO-E (dotted curves) and CAO-EN (solid) after switching off the excitation at 350 nm. The decay curves were recorded at 437 nm at RT and 20 K, respectively.

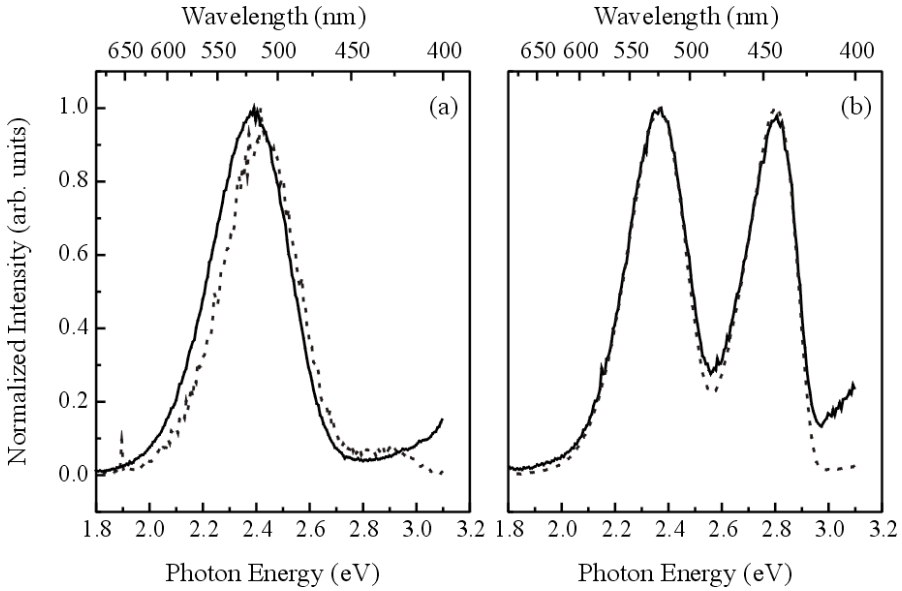

Figure 6.5: (a) Normalized PL (solid line) excited at 350 nm and RL (dotted) spectra of SAO-ED after excitation at 350 nm, recorded at RT. (b) Normalized PL spectra of SAO-E (dotted) and SAO-ED excited at 350 nm, recorded at 20 K.

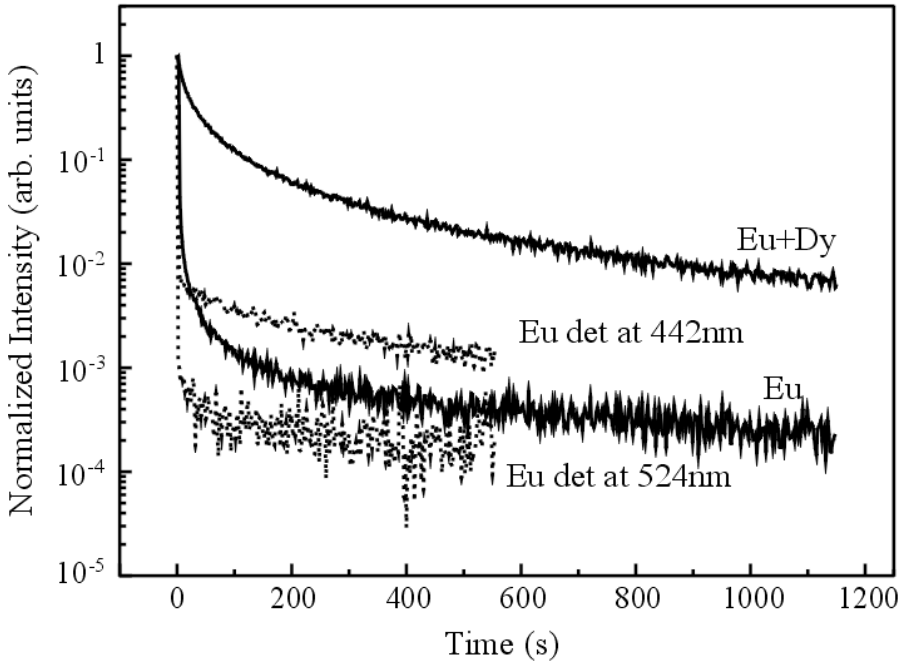

Figure 6.6: Normalized RL decay of SAO-E and SAO-ED after switching off the excitation at 350 nm. The decay curves were recorded at 518 nm at RT (solid lines) and at the wavelengths marked in the figure at 20 K (dotted), respectively. The RL decay of SAO-ED is not shown.

SAO (Figure 6.7 (b), dotted curve) single crystals show a broad luminescence band centered at about 360 nm and another one at 860 nm. The spectrum is similar to that already observed for CAO. Several further bands appear in SAO-D crystals at about 485, 585, 680, and 770 nm. These bands can be attributed to Dy^{3+} [45]. In SAO-E an additional double-structured band peaking at 435 and 520 nm is found. These bands are due to Eu^{2+} [35]. The RL spectrum of SAO-ED (Figure 6.7 (b), solid curve) show bands caused by Eu^{2+} and by Dy^{3+}.

RL excitation spectra were recorded at 4.2 K using the magneto-optical spectrometer. RL was excited with a deuterium lamp and a subsequent set of interference filters; the luminescence was detected integrally. Figure 6.8 shows the spectra for differently doped SAO. For SAO and SAO-D the best excitation wavelength is found to be at 200 nm, whereas for SAO-E and SAO-ED, i.e. additional Eu-doping, it is shifted to about 250 nm. A similar behavior was observed for CAO single crystals (spectra not shown).

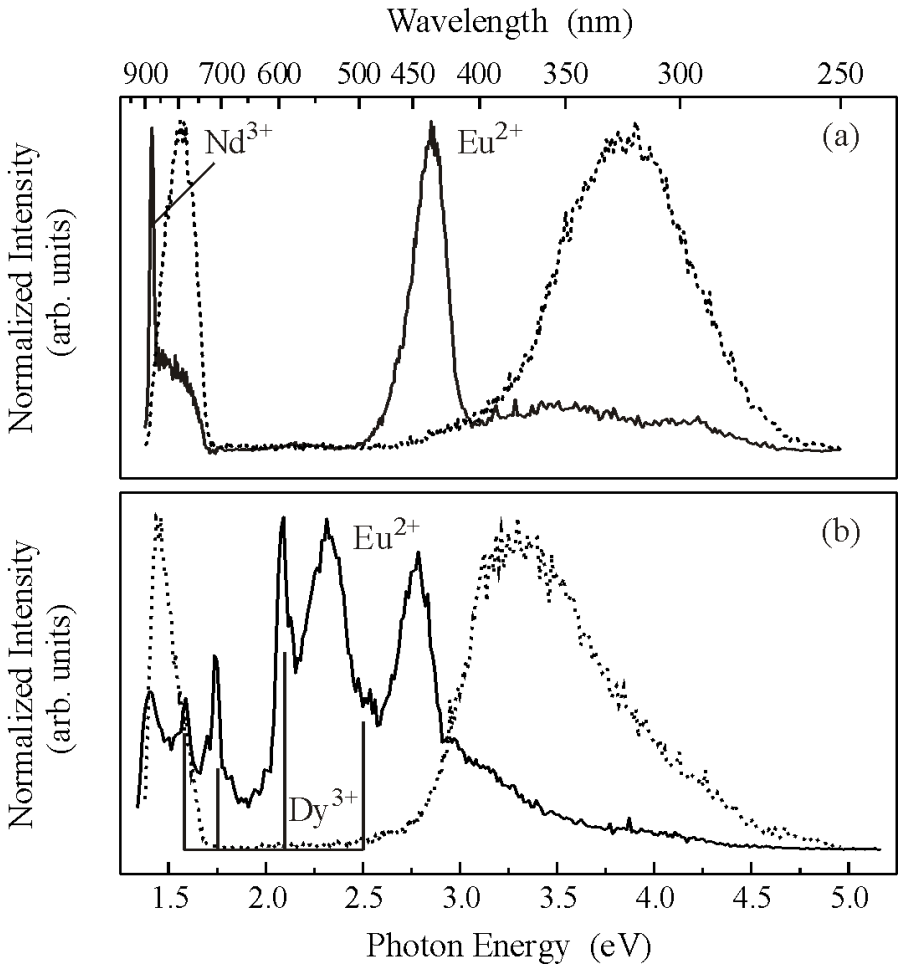

Figure 6.7: RL spectra of (a) CAO (dotted curve) and CAO-EN (solid curve), (b) SAO (dotted curve) and SAO-ED (solid curve), recorded at 20 K after 30 min UV-excitation at 20 K.

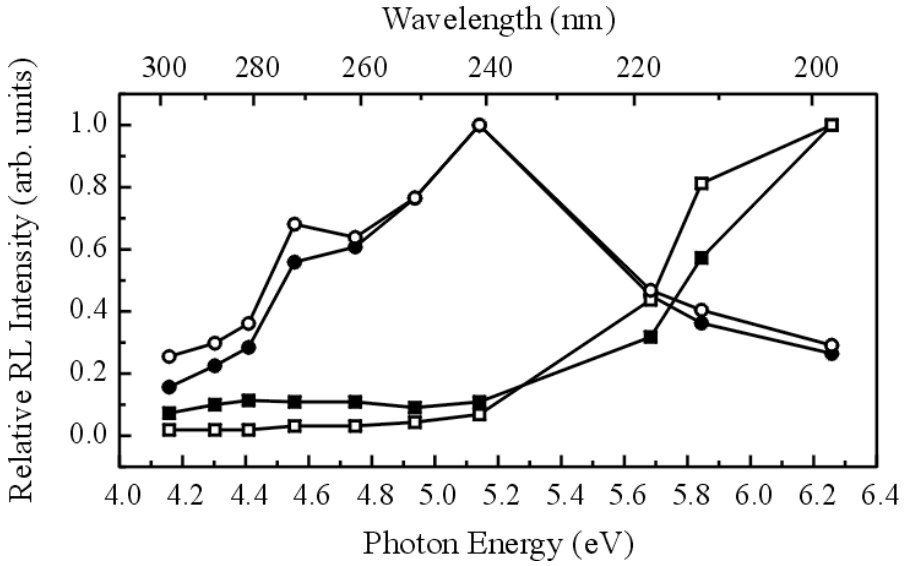

Figure 6.8: RL excitation spectra, recorded at 4.2 K for SAO (full squares), SAO-E (full circles), SAO-D (open squares), and SAO-ED (open circles) single crystals. The RL was excited with a deuterium lamp and a subsequent interference filter at the wavelengths indicated; the luminescence was detected integrally. The symbols represent the experimental data points; the lines connecting the data points are a guide to the eye.

6.3 Electron Paramagnetic Resonance

Nakamura et al. [46] performed EPR experiments on CAO-ED and SAO-EN powders in high frequency (180 GHz) spectrometers. They found three sites for the Eu^{2+}-dopant in SAO and only one site in CAO. The parameters are shown in Table 6.1. Angular dependent EPR spectra of single crystalline SAO-E and CAO-E taken in a conventional EPR X-band spectrometer are shown in Figures 6.9 and 6.10. Both crystals show several

Phosphor	g-value	D(10^{-4} cm^{-1})	E(10^{-4} cm^{-1})	Rel. intensity
$SrAl_2O_4$:Eu,Dy	1.989	1402.17	361.76	1.0
		1123.59	343.82	1.0
		1021.45	250.26	0.25
$CaAl_2O_4$:Eu,Nd	1.988	1791.00	46.33	1.0

Table 6.1: Parameters used for the calculation of high frequency EPR spectra of $SrAl_2O_4$:Eu,Dy and $CaAl_2O_4$:Eu,Nd at 145 K [46].

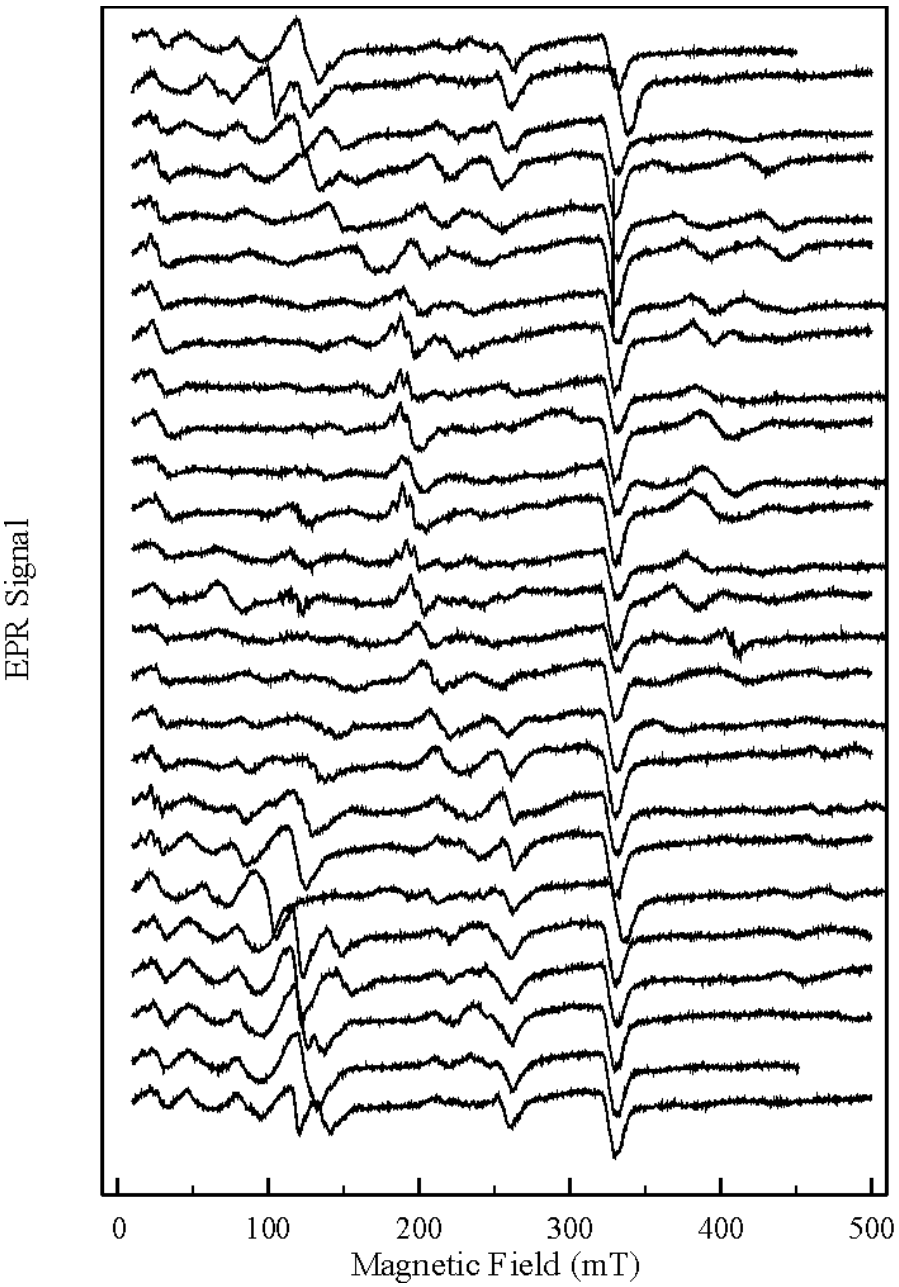

Figure 6.9: Angular dependent EPR-spectra of CAO-E recorded at 10 K in X-band (9.35 GHz). The rotation was performed in an arbitrary plane.

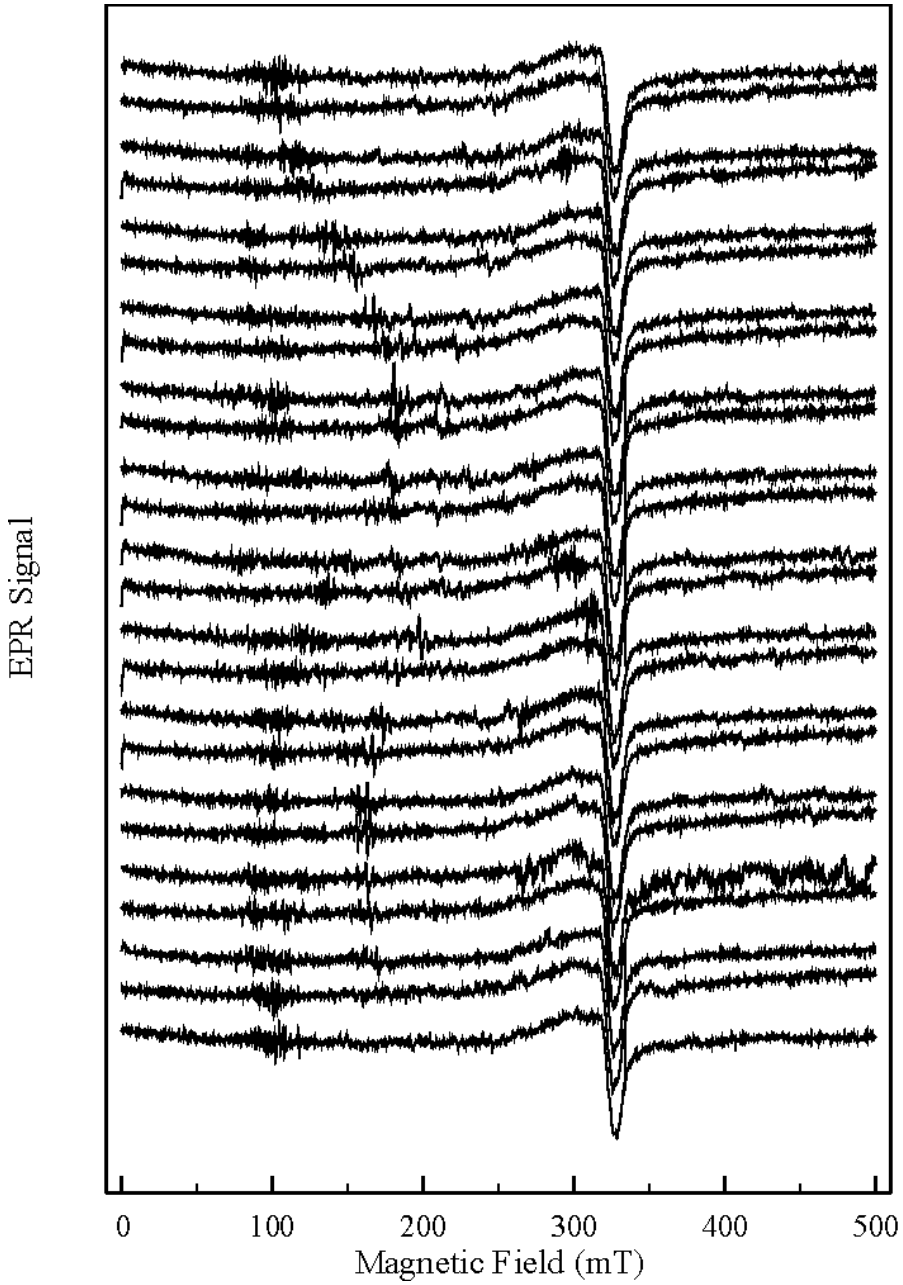

Figure 6.10: Angular dependent EPR-spectra of SAO-E recorded at 10 K in X-band (9.35 GHz). The rotation was performed in an arbitrary plane.

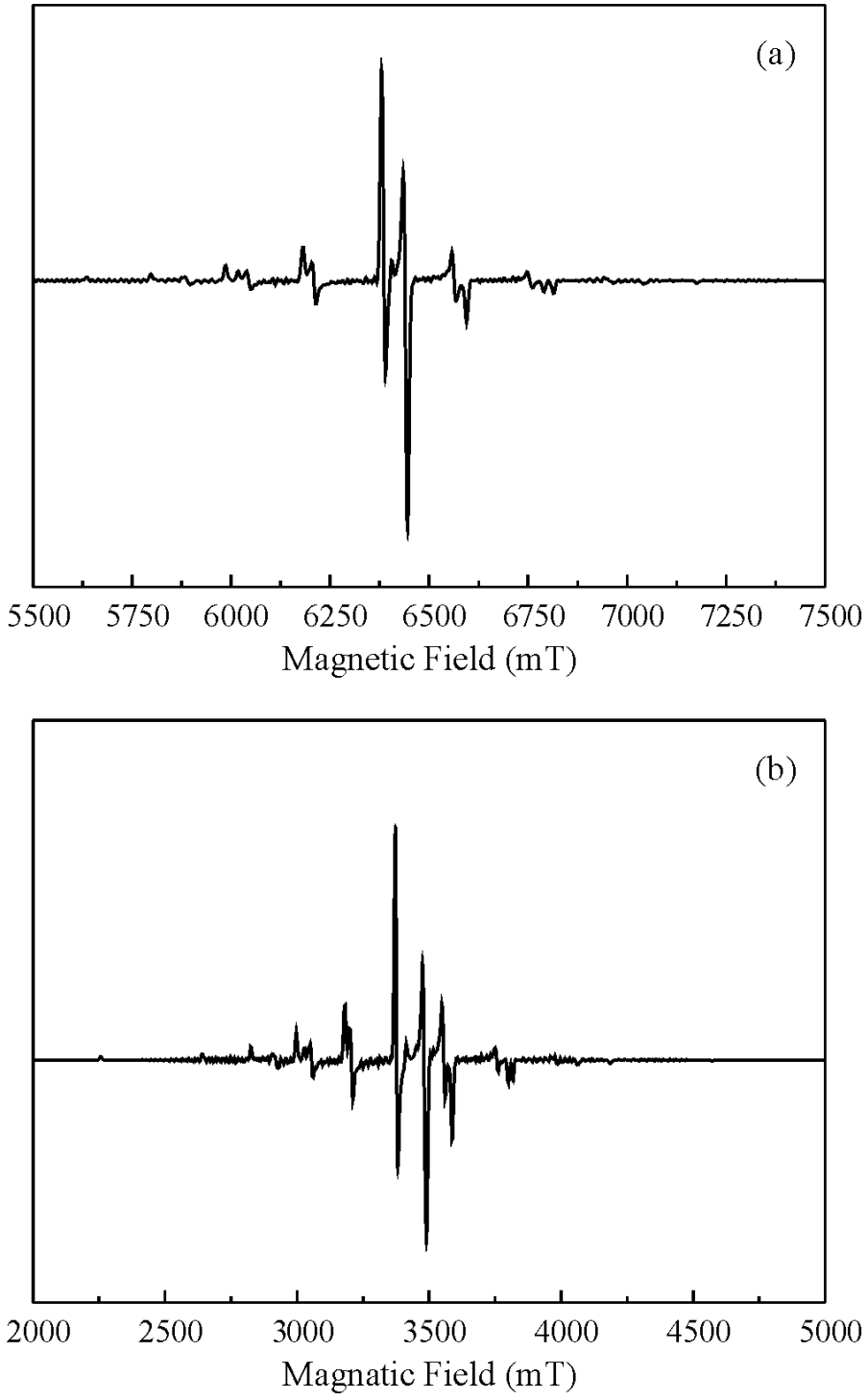

Figure 6.11: Calculated EPR powder spectra of CAO-EN for a microwave frequency of (a) 180 GHz and (b) 93 GHz. The parameters can be found in Table 6.1.

angular dependent lines which cannot yet be assigned. Phosphors doped only with Nd or Dy or co-doped with Nd or Dy show no EPR signal. For improved resolution it is essential to use high frequency EPR. Therefore, the RL-EPR measurements which are described in the following section were not performed in K-band (24 GHz) but in W-Band (93 GHz). A calculation of powder EPR spectra of CAO-EN at 93 GHz and at 180 GHz are shown in Figure 6.11.

6.4 Recombination Luminescence detected Electron Paramagnetic Resonance

The RL-EPR spectra of SAO, SAO-D, SAO-E, and SAO-ED (Figure 6.12 lower part) show a group of lines centered at about 3310 mT ($g = 2.02$) as well as a structureless resonance line at about 3390 mT ($g = 1.97$ for a microwave frequency of 93.7 GHz). Note, that the high-field side of the 3365 mT line is affected by long spin-lattice relaxation times. The resonance at 3390 mT shows no angular dependence, whereas the line group at 3310 mT shows significant changes in structure as a function of orientation with respect to the magnetic field (see Figure 6.14).

The RL-EPR spectra for CAO, CAO-E, and CAO-EN show similar resonances (Figure 6.12 upper graphs). The RL of the CAO-N sample was too weak for RL-EPR measurements. The group of lines at about 3310 mT is comparable to those observed in SAO and is angular dependent (Figure 6.13). The structureless (isotropic) line is shifted to 3365 mT ($g = 1.99$).

Spectral dependencies of the RL-EPR spectra are shown in Figure 6.15 for SAO and CAO. The isotropic line shows no spectral dependence, but the low field group shows significant changes for SAO as well as for CAO.

6.5 Discussion

CAO-E and CAO-EN shows an emission band at 437 nm, which is attributed to a $5d-4f$ transition of a Eu^{2+} ion. A similar luminescence can be observed for SAO-E and SAO-ED. At RT a single peak can be observed at 518 nm, which shifts at 20 K to 524 nm. It is also due to the Eu^{2+} dopant, which substitutes for a Sr^{2+} ion. The additional band appearing at 20 K cannot be attributed to this Eu ion. It is proposed to be due to interstitial Eu^{2+} ions [36].

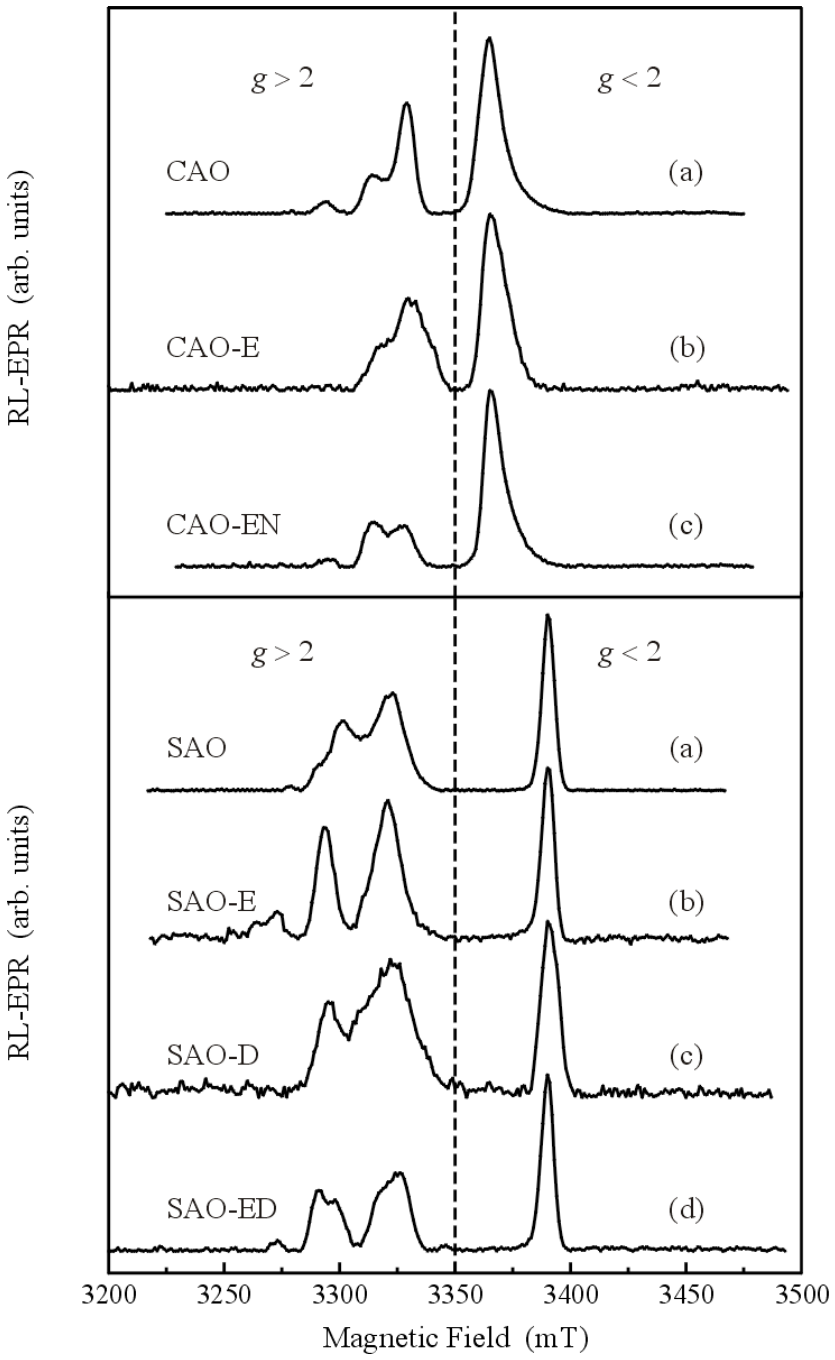

Figure 6.12: The upper graphs show the RL-EPR spectra of (a) CAO, (b) CAO-E, and (c) CAO-EN. The RL-EPR of CAO-N was too weak to be measured. In the lower graphs the RL-EPR spectra of (a) SAO, (b) SAO-E, (c) SAO-D, and (d) SAO-ED are depicted. The RL-EPR was detected in the integral RL at 1.5 K in the W-band (93.7 GHz) after UV-excitation with the light of a deuterium lamp at 4.2 K. The magnetic field dependent background is subtracted.

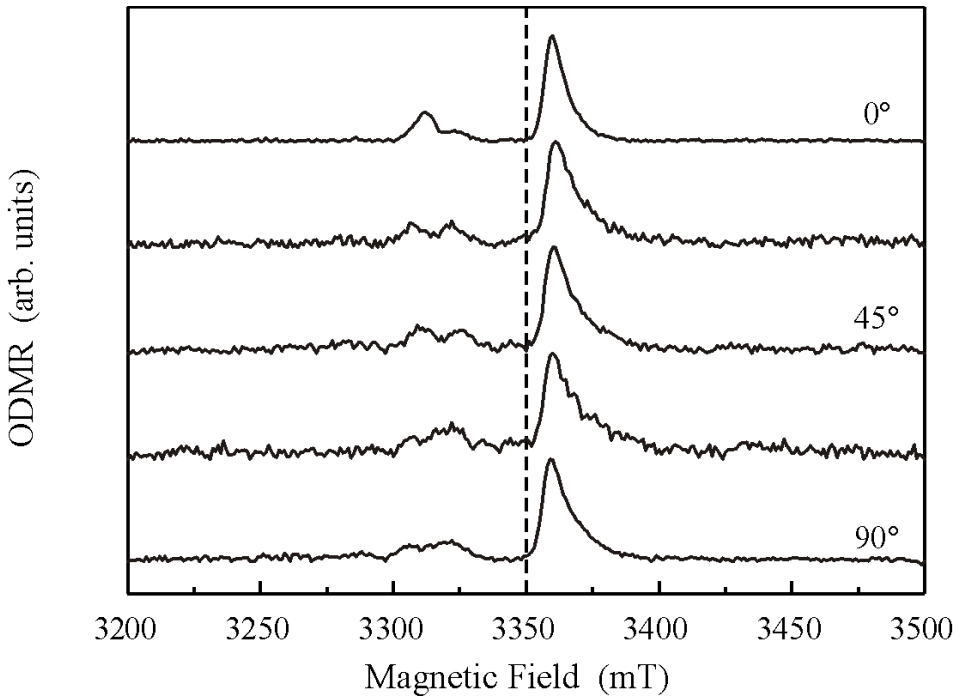

Figure 6.13: Angular dependent RL-EPR spectra of CAO-EN. The RL-EPR was recorded in the integral RL at 1.5 K in W-band (93 GHz) after UV-excitation with the light of a deuterium lamp at 4.2 K. The magnetic field dependent background is subtracted; the rotation of the magnetic field is performed in an arbitrary plane.

The RL which was induced by prior UV-exposure at 4.2 K quenches in high magnetic fields, but it can be increased significantly by applying microwave radiation (93.7 GHz) yielding resonance lines for appropriate magnetic fields. We attribute the RL to a recombination of distant donors and acceptors which were generated by the UV-excitation.

The RL spectra show that either the donor-acceptor recombination energy is emitted directly (undoped samples) or transferred to the rare-earth activators (doped samples). We do observe luminescence from intrinsic centers as well as from RE dopant ions. Europium doping leads to a perturbation of the intrinsic defect states; the maxima of the corresponding RL excitation spectra are shifted to longer wavelengths (Figure 6.8).

The g values of the RL-EPR line at 1.97 (SAO) and 1.99 (CAO), respectively, are less than two, so we can attribute them to donors [47]. The line groups centered at 2.02 are assigned to acceptors [47]. The angular dependence of the donor in CAO and SAO shows that we are dealing with an isotropic center here, whereas the line group of the

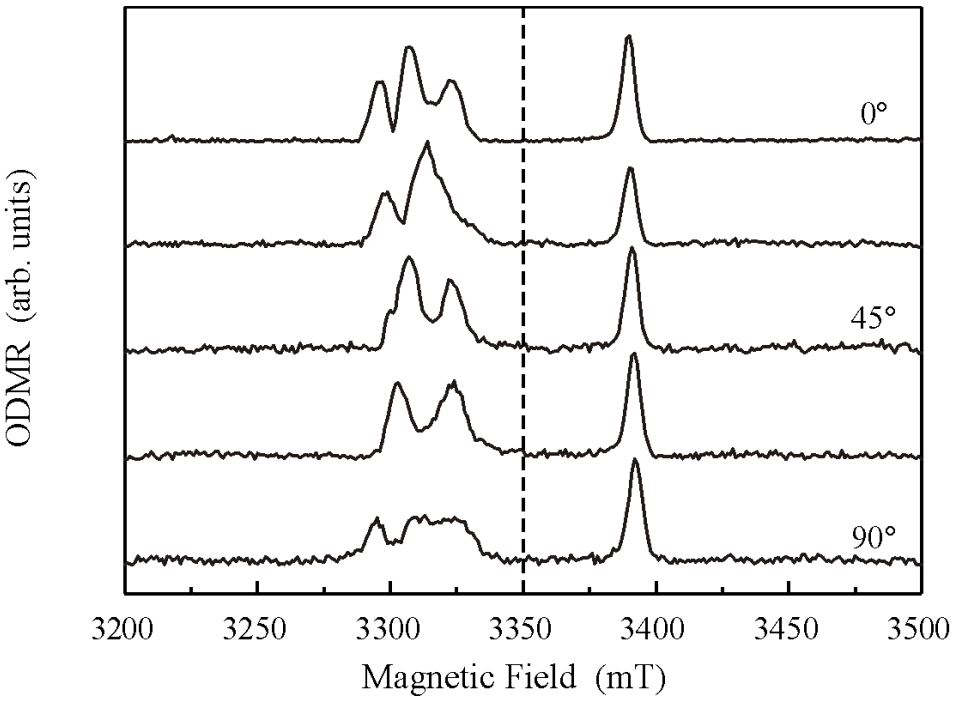

Figure 6.14: Angular dependent RL-EPR spectra of SAO-E. The RL-EPR was recorded in the integral RL at 1.5 K in W-band (93 GHz) after UV-excitation with the light of a deuterium lamp at 4.2 K. The magnetic field dependent background is subtracted; the rotation of the magnetic field is performed in an arbitrary plane.

acceptor is clearly angular dependent. Since the g values of the donors do not change upon doping, these traps are intrinsic. The angular dependence of the line group at 2.02 is caused by different center orientations and by a superimposition of resonances lines of at least two acceptors. We cannot say how the co-doping of Nd or Dy affects the defect structure of the acceptor since the different patterns of the line group at 2.02 (see Figures 6.12 and 6.15) are also affected by the different orientation of the magnetic field. Note that all RL-EPR measurements were performed in an arbitrary orientation of the magnetic field.

From the RL spectra and the spectral dependent RL-EPR we assume that there are two different types of intrinsic luminescences in both aluminates. Because the lines at 1.97 and 1.99, respectively, do not change in the spectral dependent RL-EPR it seems that in both RL processes the same donors are involved. The difference between them is the type of acceptors. In doped aluminates parts of the recombination energy is

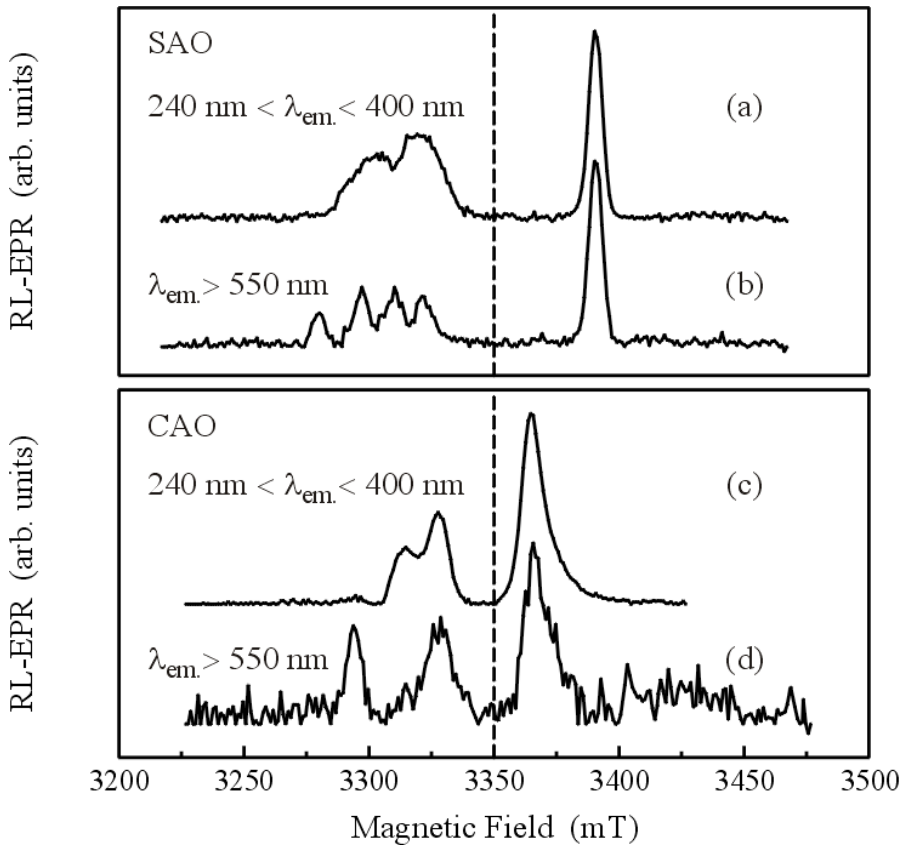

Figure 6.15: Spectral dependent RL-EPR spectra of SAO and CAO. (a) SAO, recorded with UV band-pass filter DUG 11; (b) SAO, recorded with an edge filter KV 550 for the same orientation of the magnetic field as in (a); (c) CAO, recorded with UV band-pass filter DUG 11; (d) CAO, recorded with an edge filter KV 550 for the same orientation of the magnetic field as in (c). The RL-EPR was recorded in the integral RL at 1.5 K in the W-band (93.7 GHz) after UV-excitation with the light of a deuterium lamp at 4.2 K. The magnetic field dependent background was subtracted.

transferred to the dopant. Spectral dependent RL-EPR in doped aluminates (not shown here) showed a comparable behavior to the undoped samples. This indicates that parts of the intrinsic recombination energy is transferred to the dopant. This is also corroborated by the RL spectra.

7 Conclusion

The PL emission of Mn-doped $RbCdF_3$ at 560 nm could be attributed to the Mn^{2+} dopant, having the corresponding excitation peaks in the UV and VIS spectral region. This emission band can be increased significantly upon x-irradiation, where an additional excitation peak at about 300 nm appears; this excitation band can be bleached optically. The EPR measurements showed that the number of Mn^{2+} ions is reduced by x-irradiation and can be restored by optical bleaching. This agrees with the model that optically stimulable Mn^{3+}-F complexes are formed by x-irradiation.

Unfortunately $RbCdF_3$ shows after x-irradiation no PL-EPR resonance lines. In principle it would be possible to analyze the vicinity of the Mn-dopant with EXFAS measurements, but here all Mn ions in the compound are detected not only the optically active ones. An optical detection of EXFAS would lead to a selective detection of the Mn ions; i.e. only the optically active ions will be monitored. This technique is usually called x-ray excited optical luminescence detected x-ray finestructure absorption spectroscopy (XEOL-XAFS).

The investigations on Mn-activated $LiBaF_3$ yielded that there are several luminescent processes. On the one hand non-irradiated $LiBaF_3$ shows a typical Mn^{2+} luminescence and its typical excitation bands in the UV and in the VIS spectral region. On the other hand there is a further luminescence band in the blue region. It turned out to be due to a perturbed oxygen vacancy complex. An oxygen impurity substitutes for a fluorine ion with a F^- vacancy in a <110> direction. This complex is probably perturbed by a Mn^{2+} ion on a Ba^{2+} site lying about 35° away from the complex. After x-irradiation the whole luminescence is covered by a new emission band peaking at 600 nm also showing PL-EPR resonance lines. From the angular dependence it can be extracted that this defect is almost parallel to a <110> direction and it is significantly different from the oxygen vacancy complex.
There are several mechanisms in $LiBaF_3$, which are not understood yet. The new excitation band appearing at low temperatures has not been investigated in detail yet.

This band is probably due to a Mn-vacancy complex, which is already created during the growth process. Quenching of a sample slightly below the melting temperature of $LiBaF_3$ should lead to a destruction of this center and the new excitation band should also disappear. A complete analysis of the PL-EPR spectra recorded after x-irradiation would yield new information on the defect structure responsible for the luminescence at 600 nm.

The persistent phosphors CAO and SAO show a very strong persistent luminescence in the visible region originating from a $5d - 4f$ transition of the Eu^{2+} activator. They can be excited in the near UV region. In this work it could be shown that there is also an RL from CAO and SAO at low temperatures. This luminescence was attributed to a distant donor acceptor recombination, which were created by UV excitation at low temperatures. The energy of the recombination process is either transferred to the rare earth activators (doped samples) or emitted directly (undoped samples). There is RL coming from intrinsic centers as well as from rare-earth the dopant ions. It was shown that there is only one type of donors, which could be attributed to intrinsic traps, whereas there are at least two acceptors. Europium doping leads to a perturbation of the intrinsic defect states, i.e. the excitation spectra are shifted to higher wavelengths.

A $BaCl_2$ EXAFS

The stable phase of $BaCl_2$ is the orthorhombic $PbCl_2$ structure, space group $Pnma(D_{2h}^{16})$ with lattice parameters $a = 7.865$ Å, $b = 4.731$ Å, and $b = 9.421$ Å [48]. The crystal structures of different barium halides are shown in Figures A.1. In Figure A.2 the lattice structure of $BaCl_2$, $BaBr_2$, and BaI_2 and their corresponding lattice parameters are depicted. Due to the same charge state of Ba^{2+} and Eu^{2+} a Eu^{2+} dopant should substitute a barium ion.

The x-ray fluorescence spectrum of 10% Eu-doped $BaCl_2$ is shown in Figure A.3. The most significant peaks at 4469 and 4857 eV can be attributed to the $L_{\alpha 1,2}$ and $L_{\beta 3,4}$ lines of barium. The $L_{\alpha 1,2}$ line of Eu can be found at 5835 eV. The EXAFS spectrum of the Eu L_{III}-edge in $BaCl_2$ can be seen in Figure A.4, where the white line at 6980 eV is due to Eu^{3+}. Since in the crystal growth process only a small amount of Eu^{2+} was incorporated in the sample the white line of Eu^{2+} is only a small shoulder at about 6972 eV. The relative intensity of the two white lines is an indication of the Eu^{2+}/Eu^{3+} ratio. A detailed analysis to obtain quantitative information about the ratio has not been done yet.

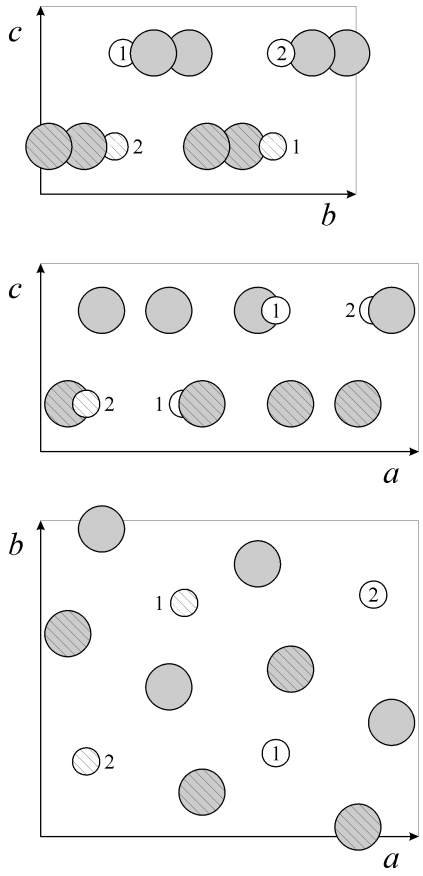

Figure A.1: Lattice structure of orthorhombic BaX_2 projected on the *ab*, *ac*, and *bc* planes, small white and large gray circles denoting Ba^{2+} and X^- (X = Cl, Br, I) ions, respectively. The ions discerned by hatched circles lie in a different *ab*-type mirror plane than the non-hatched ones. Two types of magnetically non-equivalent Ba sites are labeled 1 and 2. The radii are scaled to 30% of their original values.

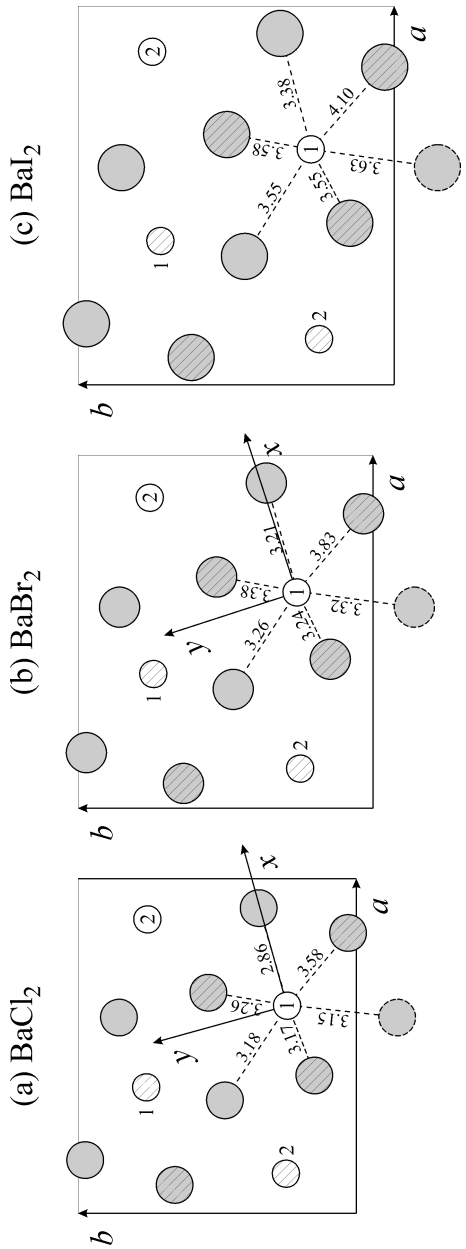

Figure A.2: Lattice structure of orthorhombic (a) $BaCl_2$, (b) $BaBr_2$, and (c) BaI_2 projected on the *ab* plane, small white and large gray circles denoting Ba^{2+} and X^- ions, respectively. The ions discerned by hatched circles lie in a different *ab*-type mirror plane than the non-hatched ones. Two types of Ba sites are labeled 1 and 2. The distances indicated are given in Å. The radii are scaled to 30% of their original values. The principal directions x and y of the crystal field are indicated.

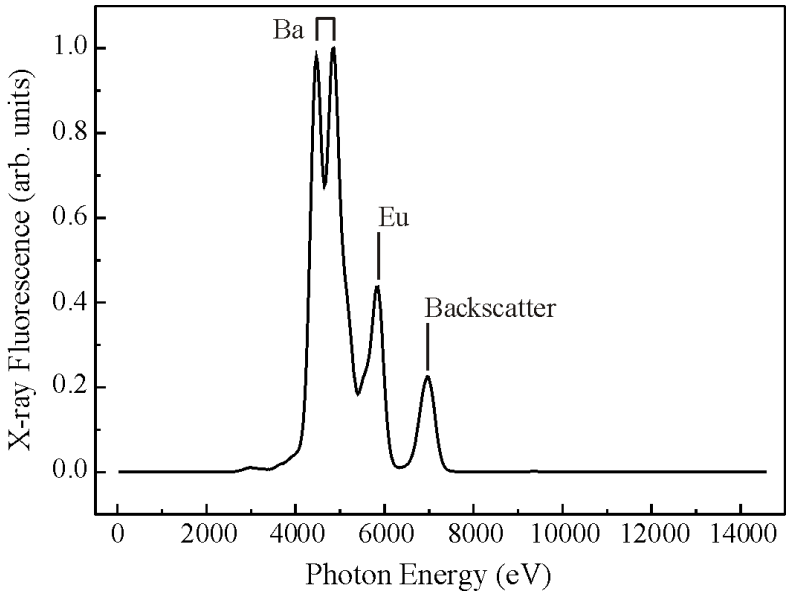

Figure A.3: Normalized X-ray fluorescence spectrum of 10% Eu-doped $BaCl_2$ with an excitation energy of 7080 eV.

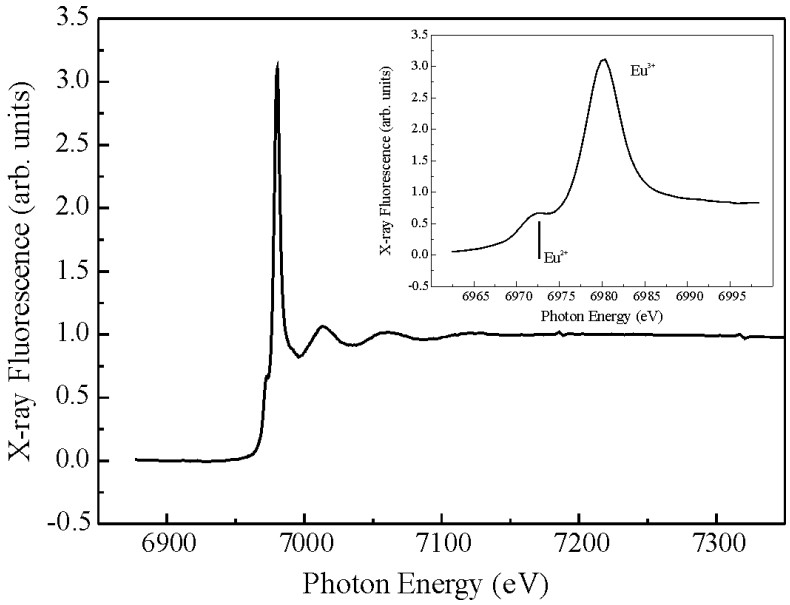

Figure A.4: Normalized EXAFS spectrum of 10% Eu-doped $BaCl_2$. The spectrum was recorded in fluorescence mode. The inset shows the Eu absorption edge in more detail.

B Miscellaneous

B.1 Euler Tensor

The definition of the matrix $\underline{\underline{E}}$ is:

$$\underline{\underline{E}} = \begin{pmatrix} E_{xx} & E_{xy} & E_{xz} \\ E_{xy} & E_{yy} & E_{yz} \\ E_{xz} & E_{yz} & E_{zz} \end{pmatrix}$$

With its elements:

$$\begin{aligned}
E_{xx} &= \cos\alpha \cdot \cos\beta \cdot \cos\gamma - \sin\alpha \cdot \sin\gamma \\
E_{xy} &= \cos\beta \cdot \cos\gamma \cdot \sin\alpha + \sin\gamma \cdot \cos\alpha \\
E_{xz} &= -\cos\gamma \cdot \sin\beta \\
E_{xy} &= -\sin\gamma \cdot \cos\alpha \cdot \cos\beta - \cos\gamma \cdot \sin\alpha \\
E_{yy} &= -\sin\gamma \cdot \cos\beta \cdot \sin\alpha + \cos\gamma \cdot \cos\alpha \\
E_{yz} &= \sin\beta \cdot \sin\gamma \\
E_{zx} &= \sin\beta \cdot \cos\alpha \\
E_{zy} &= \sin\beta \cdot \sin\alpha \\
E_{zz} &= \cos\beta
\end{aligned}$$

These definitions are the same as used in the VISUAL EPR program. To transform a matrix in a new axis system the formula $\underline{\underline{M}}_{new} = \underline{\underline{E}} \cdot \underline{\underline{M}} \cdot \underline{\underline{E}}^T$ is used. $\underline{\underline{E}}^T$ is the transpose of the Euler matrix.

A rotation of the Euler angles of the center orientation is described by $\underline{\underline{E}}_{new} = \underline{\underline{E}}_{rot} \cdot \underline{\underline{E}}_{old}$. The new angles are given by:

$$\beta_{new} = \arccos\left(E_{zz}^{new}\right)$$

$$\begin{aligned} \alpha_{new} &= \arcsin\left(\frac{E_{zy}^{new}}{\sin\beta_{new}}\right) \\ \gamma_{new} &= \arcsin\left(\frac{E_{yz}^{new}}{\sin\beta_{new}}\right) \end{aligned}$$

B.2 Fine Structure Tensor

The definition of the fine structure tensor $\underline{\underline{D}}$ is

$$\underline{\underline{D}} = \begin{pmatrix} D_{xx} & D_{xy} & D_{xz} \\ D_{xy} & D_{yy} & D_{yz} \\ D_{xz} & D_{yz} & D_{zz} \end{pmatrix}$$

In the "Grachev" program the elements are defined by:

$$\begin{aligned} D_{xx} &= 1/3 \cdot (-b_2^0 + b_2^2) \\ D_{yy} &= 1/3 \cdot (-b_2^0 - b_2^2) \\ D_{zz} &= 2/3 \cdot b_2^0 \\ D_{xy} &= 1/3 \cdot c_2^2 \\ D_{xz} &= 1/6 \cdot b_2^1 \\ D_{yz} &= 1/6 \cdot c_2^1 \end{aligned}$$

With the inversion:

$$\begin{aligned} b_2^0 &= 3/2 \cdot D_{zz} \\ b_2^1 &= 3 \cdot D_{xz} \\ c_2^1 &= 6 \cdot D_{yz} \\ b_2^2 &= 3 \cdot D_{xx} - b_2^0 \\ c_2^2 &= 3 \cdot D_{xy} \end{aligned}$$

A further description of the main axis elements is given by:

$$\begin{aligned} D_{xx} &= -1/3 \cdot D + E \\ D_{yy} &= -1/3 \cdot D - E \\ D_{zz} &= 2/3 \cdot D \end{aligned}$$

This yields:

$$\begin{aligned} b_2^0 &= D \\ b_2^2 &= 3 \cdot E \end{aligned}$$

B.3 EPR Data

Host	g	A(10^{-4} cm^{-1})	a(10^{-4} cm^{-1})	Reference
$LiBaF_3$	2.0014 ± 0.0004	-88.3 ± 0.1	5.5 ± 0.1	[26]
$RbCdF_3$	1.99 ± 0.01	-90.4 ± 0.3	14 ± 0.3	[18]
$RbMgF_3$	2.001	88.7		[49]

Table B.1: Hyperfine structure parameter for Mn^{2+} in different host lattices.

Bibliography

[1] W. A. Sibley and N. Koumvakalis. *Phys. Rev. B* **14**(1), 35 (1976).

[2] M. A. Losada, R. Alcala, P. J. Alonso, R. Cases, and V. M. Orera. *Radiation Effects Express* **2**, 39–44 (1988).

[3] Y. Murayama, N. Takeuchi, Y. Aoki, and T. Matsuzawa. Technical report, US Patent 5,424,006, (1995).

[4] T. Matsuzawa, N. Aoki, Y. Takeuchi, and Y. Murayama. *J. Electrochem. Soc.* **143**, 2670 (1996).

[5] T. Aitasalo, J. Hölsä, H. Jungner, M. Lastusaari, and J. Niittykoski. *J. Lumin.* **94-95**, 59–63 (2001).

[6] G. Blasse and B. C. Grabmaier. *Luminescent Materials.* Springer Verlag, Berlin Heidelberg, (1994).

[7] B. Henderson and G. F. Imbusch. *Optical Spectroscopy of Inorganic Solids.* Clarendon Press, Oxford, (1989).

[8] F. Rodriquez and M. Moreno. *J. Chem. Phys.* **84**(2), 692–697 (1986).

[9] P. G. Baranov, V. A. Vetrov, and N. G. Romanov. *Sov. Phys. Solid State* **25**(5), 784–788 (1983).

[10] Boon K. Teo. *EXAFS: Basic Principles and Data Analysis.* Springer-Verlag, (1986).

[11] J. Dumschat. *Hochauflösende Röntgenabsorptionsspektroskopie an vierwertigen Seltene-Erdsystemen.* PhD thesis, University of Paderborn, (2000).

[12] *http://physics.nist.gov/PhysRefData/FFast/html/form.html* (Retrieved 2007).

[13] T. Rewaj, M. Krupski, J. Kuriata, and J. Y. Buzaré. *J. Phys.: Condens. Matter* **4**(49), 9909–9918 (1992).

[14] M. Rousseau, J. Y. Gesland, J. Julliard, J. Nouet, J. Zarembowitch, and A. Zarembowitch. *Phys. Rev. B* **12**(4), 1579–1590 (1975).

[15] P. Studzinski and J. M. Spaeth. *Radiation Effects* **73**, 207–213 (1983).

[16] D'Ans-Lax. *Taschenbuch für Chemiker und Physiker*. Springer-Verlag, (1970).

[17] J. Ferguson. *Australian Journal of Chemistry* **21**, 307–321 (1968).

[18] P. Studzinski. *Paramagnetische Ionen zur Untersuchung struktureller Phasenübergänge - Eine* ENDOR *Untersuchung*. PhD thesis, Universität Paderborn, (1985).

[19] C. Dotzler, G. V. M. Williams, A. Edgar, S. Schweizer, B. Henke, J.-M. Spaeth, A. Bittar, J. Hamlin, and C. Dunford. *J. Appl. Phys.* **100**, 033102 (2006).

[20] *http://cars9.uchicago.edu/∼newville/ModelLib/search.htm* (Retrieved 2007).

[21] *http://cars9.uchicago.edu/∼ravel/software/aboutathena.html* (Retrieved 2007).

[22] M. C. Marco de Lucas, F. Rodriguez, M. Moreno, and A. Tressaud. *J. Phys.: Condens. Matter* **6**, 6353–6366 (1994).

[23] R. L. Lambe and D. Schroeer. *Phys. Rev. Lett.* **36**(1), 45 (1976).

[24] J. Selling. *Barium Halide Nanocrystals in Fluorozirconate based Glass Ceramics for Scintillation Application*. PhD thesis, University of Paderborn, (2007).

[25] V. Möllmann, J. Selling, B. Henke, S. Schweizer, P. Keil, V. Lavin, and G. Wortmann. *Annual HASYLAB Report 2007* **submitted** (2007).

[26] T. Yosida, H. Aoki, H. Takeuchi, M. Arakawa, and K. Horai. *J. Phys. Soc. Jpn.* **46**(5), 1661–1662 (1979).

[27] W. L. W. Ludekens and A. J. E. Welch. *Acta Crystallographica* **5**, 841 (1952).

[28] T. Yosida. *J. Phys. Soc. Jpn.* **49**(1), 127–135 (1980).

[29] N. Shiran and V. Voronova. *J. Lumin.* **87-89**, 561–563 (2000).

[30] A. Abragam and B. Bleany. *Electron Paramagnetic Resonance of Transition Ions*. Dover Publications, New York, (1986).

[31] F. K. Koschnick, Th. Hangleiter, K. S. Song, and J.-M. Spaeth. *J. Phys.: Condens. Matter* **7**, 6925–6937 (1995).

[32] S. Schweizer, U. Rogulis, K. S. Song, and J.-M. Spaeth. *J. Phys.: Condens. Matter* **12**, 6237–6243 (2000).

[33] U. Rogulis, S. Schweizer, and J.-M. Spaeth. *J. Phys.: Condens. Matter* **14**(28), 6949–6956 (2002).

[34] B. Henke, M. Secu, U. Rogulis, S. Schweizer, and J.-M. Spaeth. *Phys. Status Solidi C* **2**(1), 380–383 (2005).

[35] W. Jia, H. Yuan, L. Lu, H. Liu, and W. M. Yen. *J. Lumin.* **76&77**, 424–428 (1998).

[36] W. Jia, H. Yuan, L. Lu, H. Liu, and W. M. Yen. *J. Cryst. Growth* **200**, 179–184 (1999).

[37] D. Jia, S. Meltzer, W. M. Yen, W. Jia, and X. Wang. *Appl. Phys. Lett.* **80**(9), 1535–1537 (2002).

[38] T. Aitasalo, P. Deren, J. Hölsä, H. Jungner, J.-C. Krupa, M. Lastusaari, J. Legendziewicz, J. Niittykoski, and W. Strek. *Journal of Solid State Chemistry* **171**, 114–122 (2003).

[39] Y. Lin, Z. Tang, Z. Zhang, and C. Nan. *Journal of the European Ceramic Society* **23**, 175–178 (2003).

[40] A. Nag and T. R. N. Kutty. *Materials Research Bulletin* **39**, 331–342 (2004).

[41] P. Dorenbos. *Journal of the Electrochemical Society* **152**(7), H107–H110 (2005).

[42] P. Dorenbos. *Phys. Status Solidi B* **242**, R7–R9 (2005).

[43] W. M. Yen. *Preparation of Single Crystal Fibers in: Insulating Materials for Optoelectronics*. World Scientific, Singapore, (1995).

[44] A. A. Kaminskii. *Laser Crystal*, volume 14 of *Optical Series*. Springer-Verlag, Berlin, 2nd edition, (1981).

[45] H. M. Crosswhite and G. H. Dieke. *J. Chem. Phys.* **35**(5), 1535–1548 (1961).

[46] T. Nakamura, T. Matsuzawa, C. C. Rowlands, V. Beltrán-López, G. M. Smith, and P. C. Riedi. *J. Chem. Soc., Faraday Trans.* **94**, 3009–3012 (1998).

[47] J.-M. Spaeth and H. Overhof. *Point Defects in Semiconductors and Insulators.* Springer, Berlin, (2003).

[48] E. B. Brackett, T. E. Brackett, and R. L. Sass. *J. Phys. Chem.* **67**(10), 2132 (1963).

[49] J. M. Dance and N. Kerkouri. *C. R. Acad. Sc. Paris* **289**(C), 425–428 (1979).

List of Publications

[1] B. Henke, M. Secu, U. Rogulis, S. Schweizer, and J.-M. Spaeth.
Optical and magneto-optical studies of Mn-activated $LiBaF_3$
phys. stat. sol. c **2**(1), 380–383 (2005).

[2] S. Schweizer, B. Henke, U. Rogulis, and W. M. Yen.
Magneto-optical resonance investigations on Eu and Nd/Dy-codoped $CaAl_2O_4$ and $SrAl_2O_4$ single crystals
in Science and Technology of Dielectrics in Emerging Fields and Persistent Phosphors (PV 2005-13), edited by K. Wörhoff, D. Misra, P. Mascher, K. Sundaram, W. M. Yen, and J. Capobianco (The Electrochemical Society, Quebec City, Canada, 2005), Part II, p. 191.

[3] C. Dotzler, G. V. M. Williams, A. Edgar, S. Schweizer, B. Henke, J.-M. Spaeth, A. Bittar, J. Hamlin, and C. Dunford.
The effect of x-ray, γ-ray, and UV radiations on the optical properties of $RbCdF_3$:Mn^{2+}
J. Appl. Phys. **100**, 033102 (2006).

[4] B. Henke, U. Rogulis, and S. Schweizer.
Luminescent oxygen-vacancy complex in Mn-doped $LiBaF_3$ investigated by optically detected magnetic resonance
Proceedings of the Eighth International Conference on Inorganic Scintillators and their Use in Scientific and Industrial Applications, Alushta, Crimea, Ukraine, September 19-23, 2005, ed. by A. Gektin and B. Grinyov (National Academy of Sciences of Ukraine, Ukraine - Kharkov, 2006), 70–73 (2006).

[5] B. Henke, U. Rogulis, and S. Schweizer.
Optically detected magnetic resonance investigation of a luminescent oxygen-vacancy complex in Mn-doped $LiBaF_3$
J. Phys.: Condens. Matter **18**(5), 1577–1583 (2006).

[6] J. A. Johnson, S. Schweizer, B. Henke, G. Chen, J. Woodford, P. J. Newman, and D. R. MacFarlane.
Eu-activated fluorochlorozirconate glass-ceramic scintillators
J. Appl. Phys. **100**, 034701 (2006).

[7] S. Schweizer, B. Henke, S. Köneke, J. A. Johnson, G. Chen, and J. Woodford.
Energy-dependent scintillation intensity of fluorozirconate-based glass-ceramic x-ray detectors
Proc. of SPIE **6142**, 61422Y–1 (2006).

[8] G. V. M. Williams, S. Schweizer, B. Henke, C. Dunford, and A. Edgar.
X-ray and UV induced photo-luminescence from $RbCdF_3$:Mn^{2+}
Curr. Appl. Phys. **6**, 351–354 (2006).

[9] S. Schweizer, B. Henke, U. Rogulis, and W. M. Yen.
Recombination processes in undoped and rare-earth doped MAl_2O_4 (M=Ca, Sr) persistent phosphors investigated by optically detected magnetic resonance
Appl. Phys. Lett. **90**, 051902 (2007).

[10] B. Henke, S. Schweizer, and U. Rogulis.
Optical and electron paramagnetic resonance studies on radiation defects in Mn-activated $RbCdF_3$
phys. stat. sol. c **4**, No. 3, 677-682 (2007).

[11] S. Schweizer, B. Henke, U. Rogulis, and W. M. Yen.
Recombination processes in rare-earth doped MAl_2O_4 (M = Ca, Sr) persistent phosphors investigated by optically-detected magnetic resonance
phys. stat. sol. a **204**, 677-682 (2007).

[12] B. Henke, S. Schweizer, J. A. Johnson, and D. T. Keane.
Zr and Ba edge phenomena in the scintillation intensity of fluorozirconate-based glass-ceramic X-ray detectors
J. Sychrotron Rad. **14**, 252-256 (2007).

[13] B. Henke, U. Rogulis, and S. Schweizer.
Structure sensitive investigations on luminescence centres in Mn-activated $LiBaF_3$ dosimeters
Radiat. Meas., (submitted September 2007).

In Preparation

[1] B. Henke, U. Rogulis, Mike and S. Schweizer.
Structure sensitive investigations of a x-ray induced defect in Mn-activated $LiBaF_3$
J. Phys.: Condens. Matter.

[2] B. Henke, J. A. Johnson, and S. Schweizer.
EXAFS investigations on the Mn-doped fluoroperovskite $RbCdF_3$
J. Phys.: Condens. Matter.

[3] B. Ahrens, B. Henke, J. A. Johnson, P. T. Miclea and S. Schweizer.
Enhanced up-converted fluorescence in fluorozirconate based glass ceramics for high efficiency solar cells
Proc. of SPIE.

Danksagung

Abschließend möchte ich mich bei den Menschen bedanken, die mir während meiner Promotion zur Seite gestanden haben:

- PD Dr. Stefan Schweizer für die Möglichkeit in seiner Arbeitsgruppe zu promovieren und sein stets förderndes Engagement.
- Prof. Dr. G. Wortmann für viele wertvolle Diskussionen.
- Meinen beiden Kollegen Julia Selling und Bernd Ahrens für die Hilfe in allen möglichen Lebenslagen.
- Prof. Dr. Uldis Rogulis für die nicht immer unproblematische Einführung in die ODMR Spektroskopie.
- Dr. Jacqueline A. Johnson, die meine offensive Auslegung der englischen Grammatik in die richtigen Bahnen gelenkt hat.
- Dr. Mihail Secu für viele wissenschaftliche Anregungen.
- Den Mitarbeitern des Kristallzuchtlabors D. Niggemeier und R. Winterberg.
- J. Pauli für die problemlose Versorgung mit flüssigem Helium.

- Den Mitarbeitern der APS Denis T. Keane und Qing Ma für die freundliche und kompetente Hilfe bei den Experimenten an der APS[1] sowie Dariusz Zajac als Mitarbeiter des HASYLABs.

- Allen namentlich nicht erwähnten Institutsmitgliedern für die gute Zusammenarbeit und das hervorragende Arbeitsklima.

Auch danke ich meiner Freundin Sarah Schuller und meinen Eltern, die mich zu jeder Zeit nach besten Kräften unterstützt haben.

[1]This work was performed at the DuPont-Northwestern-Dow Collaborative Access Team (DND-CAT) Synchrotron Research Center located at Sector 5 of the Advanced Photon Source. DND-CAT is supported by the E.I. DuPont de Nemours & Co., The Dow Chemical Company, the U.S. National Science Foundation through Grant DMR-9304725 and the State of Illinois through the Department of Commerce and the Board of Higher Education Grant IBHE HECA NWU 96.

Use of the Advanced Photon Source was supported by the U. S. Department of Energy, Office of Science, Office of Basic Energy Sciences, under Contract No. W-31-109-Eng-38.